STUDIES ON THE THERMOELECTRIC PERFORMANCE OF LEAD AND TIN CHALCOGENIDES

A Dissertation Presented to

the Faculty of the Department of Physics

University of Houston

In Partial Fulfillment of
the Requirements for the Degree

Doctor of Philosophy

By

Eyob Kebede Chere

August 2016

STUDIES ON THE THERMOELECTRIC PERFORMANCE OF LEAD AND TIN CHALCOGENIDES

_____

Eyob Kebede Chere

APPROVED:

_____

Dr. Zhifeng Ren, Advisor

_____

Dr. Gemunu Gunaratne

_____

Dr. Jiming Bao

_____

Dr. Shuo Chen

_____

Dr. Dong Cai

_____

Dean, College of Natural Sciences and Mathematics

ACKNOWLEDGEMENTS

First of all, I would like to express my special appreciation and thanks to my advisor, Professor Zhifeng Ren for his valuable guidance, scholarly inputs, consistent mentoring, and encouragement. Prof. Ren was always available for discussion and his insightful advising helped me at various stages of my research to grow as a research scientist.

I would like to show my sincere gratitude to the committee members, Professor Gemunu Gunaratne, Professor Jiming Bao, Professor Shuo Chen, and Professor Dong Cai for serving as my committee members and for their perceptive comments and suggestions.

I am indebted to thank my lab mates whom I have worked with for their personal and professional help each extended to me in their own unique way. I especially owe my deepest gratitude to Dr. Qian Zhang who taught me not only the lab culture but also make me to understand the hard facts to grow as a professional through her fruitful guidance and thoughtful suggestions. Working with her was truly inspirational.

I extend my special thanks to my parents especially my beloved sisters and my God father Asnake Simegn who laid the very foundations of my bright future, mold and shape my dreams that has lead me where I am now. I would like to thank my girlfriend Melkam A. Garedew for her unconditional love and support in my endeavors.

I would like to acknowledge my friends Dr. Merzu Belete, Maru Belay, Shore Salle, Ayichew Eshete for always being there and bearing with me during my wonderful days of Ph.D.

Finally, above all I would like to thank the almighty God for his abundant blessing and grace to see the finish.

STUDIES ON THE THERMOELECTRIC PERFORMANCE OF LEAD AND TIN CHALCOGENIDES

An Abstract of a Dissertation

Presented to

the Faculty of the Department of Physics

University of Houston

In Partial Fulfillment

of the Requirements for the Degree

Doctor of Philosophy

University of Houston

By

Eyob Kebede Chere

August 2016

ABSTRACT

With the growing interest of the world's energy demand, sustainable and green energy is becoming a global challenge. Thermoelectric power generation, that directly converts waste heat into electricity, is considered as one of the potent alternatives to solve this challenge. IV-VI alloys, especially lead chalcogenides are one of the most studied thermoelectric materials due to their decent thermoelectric figure of merit, *ZT,* from 573 K-873 K. On the contrary, tin chalcogenides, especially tin-selenides are rarely studied as thermoelectric materials due to their larger band gaps. This dissertation, addresses the systematic study of the thermoelectric performance of lead chalcogenides (PbTe, PbSe, PbS and their alloys) and tin chalcogenides (n and p-type SnSe) prepared by melting and hot pressing. We found that, Cr doping increases the Seebeck coefficient and power factor of n-type PbSe and $PbTe_{1-y}Se_y$ alloys near room-temperature. The higher Seebeck coefficient and power factor enhancements are attributed to the higher Hall mobilities of ~1000-1120 $cm^2\ V^{-1}s^{-1}$ at lower carrier concentrations. The high power factor combined with lower thermal conductivity due to large Grüneisen parameter in PbSe, and alloy scattering in $PbTe_{1-y}Se_y$, lead to a room-temperature *ZT* enhancement of ~0.4 in $Cr_{0.005}Pb_{0.995}Se$, ~0.5 in selenium-rich $Cr_{0.01}Pb_{0.99}Te_{0.25}Se_{0.75}$, and ~0.6 in tellurium-rich $Cr_{0.015}Pb_{0.985}Te_{0.75}Se_{0.25}$ respectively. Consequently, the average *ZT* was improved from 300 K-873 K and lead to thermal to electrical conversion efficiency of up to ~12 % in $Cr_{0.005}Pb_{0.995}Se$, ~10 % in tellurium-rich $Cr_{0.015}Pb_{0.985}Te_{0.75}Se_{0.25}$, and ~12 % in selenium-rich $Cr_{0.01}Pb_{0.99}Te_{0.25}Se_{0.75}$, withcold-side temperature of 300 K and hot-side temperature of 773 K. In another study of $PbTe_{1-y}S_y$ alloy, by combination of indium doping and

thermal conductivity reduction via alloy scattering and spinodal decomposition, the room-temperature and average *ZT* was significantly improved leading to efficiency of ~12 % in $In_{0.02}Pb_{0.98}Te_{0.8}S_{0.2}$ with cold-side temperature of 323 K and hot-side temperature of 773 K. In addition to lead chalcogenides, we also investigated the thermoelectric performance of polycrystalline SnSe. We achieved a peak *ZT* of ~1 and ~0.8 at ~773 K in n-type $SnSe_{0.87}S_{0.1}I_{0.03}$ and p-type $Na_{0.015}Sn_{0.985}Se$ respectively, by combination of optimized doping and lower thermal conductivity due to mainly anharmonic and anisotropic bonding.

DEDICATION

To the loving memory of my mom Birke Yilkeku, my dad Kebede Chere, and my brother–in-law Zelekew Shibeshi.

TABLE OF CONTENTS

ABBREVIATIONS

Abbreviation	Meaning
DC hot press	Direct current induced hot press
AC hot press	Alternating current induced hot
XRD	X-ray diffraction
EDS	Energy dispersive spectroscopy
TEM	Transmission electron microscopy
SEM	Scanning electron microscopy
IR	Infrared
TC	Thermocouple
TE	Thermoelectric
RT	Room temperature
atm. %	Atomic percentage

LIST OF SYMBOLS

Symbol	Meaning
PF	Power factor
v_s	Speed of sound
ZT	Dimensionless figure-of-merit
T	Temperature
S	Seebeck coefficient
π_{ab}	Peltier coefficient
Ef	Fermi energy
σ	Electrical conductivity
κ	Thermal conductivity
τ	Scattering time
e	Electronic charge
μ	Carrier mobility
m^*	Effective mass
k_B	Boltzmann constant
n	Hall concentration
ω	Frequency
l	Mean free path
κ_l	Lattice thermal conductivity
κ_e	Electronic thermal conductivity
η	Efficiency
COP	Coefficient of performance
R_H	Hall coefficient
Q	Heat flux
ρ	Resistivity
$t_{1/2}$	Half time
α	Thermal diffusivity
C_p	Specific heat capacity
J	Current density
β	Thomson coefficient
ΔT	Temperature difference
q	Phonon momentum
G	Reciprocal lattice vector
f	Fermi-Dirac distribution function
k	Crystal momentum
r	Position vector
$\hbar$	Reduced Plank's constant

t	Time
Ω_0	Volume per atom
v_s	Phonon Velocity

LIST OF FIGURES

LIST OF TABLES

CHAPTER 1: THEORY OF THERMOELECTRIC PHENOMENA

1.1. Historical Development

Thermoelectric phenomena, which underlie the conversion of heat directly into electricity or vice versa, have been known recognized since 1821, when the German physicist Seebeck first discovered thermoelectric phenomena from his experimental observation of a voltage developed in a loop containing two dissimilar metals where two junctions are maintained at two different temperatures [1]. Shortly after this discovery, Peltier discovered the complimentary effect where a temperature difference could be produced at the junctions of two dissimilar metals when electric current passed through it [1]. In 1838, Lenz explained this as the junctions act as heat sink or heat source depending on the direction of the current [2]. Despite the discovery of the Seebeck and Peltier effects, thermoelectric applications showed a slow progress until the development of thermodynamics in 1850. In 1851, William Thomson (Lord Kelvin) established a theoretical relationship between the Seebeck and Peltier coefficients by applying thermodynamics. He predicted the existence of the third thermoelectric effect called the Thomson effect [3]. This effect relates the heating or cooling in a single homogeneous conductor when a current passes along it in the presence of a temperature gradient. Thomson's work showed that, the thermocouple is a type of heat engine and that might in principle be used either as a device for generating electricity from heat or alternatively as a heat pump or refrigerator [4]. The problem of energy conversion using thermocouples was analyzed by Altenkirch for the first time in 1911 [4,5].

He showed that, the performance of a thermocouple could be improved by increasing the magnitude of the differential Seebeck coefficient, by increasing the electrical conductivities of the two branches and by reducing their thermal conductivities. Unfortunately, at that time, there were no thermocouples available in which the combination of properties was good enough for reasonably efficient energy conversion. The field of thermoelectricity advanced rapidly in 1950 after the introduction of semiconductors as thermoelectric materials, which allowed for practical thermoelectric devices to be made [4]. Work on semiconductor thermocouples also led to the construction of thermoelectric generators with a high enough efficiency for special applications. Nevertheless, the performance of thermoelectric energy converters has always remained inferior to that of the best conventional machines. In fact, there was little improvement in thermoelectric materials from the time of the introduction of semiconductor thermoelements until the end of the twentieth century. However, in recent years, several new ideas for the improvement of materials have been put forwarded and significant advances are being made, at least on a laboratory scale.

Over the last few decades thermoelectricity acquired new impetus owing to the growing awareness that fossil fuels are limited, energy demand is constantly growing and the environmental impact associated with fossil fuels is increasingly alarming [6-10]. Consequently, the field of thermoelectricity gained significant attention from the scientific community. Recently, several new ideas for the improvement of thermoelectric materials have been suggested and extensive researches are now in varying stages of development.

1.2. Principle of Thermoelectricity and Thermoelectric Coefficients

1.2.1. Seebeck Effect

The Seebeck effect, underlying the phenomena of conversion of heat energy into electrical power can be demonstrated by making a connection of two wires of different metals, say A and B. The other ends of these two metals are connected to the terminals of a sensitive voltmeter as shown in Figure 1.2.1.1. Originally, in the absence of temperature gradient, the conductors have uniform distribution of charge carriers and the voltmeter reads zero potential difference. When the junctions between the two conductors subjected to a temperature gradient, the free carriers at the hot end will gain kinetic energy and tend to flow to the cold end. This creates a build up of charge at the two ends. Consequently, a potential difference will be developed and the voltmeter reads a small voltage.

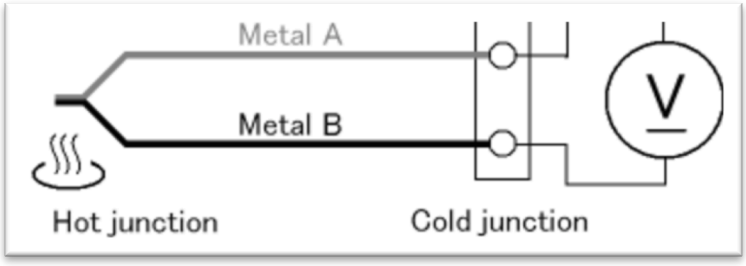

Figure 1.2.1.1 Simple experimental setup for Seebeck effect demonstration [1].

This open circuit potential V is linearly related to the temperature difference between the ends and mathematically given by:

$$V = S(T_1 - T_2) \qquad (1.2.1.1)$$

Where the temperatures, T_1 and T_2 are the hot-side andcold-side temperatures respectively and the proportionality constant S is called Seebeck coefficient.

1.2.2. Peltier Effect

The Peltier effect is the complementary of the Seebck effect. In this case, electric current produces temperature gradient when it passed across the junction. This phenomena is very useful for thermoelectric cooling applications. The amount of heat (Q) absorbed at the junction due to the electric current (I) is mathematically expressed by Equation 1.2.2.1.

$$Q = \pi_{ab} I \qquad (1.2.2.1)$$

Where π_{ab} is the Peltier coefficient of the junction. Figure 1.2.2.1 shows a simple schematic representation of a thermocouple showing Peltier effect.

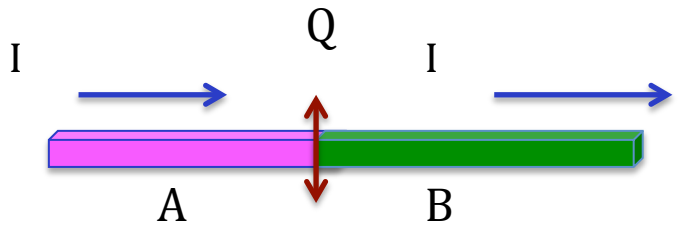

Figure 1.2.2.1 Peltier effect in two dissimilar materials A and B where I is electric current and Q is the amount of heat absorbed at the junction.

When a hot carrier (electron or hole) passes through the junction, it gives away energy and temperature difference is developed at the junction. The Peltier effect arises due to the difference in the potential energies of the charge carriers in the materials.

1.2.3. Thomson Effect

The third important thermoelectric effect is the Thomson effect that relates the rate of generation of heat due to electric current along a portion of a single material at a temperature difference ΔT.

Figure 1.2.3.1 shows a schematic representation of Thomson effect on a single material.

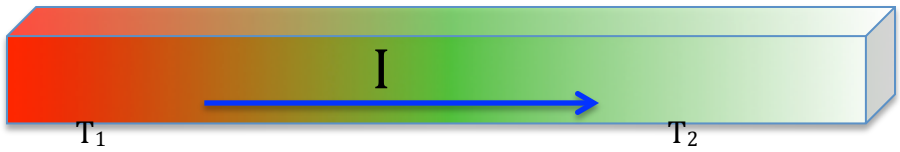

Figure 1.2.3.1 Thomson effect on a single material due to electric current (*I*) and temperature difference ($\Delta T = T_1 - T_2$).

The generated heat is mathematically given by Equation 1.2.3.1 below.

$$Q = \beta I \Delta T \qquad (1.2.3.1)$$

Where β is Thomson coefficient, *I* is electric current, and ΔT is temperature difference.

1.2.4. The Kelvin Relation

The Kelvin relation is a mathematical expression that relates the three thermoelectric coefficients, *i.e.,* the Seebeck coefficient (*S*), the Peltier coefficient (π_{ab}), and the Thomson coefficient (β) together. These relationships are expressed in Equation 1.2.4.1 and Equation 1.2.4.2 below.

$$S_{ab} = \frac{\pi_{ab}}{T} \qquad (1.2.4.1)$$

$$\frac{dS_{ab}}{dT} = \frac{\beta_a - \beta_b}{T} \qquad (1.2.4.2)$$

The first equation relates the Seebeck coefficient with Peltier coefficient and the second equation relates the Seebeck coefficient to Thomson coefficient. The relationship between Peltier and Thomson coefficients can also be derived from the two equations.

1.3. Thermoelectric Transport Properties

The ability of a thermoelectric (TE) material to convert heat into electricity is characterized by its dimensionless figure of merit (*ZT*), itself is a function of the thermal and electronic transport properties. Mathematically, it is expressed by $ZT = \frac{S^2\sigma T}{\kappa_e+\kappa_l}$, where σ is the electrical conductivity, *S* is the Seebeck coefficient, κ_e is electronic thermal conductivity, κ_l is lattice thermal conductivity, and *T* is the absolute temperature [12]. To achieve a higher *ZT* value, materials should have high electrical conductivity, high Seebeck coefficient, and low thermal conductivity. Therefore, it is important to investigate their transport properties in order to improve the performance of thermoelectric materials. In the following sections, we will address thermoelectric transport properties in detail.

1.3.1. Electrical Conductivity

At finite fields, the electrical conductivity depends on the product of carrier density and carrier mobility. To the extent that electrons and holes can be considered as particles, the electrical conductivity can be determined by solving the semi-classical Boltzmann transport equation [13]. The Boltzmann transport equation is a statement, that in steady-state, there is no net change in the distribution function $f\ (\vec{r}, \vec{k}, t)$ that determines the probability of finding an electron at position $\vec{r}$, crystal momentum $\vec{k}$, and time *t* [13].

Therefore, the generalized Boltzmann transport equation is based on the framework that we get no change of the distribution function $f\ (\vec{r}, \vec{k}, t)$ due to the three processes. These are diffusion, the effect of forces or fields, and collisions.

$$\frac{\partial f(\vec{r},\vec{k},t)}{\partial t} + \vec{v}\,(\vec{k})\frac{\partial f(\vec{r},\vec{k},t)}{\partial t} + \frac{\partial(\vec{k})}{\partial t}\frac{\partial f(\vec{r},\vec{k},t)}{\partial \vec{k}} = \left(\frac{\partial f(\vec{r},\vec{k},t)}{\partial t}\right)_{\text{collision}} \qquad (1.3.1.1)$$

Where the first two left hand side (LHS) terms of Equation 1.3.1.1 are diffusion terms that describe the change of the distribution function due to diffusion, the third LHS term of Equation 1.3.1.1 is the fields and forces term that describes the change of the distribution function due to the fields and forces, and the right hand side (RHS) term of Equation 1.3.1.1 is the collision term. One way of solving Boltzmann transport equation is by relaxation time approximation so that the system returns to equilibrium uniformly [13]. The electrical conductivity tensor $\vec{\sigma}$ derived from the Boltzmann transport equation in constant relaxation time approximation is given by Equation 1.3.1.2 below.

$$\vec{\sigma} = \frac{e^2}{4\pi^3}\int \tau\vec{v}\,\vec{v}\,(\frac{-\partial f_0}{\partial E})d^3k \qquad (1.3.1.2)$$

Where τ is relaxation time, $\vec{v}$ is the velocity tensor, e is electron charge, and f_0 is the Fermi Dirac distribution function. The temperature dependence of the electrical conductivity comes from the energy dependent Fermi distribution function f_0 by $\frac{\partial f_0}{\partial E}$. For isotropic intrinsic semiconductors with parabolic bands Equation 1.3.1.2 can be simplified to Equation 1.3.1.3.

$$\sigma_{xx} = \frac{2e^2}{m^*}\left(\frac{m*K_BT}{2\pi\hbar^2}\right)^{3/2} exp^{-|E_F|/K_BT} \qquad (1.3.1.3)$$

Where m^* is effective mass and E_F is Fermi energy. Equation 1.3.1.3 shows that the electrical conductivity of semiconductors increases with temperature and decreases with effective mass due to a decrease in drift velocity of the carriers.

1.3.2. Seebeck Coefficient

We have defined Seebeck effect in section 1.2.1 as the potential difference developed across a material in response to temperature gradient. The ratio of the potential difference (open circuit voltage (V)) to the temperature difference is called Seebeck coefficient. The Seebeck coefficient measures the entropy transported with charge as it moves divided by the carrier charge [1]. The Seebeck coefficient is affected by charge carrier interactions. Therefore, it is an important transport property of thermoelectric materials since it also gives information about carrier interactions. Like the electrical conductivity, the Seebeck coefficient tensor S_{ij} can also be derived from Boltzmann transport equation with constant relaxation time approximation.

$$S_{ij} = \frac{1}{eT}\left(\vec{k}_1 \Big/ \vec{k}_0\right) \qquad (1.3.2.1)$$

The tensors $\vec{k}_0$ and $\vec{k}_1$ are given by;

$$\vec{k}_0 = \frac{1}{4\pi^3} \int \tau \vec{v}\, \vec{v} \left(\frac{-\partial f_0}{\partial E}\right) d^3k \qquad (1.3.2.2)$$

$$\vec{k}_1 = \frac{1}{4\pi^3} \int \tau \vec{v}\, \vec{v}\, (E - E_F)^2 \left(\frac{-\partial f_0}{\partial E}\right) d^3k \qquad (1.3.2.3)$$

Where T is temperature, e is electron charge, τ is the relaxation time, E is energy of the electron, and E_F is Fermi energy. For isotropic materials, the Seebeck coefficient is a scalar given by:

$$S = \frac{1}{eT}\frac{k_1}{k_2} \qquad (1.3.2.4)$$

In order to improve the performance of thermoelectric materials, we need to enhance the Seebeck coefficient.

Due to the strong enhancement of Seebeck coefficient with density of electronic states near the Fermi level, significant efforts have been made on the framework of density of states enhancement near the Fermi level. One approach is the low-dimensional concept, which underlies on reducing dimension from bulk 3D materials to 0D quantum dots, where the density of states near Fermi level is like a delta function [14]. This approach helps tuning the Seebeck coefficient and electrical conductivity somehow independently [15,16]. The second approach is modifying the density of states in bulk materials by electronic band structure modification called band engineering. Band engineering approach is one of the potent ways of enhancing the Seebeck coefficient by distortion of density of states near the Fermi level [17]. Distortion of the density of states might be due to resonant states [17] in which the impurity band resonates with the continuum of the host band or due to the convergence of the extrema of two bands at a particular energy [18].

In both cases the density of states gets an extra enhancement and lead to a boost in Seebeck coefficient. Resonance can also improve the thermopower by resonant scattering. This is due to strong electron energy filtering effect at cryogenic temperatures where electron phonon interactions are weaker. Mathematically, the dependent of *S* with density of states and energy dependent mobility is expressed by Equation 1.3.2.5.

$$S = \frac{\pi^2 K_B^2}{3e} T \left(\frac{g(E)}{n(E)} + \frac{1}{\mu(E)} \frac{d\mu(E)}{dE} \right) \qquad (1.3.2.5)$$

Where, K_B is Boltzmann constant, e is electron charge, T is absolute temperature, $n(E)$ is carrier concentration, $g(E)$ is density of states, $\mu(E)$ is mobility, E is energy of electron, and $\pi \approx 3.14$.

The first term in Equation 1.3.2.5 that contains the density of states $g(E)$, enhances the Seebeck coefficient due to the change in the density of states near the Fermi level. The second term in Equation 1.3.2.5 enhances the Seebeck coefficient by energy selective scattering.

1.3.3. Power Factor

In thermoelectrics, it is convenient to introduce a quantity that sums up the electrical conductivity and Seebeck coefficient together. This quantity is called power factor. Mathematically, it is defined by:

$$PF = S^2\sigma \qquad (1.3.3.1)$$

The power factor of a TE material heavily depends upon the position of the Fermi level. It gets smaller when the Fermi level further deepens in the forbidden gap and also moves deep into the conduction and valance bands [4]. The power factor is maximized at an optimum value of Fermi energy where the Seebeck coefficient and electrical conductivity maintained optimum values.

1.3.4. Thermal Conductivity

The transport of heat in solids is characterized by thermal conductivity. Thermal transport in non-degenerate semiconductors is mainly due to phonons, whereas the electrons or holes also contribute a significant amount in heavily doped semiconductors [2,4,13]. In intrinsic semiconductors, the contribution by minority carriers is also non negligible at high temperature. In thermoelectric materials, since thermal conduction transports charge and electrical conduction transports heat energy, the electrical conductivity and thermal

conductivity are coupled. The thermal conductivity is generally a contribution of the lattice part (due to phonons) and electronic part (due to electrons or holes). The total thermal conductivity κ is thus the superposition of the two.

$$\kappa = \kappa_l + \kappa_e \qquad (1.3.4.1)$$

Where κ_l is the lattice part of thermal conductivity, κ_e is electronic part of thermal conductivity. Now let us see the two parts separately.

Lattice Thermal Conductivity: In solids, each atom is bonded to its neighbors and the displacement of one atom would give rise to a disturbance to the other atoms. The atoms in crystals are in continuous motion (vibration) and these vibrations are quantized. The quanta of crystal vibrations are called phonons. Phonons are responsible for the transport of heat in solids since they flow down to the temperature gradient and constitute a thermal current. From simple considerations based on the classical kinetic theory of gases, the lattice thermal conductivity is given by Equation 1.3.4.2 [1].

$$\kappa_l = \frac{1}{3} C v_s l \qquad (1.3.4.2)$$

Where C is phonon heat capacity per unit volume, v_s is the phonon velocity also called speed of sound, and l is phonon mean free path. The phonon mean free path is determined by the extent to which a phonon scatters by other phonons, lattice imperfections, free charge carriers and grain boundaries. The scattering of phonons by other phonons is due to anharmonic lattice interactions, which associate coupling of different phonons [1]. Phonons could interact with each other in two ways. These are called Normal process and Umklapp or U-process. In Normal process the momentum of the phonon is conserved whereas in Umklapp or U-process the phonon momentum is not conserved. Umklapp

interaction is responsible for the scattering of phonons with each other. The following three-phonon process summarizes the two processes of phonon scattering.

$$\vec{q}_1 + \vec{q}_2 = \vec{q}_3 + \vec{G} \qquad (1.3.4.3)$$

$\vec{G} = 0$ is the Normal process; whereas $\vec{G} \neq 0$ is the Umklapp process, where $\vec{G}$ is reciprocal lattice vector and the $\vec{q}_i$s are phonon momenta. The relaxation time approach in Boltzmann transport theory and using an isotropic Debye-like phonon spectrum consisting of one average acoustic branch is a common approach to study the scattering of phonons by lattice disorder, charge carriers and boundary scattering [1]. In this approach, the relaxation time for phonon scattering by atomic mass difference is given by:

$$\tau^{-1} = \Gamma \frac{v_s \Omega_0}{4\pi} \left(\frac{K_B T}{\hbar v_s}\right)^4 Z^4 \qquad (1.3.4.4)$$

Where, $Z = \frac{\hbar\omega}{K_B T}$, $\Gamma = \sum_i f_i \left(1 - \frac{M_i}{M}\right)$, $M = \sum_i f_i M_i$, f_i is fraction of atomic mass M_i, ω is phonon frequency, $\hbar$ is reduced Plank's constant, v_s is sound velocity, Ω_0 is volume per atom, and K_B is Boltzmann constant. From Equation 1.3.4.4, we can see that large atomic mass disorder shortens the relaxation time resulting in a higher phonon scattering that reduces the thermal conductivity. The relaxation time of phonons due to grain boundaries is expressed by $\tau = l/v_s$ where l is similar to grain dimension known as the Casimir length. In a similar way smaller grain sizes in a material will reduce the thermal conductivity by scattering phonons with mean free paths in the order of their sizes.

Electronic Thermal Conductivity: charge carriers (electrons and holes) in solids conduct heat as they transfer energy from hot to cold. The electronic contribution of the thermal conductivity is defined as the thermal current, which is driven by the heat energy E-E_F. The thermal current $\vec{U}$ given in Equation 1.3.4.5 can be derived from Boltzmann transport equation in the relaxation time approximation.

$$\vec{U} = \frac{1}{4\pi^3} \int \vec{v}\ (E - E_F) f_1 d^3k \qquad (1.3.4.5)$$

Where f_1 is determined from Boltzmann equation and E_F is the Fermi energy.

In thermoelectric materials, both electric field and temperature gradient are present and the thermal conductivity tensor can be obtained from Boltzmann equation at constant relaxation time τ.

$$\vec{\kappa}_e = \frac{e^2}{4\pi^3 T} \int \tau \vec{v}\, \vec{v}\, (E - E_F)^2 \left(\frac{-\partial f_0}{\partial E}\right) d^3k \qquad (1.3.4.6)$$

For metals and heavily doped semiconductors, the above equation simplified to Equation 1.3.4.7 called Wiedemann-Franz law.

$$\vec{\kappa}_e = \frac{\pi^2}{3} \frac{K_B^2}{e^2} \vec{\sigma} T \qquad (1.3.4.7)$$

1.3.5. Thermoelectric Figure of merit (*ZT*)

The dimensionless figure of merit (*ZT*) is the measure of performance of a thermoelectric material. It incorporates all the relevant thermoelectric parameters *i.e.,* the electrical and thermal conductivities and the Seebeck coefficient. Mathematically, it is expressed by Equation 1.3.5.1

$$ZT = \frac{S^2 \sigma T}{\kappa} \qquad (1.3.5.1)$$

Where S is Seebeck coefficient, σ is electrical conductivity, κ is total thermal conductivity and T is absolute temperature.

In order to improve the performance of thermoelectric materials, we need to maximize the *ZT*, which requires high Seebeck coefficient, high electrical conductivity and low thermal conductivity. However, since these temperature dependent material parameters are coupled via the carrier concentration, it is often difficult to tune them independently. Therefore, we need to reach a subtle balance of these transport properties to get high *ZT* values.

The carrier concentration, which could be influenced by doping, has a strong effect on the thermoelectric transport properties. Figure 1.3.5.1 shows the dependence of the various thermoelectric properties on carrier concentration.

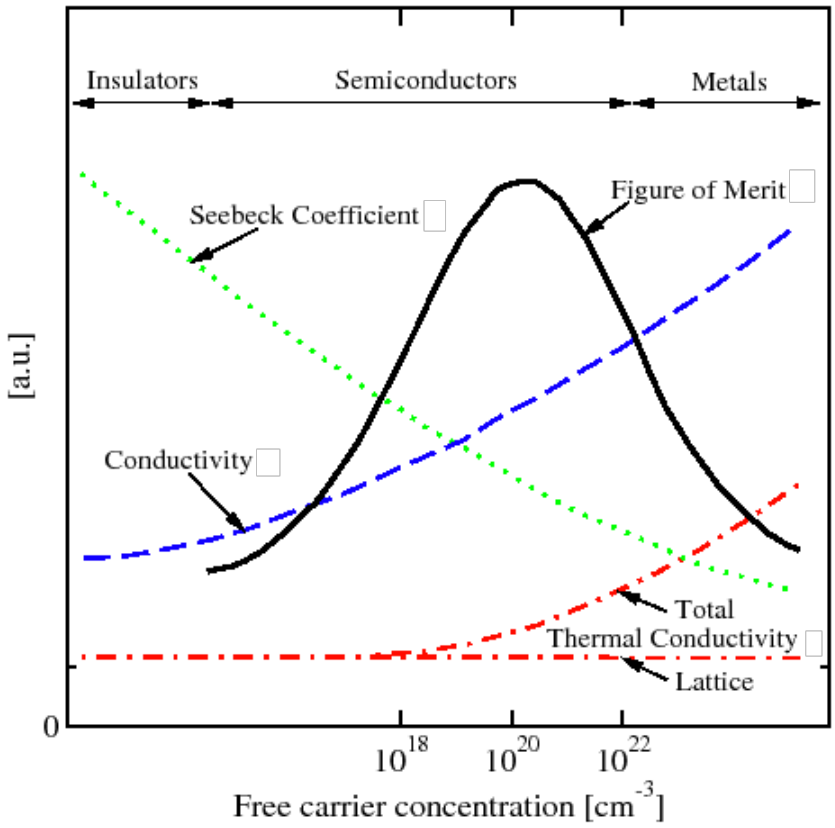

Figure 1.3.5.1 Dependence of electrical conductivity, Seebeck coefficient, total and lattice thermal conductivity on carrier concentration [6].

From Figure 1.3.5.1, we see that, good thermoelectric materials are heavily doped narrow gap semiconductors, with carrier concentrations between semiconductors and metals. The optimum carrier concentrations for these materials falls in the range from ~10^{19} cm^{-3} to ~10^{21} cm^{-3}.

1.4. Thermoelectric Devices

Thermoelectric devices are heat engines that contain an array of n and p-type thermoelectric materials connected thermally in series and electrically in parallel [1]. Thermoelectric devices can be used for either power generation or thermoelectric

refrigeration applications. Figure 1.4.1 shows a simple schematic representation of thermoelectric devices.

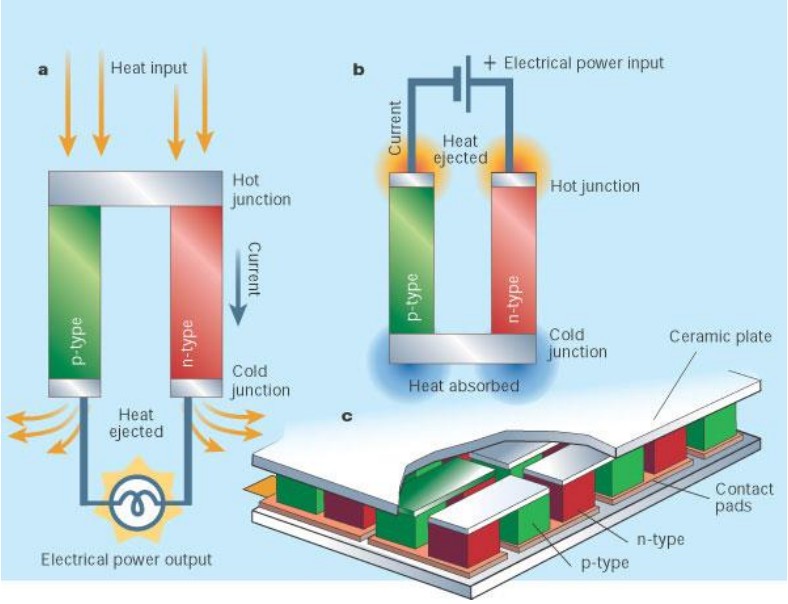

Figure 1.4.1 Thermoelectric device a) for power generation, b) for refrigeration application and c) a thermoelectric module consisting arrays of p and n-type materials connected electrically in series and thermally in parallel for either power generation or cooling applications [http://www.nature.com/nature/journal/v413/n6856/images/413577aa.2.jpg].

The thermal to electrical conversion efficiency of a thermoelectric device is defined by the ratio of electrical power output to the heat absorbed at the hot junction. The maximum efficiency, η of a thermoelectric device depends on two factors. These are the Carnot efficiency as any heat engine and the average *ZT* of the thermoelectric material.

$$\eta = \left(1 - \frac{T_c}{T_h}\right) \frac{(1+Z\bar{T})^{1/2} - 1}{(1+Z\bar{T})^{1/2} + \frac{T_c}{T_h}} \qquad (1.4.1)$$

Where $Z\bar{T}$ is average dimensionless figure of merit, and T_h and T_c are the hot-side andcold-side temperatures respectively.

In a similar fashion, the efficiency of a thermoelectric refrigerator is measured by the coefficient of performance (COP) of the device, which is also dependent on $Z\bar{T}$.

The coefficient of performance of a thermoelectric refrigerator is given by Equation 1.4.2.

$$COP = \frac{T_c[(1+Z\bar{T})^{\frac{1}{2}} - \frac{T_h}{T_c}]}{(T_h - T_c)[(1+Z\bar{T})^{1/2} + \frac{T_c}{T_h}]} \qquad (1.4.2)$$

In this case, T_c is the temperature of the source and T_h is the temperature of the sink and $T_c < T_h$. From Equation 1.4.1 and Equation 1.4.2, we can see that, the $Z\bar{T}$ plays a significant role and should be maximized in order to improve the efficiencies of both a thermoelectric generator and refrigerator. Figure 1.4.2 shows the efficiency of thermoelectric device as a function of temperature difference between source and sink for a material with different *ZT* values. For a temperature difference of 500 K and a *ZT* value ~10, the conversion efficiency of a thermoelectric generator is about 35%, comparable to the conversion efficiency of steam engine.

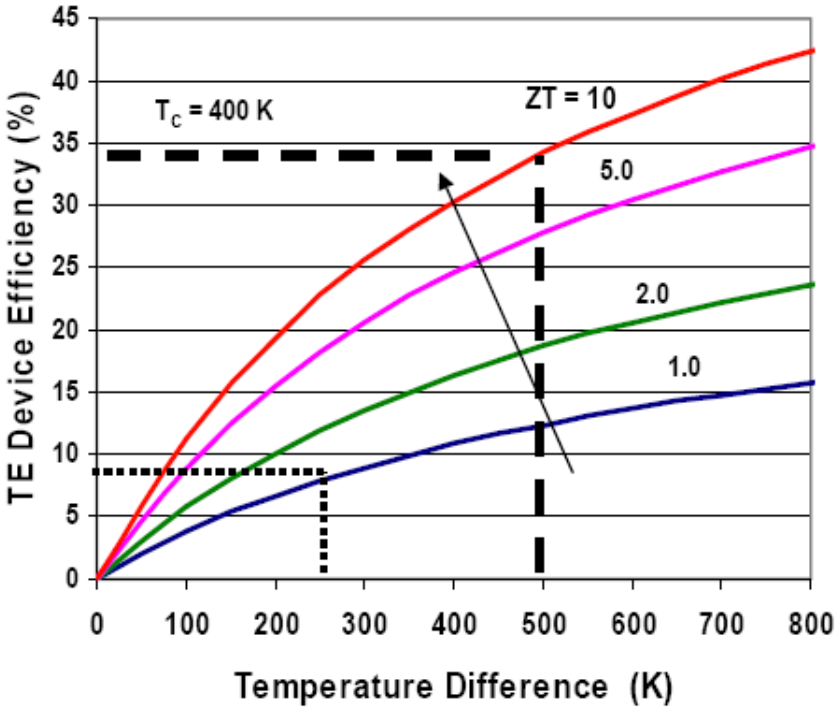

Figure 1.4.2 Efficiency of TE device as a function of temperature difference for material with different *ZT* values [http://farm3.static.flickr.com/2387/2076595330_b9dd520e51.jpg?v=0].

1.5. Improving the Thermoelectric Figure of merit (*ZT*)

Because the *ZT* is a function of the electrical conductivity (σ), Seebeck coefficient (*S*), and thermal conductivity (κ), achieving high *ZT* requires high σ, high *S,* and low κ.

1.5.1 Optimizing Seebeck Coefficient and Electrical Conductivity

The Seebeck coefficient of a thermoelectric material can be increased by different approaches, such as density of states modification as described in section 1.3.2, increasing the carrier effective mass, decreasing the carrier concentration and avoiding bipolar conduction. However, both lower carrier concentration and heavy carrier effective mass severely affect the electrical conductivity. The relationship between Seebeck

coefficient and electrical conductivity via effective mass and carrier concentration can be seen from a simple parabolic band model [19] with energy independent scattering given in Equation 1.5.1.1 and Equation 1.5.1.2 below.

$$S = \frac{8\pi^2 K_B^2}{3eh^2} m^* T \left(\frac{\pi}{3n}\right)^{2/3} \quad (1.5.1.1)$$

$$\sigma = \mu n e \quad (1.5.1.2)$$

Where m^* is effective mass, n is carrier concentration, μ is mobility, and e is electron charge. As seen in Equation 1.5.1.1 and Equation 1.5.1.2, the Seebeck coefficient and electrical conductivity have inverse relationship with the carrier concentration *n.* This requires optimizing the carrier concentration in order to get high Seebeck coefficient and high electrical conductivity. The optimum carrier concentration that yields both high Seebeck coefficient and electrical conductivity value is from ~10^{19} cm^{-3} to 10^{21} cm^{-3} [6]. Another important parameter worth to discuss is the effective mass. As can be seen in Equation 1.5.1.1, the heavier the effective mass the larger the Seebeck coefficient would be. However, carriers with heavier effective masses have smaller drift velocities, which lead to a reduction in electrical conductivity. The relationship between effective mass and mobility varies with band structure and scattering mechanism, also from material to material [6]. Since good thermoelectric materials found within a wide range of effective masses and mobilities from low mobility high effective mass (oxides [20], chalcogenides [21]) to high mobility, low effective mass semiconductors (SiGe, GaAs), unlike the carrier concentration, it is unknown which effective mass is optimum for good thermoelectric material.

1.5.2. Optimization of Thermal Conductivity

We have seen in section 1.3.4, that the thermal conductivity is a contribution of the lattice and electronic part. The electronic part of thermal conductivity can be expressed by the Wiedemann–Franz law as $\kappa_e = L\sigma T$, where L is Lorentz number, σ is electrical conductivity and T is absolute temperature. The lattice part of thermal conductivity is contributed by phonons and reducing the lattice part of thermal conductivity is achieved by scattering of phonons. There are three general strategies to reduce the lattice thermal conductivity [6]. The first is scattering of phonons in the unit cell by creating rattling structures, or point defects, such as vacancies, interstitials or by alloying [22]. The second technique is to use complex crystal structures to separate the electron crystal and phonon glass, which is approach of achieving a phonon glass without disrupting the electron crystal region [6,23]. The third strategy is inclusion of nanostructures that scatter phonons more than electrons [14]. Hence, by the above three methods and their combinations the lattice thermal conductivity can be minimized to enhance the *ZT*. In our research, we implemented some of these methods to maximize the thermoelectric transport properties of IV-VI chalcogenide materials.

1.6. IV-VI Chalcogenide Thermoelectric Materials

Chalcogenide IV-VI compounds are widely studied alloys for thermoelectric applications. Despite, recent interests in tin chalcogenide thermoelectric materials; the practicality for real device application is quite unpromising due to their poor mechanical properties and low *ZT* values in polycrystalline form. On the other hand, lead chalcogenides are better both in mechanical properties and *ZT* wise. They have decent *ZT* values at higher

temperature from 573 K to 873 K and are widely used for medium temperature power generation applications. In spite of increasing interest in these materials, their efficiency is limited by their lower average *ZT* across the temperature range from 300 K to 873 K. This is due to their respective lower *ZT* values near room temperature. Therefore, using lead chalcogenides for power generation application requires segmentation with other materials that have high *ZT* values near room temperature such as bismuth telluride alloys. However, segmentation has its own drawbacks, since the material suffers from interatomic mass diffusion, thermal expansion mismatch, and complexity of bonding that may eventually lead to material degradation and severe efficiency deterioration. Hence, to overcome these effects and use lead chalcogenide materials to span the whole temperature range, we need to improve the average *ZT* of lead chalcogenides by improving their *ZT*s near room temperature.

1.7. Objective and Organization of the Work

Thermoelectric materials have superior advantages from the perspective of providing clean energy by direct conversion of heat to electricity without moving parts. IV-VI chalcogenides, especially lead chalcogenides are potential thermoelectric materials for medium temperature power generation applications due to their decent *ZT* values from 573 K to 873 K. However, the efficiency of lead chalcogenides is low across the temperature range of 300 K to 873 K. This is due to the lower average *ZT* values associated with their corresponding lower *ZT* values near room temperature that need to be improved. On the other hand, lead chalcogenide compounds are toxic due to the presence of lead, which is a toxic element. The issue of toxicity has always been a

concern and is the main inspiration to the investigation of other lead-free compounds such as tin chalcogenides.

In this dissertation, I will address detail studies on improving the thermoelectric performance of lead chalcogenides by improving the *ZT* near room temperature and also investigate the thermoelectric performance of the newly discovered polycrystalline Sn-chalcogenides. The rest of this dissertation is organized as follows. In the second chapter, I will review the characterization techniques and principle of the measurement of thermoelectric transport properties. In the third, the fourth, and fifth chapters I will address the detail studies of improving the thermoelectric performance of lead cahlcogenides near room temperature. In the sixth and seventh chapters, I will discuss the thermoelectric performance of polycrystalline n and p-type tin chalcogenides and finally, I will conclude the dissertation with overall summary in the eighth chapter.

References

[1] D. M. Rowe and C.M. Bhandari, Modern Thermoelectrics, *Reston publishing Company, Inc.* 11480 Sunset Mills road, Reston, Virginia 22090, (1983).

[2] A. F. Ioffe, Semiconductor Thermoelements and Thermoelectric Cooling*, Infosearch*, London, (1957).

[3] W. Thomson, On a mechanical theory of thermoelectric currents, *Proceedings of the Royal Society of Edinburgh,* **91**, 8, (1851).

[4] Goldsmid, H. Julian, Introduction to Thermoelectricity *Springer Series in materials science* 2009**,** Editors: R. Hull, R. M. Osgood, Jr. J. Parisi and H. Warlimont**.**

[5] E. Altenkirch, *Phys. Z.* **12**, 920, (1911).

[6] G. J. Snyder and E.S. Tobber, *Nature Mater*. **7**, 105, (2008).

[7] M. S. Dresselhaus, & I. L. Thomas, *Nature,* **414,** 332, (2001).

[8] Global trends in sustainable energy investment, *Tech. Rep*. ISBN: 978-92-807-2859-0, DTI/0985/PA, *United Nations Environment Programme* (2007).

[9] G. Chen, M. S. Dresselhaus, G. Dresselhaus, J. P. Fleurial, & T. Caillat, *International Materials Review* **48**, 45, (2003).

[10] S. Riffat, and X. Ma, Thermoelectrics: a review of present and potential applications, *Applied Thermal Engineering* **23**, 913, (2003).

[11] G. S. Nolas ; J. Sharp; H. J. Goldsmid.Thermoelectrics : basic principles and new materials developments *Springer series in materials science* ; v. **45**, (2001).

[12] D. M. Rowe, (Ed.) CRC *Handbook of Thermoelectrics,* CRC Press, Boca Raton, FL, 157, (1995).

[13] M. S. Dresselhaus, Transport Properties of Solids, *solid state physics lecture note* part I, MIT (2001).

[14] M. S. Dresselhaus, *et al., Adv. Mater*. **19**, 1043–1053, (2007).

[15] L. D. Hicks, and M. S. Dresselhaus, *Physical Review B,* **47**, 12727, (1993).

[16] L. D. Hicks, and M. S. Dresselhaus, *Physical Review B,* **47**, 16631, (1993).

[17] J. P. Heremans, *et al*., *Energy Environ. Sci.,* **5**, 5510, (2012).

[18] Y. Pei, *et al*., *Nature,* 473, 66–69, (2011).

[19] M. Cutler, J. F. Leavy, and R. L. Fitzpatrick, *Phys. Rev.* A, **133,** 1143–A1152, (1964).

[20] K. Koumoto, I. Terasaki, and R. Funahashi, *Mater. Res. Soc. Bull*. **31**, 206–210, (2006).

[21] G. J. Snyder, T. Caillat, and J. P. Fleurial, *Phys. Rev.* B **62**, 10185, (2000).

[22] C. M. Bhandari, in CRC Handbook of Thermoelectrics, (ed. D. M. Rowe), 55–65, CRC, Boca Raton, (1995).

[23] G. A. Slack, in CRC Handbook of Thermoelectrics (ed. M. Rowe,) 407–440, CRC, Boca Raton, (1995).

CHAPTER 2: CHARACTERIZATION OF THERMOELECTRIC MATERIALS

2.1. Introduction

In order to characterize the performance of thermoelectric materials, and develop devices, high-precision measurements of *ZT* as well as good estimation of errors is essential. Since *ZT* depends on the electrical and thermal transport properties, the measurement of these properties should be done to the highest possible level of accuracy. The measurements should be repeatable on the same sample and on new samples of same chemical composition and preparation techniques. In measurement of the transport properties, several factors may lead to unusual and inaccurate results. These include but are not limited to bad thermocouples [1], bad contacts, improper calibrations and chemical composition changes during measurement such as oxidations and evaporation of some elements from the sample. For example, excessively large contacts in resistivity and Hall measurement lead to inaccurate Seebeck coefficient enhancement [1-4] and early measurements overestimated the high temperature thermal conductivities of lead chalcogenides [1,5,6]. This overestimation of the thermal conductivity resulted in underestimation of the *ZT* values for decades. Transport property measurements may vary from material to material. For example, materials with high symmetry crystal structures like lead tellurides, lead selenides and their alloys have isotropic transport properties and measurement of the transport properties in one direction is sufficient to characterize the material. On the other hand, materials with low crystal symmetry like SnSe, have anisotropic transport properties and a transport property measurement done in one direction is insufficient to characterize such materials. One of the most important aspects

of characterization of thermoelectric properties is to identify and estimate the errors in the measurement. Therefore, thermal and electrical transport properties should be measured with extra care and maximum possible accuracy to avoid any error that could lead to underestimating or overestimating of *ZT*.

2.2. Characterization Techniques

The electrical and thermal transport properties of all our samples are characterized in the following way. Seebeck coefficient (S) and electrical conductivity (σ) were measured using a static direct current method and a four-point direct current switching method respectively, on a commercial (ZEM-3, ULVAC) system. The room-temperature Hall carrier concentration (n_H) was measured using a Quantum Design Physical Properties Measurement System. The thermal diffusivity (α) was measured by a laser flash analyzer system (LFA 457, Netzsch), the specific heat (C_p) was measured on a differential scanning calorimetry thermal analyzer (DSC 404 C, Netzsch), and the volumetric density (D) was measured by the Archimedes method. The thermal conductivity was calculated by $\kappa = D\alpha C_p$. Our measurements are accurate within 12 % for *ZT* and 10 % for power factor, due to a 3 % error in electrical conductivity, a 5 % error in Seebeck coefficient, and a 7 % error in thermal conductivity.

2.3. Electrical Resistivity Measurements

Electrical resistivity measurement is done by the four-point probe method using commercial ZEM-3 ULVAC apparatus shown in Figure 2.3.1.

In this apparatus the thermocouples would be in direct contact with the sample, reducing the distance between the electrical and thermal contacts.

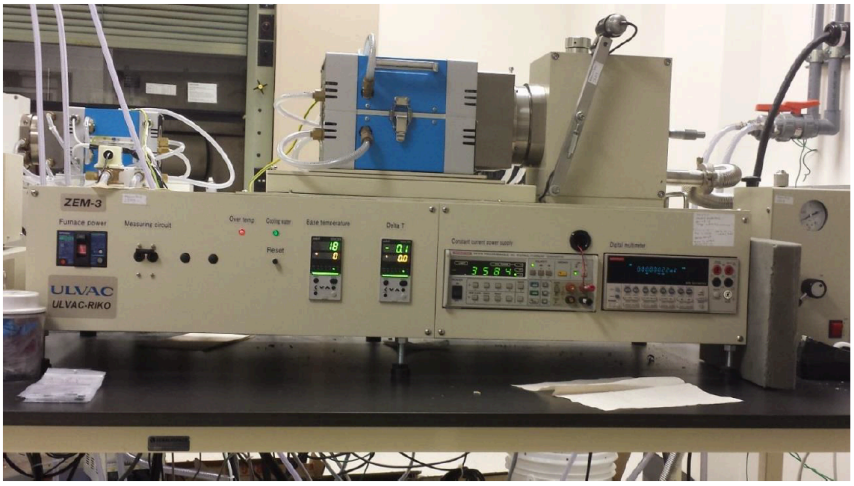

Figure 2.3.1 Commercial ZEM-3 ULVAC system for electrical resistivity and Seebeck coefficient measurement.

The four-point probe method is one of the most widely used methods for electrical resistivity and Seebeck coefficient measurements [1]. The samples are cut in to a parallel piped bar and kept between the heat source and heat sink. Figure 2.3.2 represents a simple schematic of the four-point probe method.

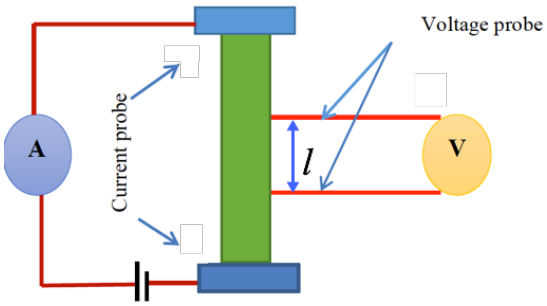

Figure 2.3.2 simple schematic representation of the four-probe method to measure electrical resistivity.

In the measurement, the thermocouples and voltage leads are placed against the side of the sample that allow concurrent measurement of electrical resistivity and Seebeck coefficient. It is very important to minimize the electrical and thermal contact resistances and make sure the temperature and voltage are measured at the same point. In the measurement process current is passed from one end to the other while the voltage is measured at the two intermediate points. The resistivity is then calculated from the cross-sectional area, the measured four-point resistance, and the separation length of the voltage contacts by the formula given in Equation 2.3.1.

$$\rho = \frac{RA}{l} = \frac{A}{l}\frac{dV}{dI} \qquad (2.3.1)$$

Where ρ is resistivity, l is length of the separation of voltage probes, A is cross-sectional area of the sample and R is the resistance calculated from the slope of voltage versus current curve. The electrical conductivity is calculated from the inverse of the resistivity (ρ^{-1}) at different temperatures. The resistivity is sensitive to errors in the geometric factor of A/l and the error in ZEM-3 is about 3 %.

2.4. Seebeck Coefficient Measurement

The Seebeck coefficient is the ratio of electric field gradient to applied temperature gradient. The principle of measurement of Seebeck coefficient is conceptually simple, but in reality it can be difficult to measure accurately. In a typical measurement, the temperature is varied around a constant average temperature and the slope of the voltage (V) versus temperature difference (ΔT) curve gives the Seebeck coefficient. The Seebeck coefficient can be measured in two ways.

The first way is by stabilizing the temperature difference before each measurement also called steady-state measurement [7-9] and the second way is by conducting the measurement while the temperature difference is varied slowly [10-13], this is called quasi-steady-state method. In a recent study, little difference was found between steady-state and quasi-steady-state measurements when good thermal and electrical contact is ensured [1,14]. In our experiment, we stabilize the temperature before each measurement (steady-state measurement) using the commercial ZEM-3 shown in Figure 2.3.1. The principle of Seebeck coefficient measurement is by the four-point method as shown in Figure 2.4.1. The bar-shaped sample is placed between the two heaters and the thermocouples A, B, C and D are in contact with the sample. The thermocouples A and B are made up of the same material and similarly C and D are also made up of the same material but different from A and B. The thermocouples C and D measure the temperature difference whereas A and B measure the potential difference at the same point. The temperature is varied around a constant temperature and the Seebeck coefficient is calculated from the slope of the voltage versus the change in temperature by $S = \frac{V}{\Delta T}$ shown in Figure 2.4.2. The measured raw data is corrected for constant offset voltages by using the slope of several (ΔT, V) points for extracting the Seebeck coefficient [7,11,15-16]. The temperature dependence of the Seebeck coefficient is measured by changing the temperature via the heater.

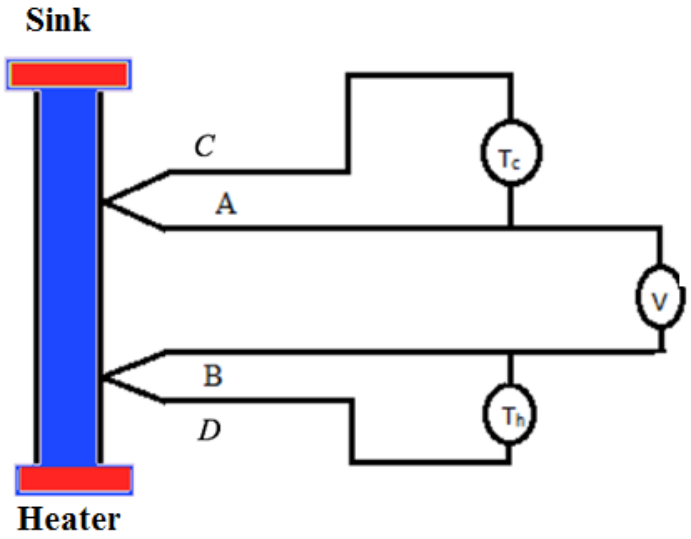

Figure 2.4.1 Schematic setup of Seebeck coefficient measurement using four-point method.

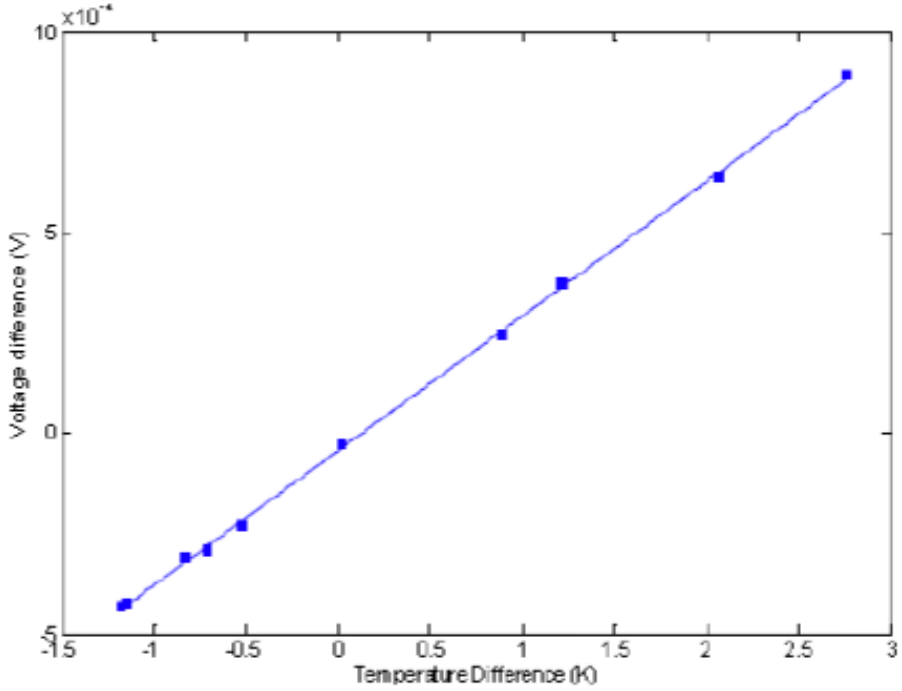

Figure 2.4.2 V-ΔT curve for Seebeck coefficient measurement.

Since it can only be measured relatively between two materials, the extent of accuracy of Seebeck coefficient measurement is usually difficult to tell accurately. However a variation of about 5 % can generally be expected at room temperature [17-19] and in ZEM-3 the total error is also up to 5 %.

2.5. Thermal Conductivity Measurement

There are many methods to measure the thermal conductivity of materials, such as the thermal Vander Pauw [20] method and the Harman method [21-22]. The most frequently used method is the flash diffusivity [23-25]. In this method, the thermal conductivity (κ) is calculated from the diffusivity (α), density (*d*), and specific heat at constant pressure (C_p) by Equation 2.5.1.

$$\kappa = \alpha d C_p \qquad (2.5.1)$$

In measuring diffusivity, a short heat pulse by laser flash is applied to one side of the sample while the temperature of the other side is measured using infrared (IR) detector. The temperature raises to a maximum value T_{max} and return back. The thermal diffusivity is calculated from the half time $T_{1/2}$, that is the time the temperature can reach half of T_{max} as shown in Figure 2.5.1.

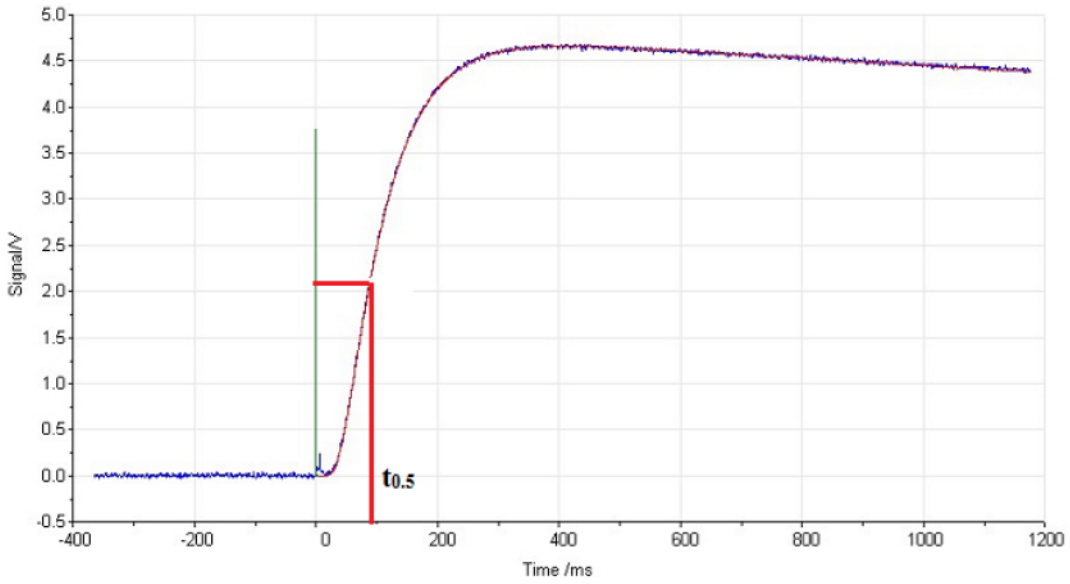

Figure 2.5.1 $T_{1/2}$ from the temperature-time curve measured by IR detector.

The thermal diffusivity can be calculated from the thickness of the sample x and the half time $T_{1/2}$ by Equation 2.5.2.

$$\alpha = \frac{1.38\, dx^2}{\pi T_{1/2}} \qquad (2.5.2)$$

This calculation is based on the assumption that the heat flows only axially and no heat loss. The schematic picture of thermal diffusivity measurement is given in Figure 2.5.2.

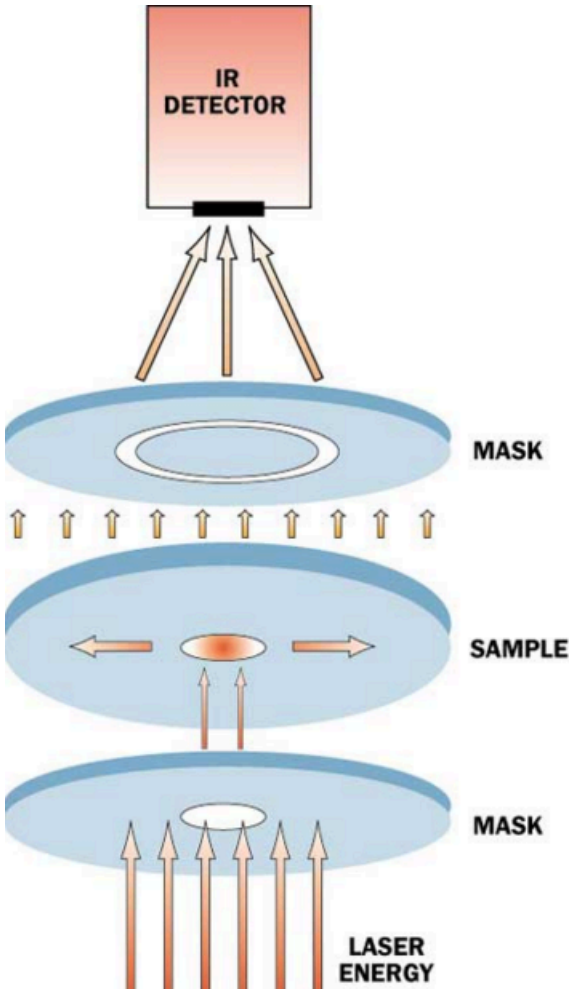

Figure 2.5.2 Simple sketch of laser flash measurement system [http://s3.electronics-cooling.com/legacy_images/2002/05/2002_may_a4_figure4.jpg].

The heat loss to the sample boundaries is minimized by the quickness of the heat pulse, and the thickness of the sample is smaller than the diameter of the sample. We measured the diffusivity by commercial (LFA 457, Netzsch) apparatus shown in Figure 2.5.3. In our measurement of the diffusivity, we used a disc-shaped sample of diameter ~ 12.7 mm and sample thickness from 1 to 2 mm. The heat to the faces is corrected by Cowan correction, which still assumes axial flow.

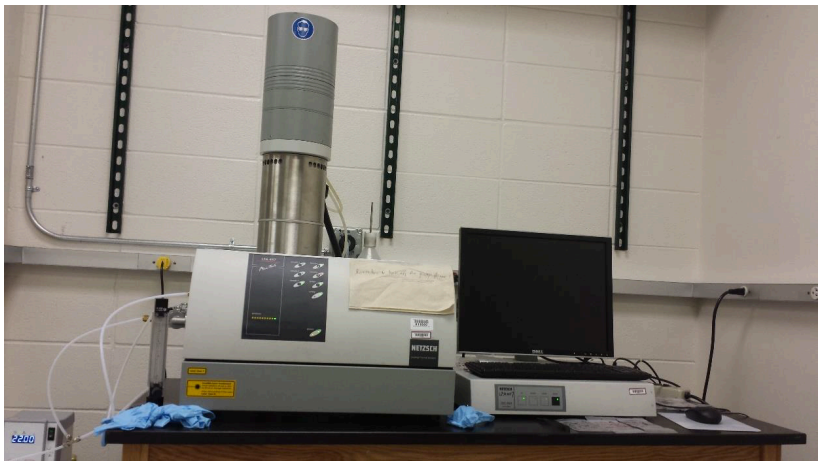

Figure 2.5.3 Laser flash system [LFA 457, Netzsch].

We also carbon coated the samples to ensure a high emissivity and hence good absorption of laser pulse and maximum detector signal. A thermocouple in contact with the sample measures the temperature of the sample and the temperature of the environment is changed by a heater in the furnace for measurement of diffusivity at different temperatures. The equipment is automated to a computer and the data is collected from the computer. The results from laser flash diffusivity are accurate compared to steady-state method and PPMS data since it is less susceptible to errors from radiation loss corrections [1]. The error in thermal conductivity measurement using flash diffusivity method is up to 7 %.

2.6. Specific Heat Capacity Measurement

In order to calculate the thermal conductivity, first we need to measure the specific heat capacity of the samples. Even though, some conventional flash diffusivity measurement systems can estimate the heat capacity relative to some standard, these results are often inaccurate and often lead to underestimation of the thermal conductivity [1]. Recently,

differential scanning calorimetry (DSC) is the most frequently used apparatus to measure specific heat (C_p). In DSC heat capacity is measured relative to a standard. Before the actual measurement is done, first a base line is measured with empty sample holder and then the sample and the reference is measured. In DSC measurement, the reference should be chosen to give a signal close to the measured sample to minimize errors. Figure 2.6.1 shows the DSC apparatus for C_p measurement.

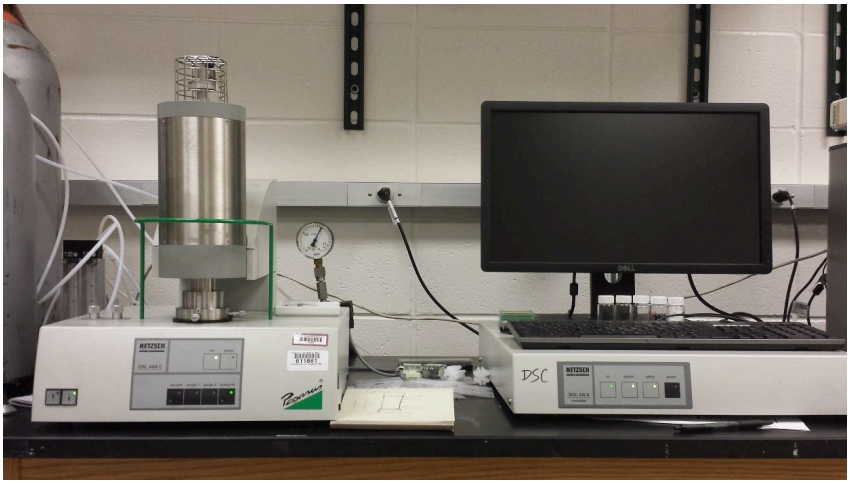

Figure 2.6.1 DSC 400C (Netzsch) for heat capacity measurement.

DSC measures the specific heat capacity by heating the sample at constant rate and measuring the temperature difference between the sample and the sapphire reference. The reference and the sample crucibles are placed on a sample carrier. The temperature is detected by thermocouples in contact with each crucible and one thermocouple is shared between the crucibles allowing the temperature difference to be measured as voltage. In our measurement, we used a small disc sample of ~ 6 mm diameter and thickness from 0.6 mm to 1 mm. These sample dimensions are comparable to the dimensions of the reference sample in

order to get results that are more accurate. As already pointed out, three measurements are needed for calculating the specific heat. First, the base line is recorded with empty sample holders to avoid system bias from the data, then the reference sample with well-defined specific heat C_p is tested for comparison to an experimental sample and finally the sample is measured. In our experiment the reference sample is sapphire sample and the specific heat is calculated from the following formula.

$$C_p = \frac{Signal\ difference\ (sample-baseline)}{sample\ mass*heating\ rate*sensitivity} \quad (2.6.1)$$

Where sensitivity is calculated from the reference sample by;

$$Sensitivity = \frac{signal\ difference(sapphire-baseline)}{(mass\ of\ sapphire)*heating\ rate*sapphire\ C_p} \quad (2.6.2)$$

The primary sources of error in DSC are operation or inexperience error, base line shift and inappropriate reference sample. These errors are controllable and the C_p of our samples can be measured within an error of 2 %.

2.7. Carrier Concentration Measurement

Even though carrier concentration is not needed to calculate *ZT*, it is a very important parameter since all transport properties are strongly related to it. Carrier concentration provides important information for the cause of changes of thermoelectric transport properties. The carrier concentration in heavily doped semiconductors like thermoelectric materials is obtained by calculating from the Hall coefficient. If metals or heavily doped semiconductors carrying electric current *I* are subjected to external magnetic field, the charge carriers will be deflected by Lorentz force and accumulated to one side of the sample. An electric field is then buildup perpendicular to both the magnetic field and the

current direction. Consequently, a voltage is developed perpendicular to both the current direction and magnetic field direction. This voltage is called the Hall voltage V_H. Figure 2.7.1 shows a simple schematic representation of Hall effect on a rectangular sample.

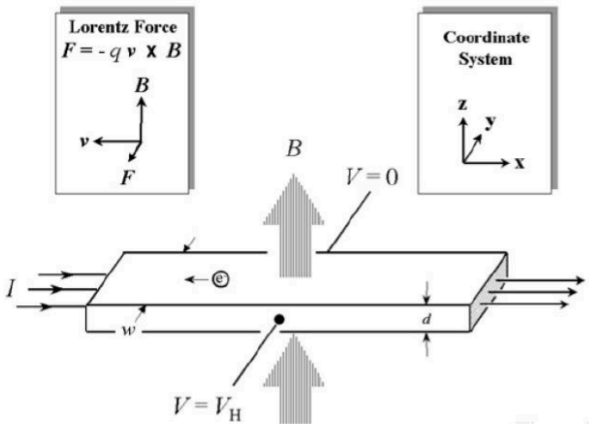

Figure 2.7.1 Schematic of Hall effect in a thin semiconducting bar with four Ohmic contacts [http://www.nist.gov/pml/div683/images/fig1s.jpg].

We measured the Hall coefficient of our samples using a quantum design physical properties measurement system (Quantum design PPMS) apparatus shown in Figure 2.7.2.

Figure 2.7.2 PPMS (Quantum Design) for carrier concentration and mobility measurement.

The Hall coefficient R_H and Hall resistance R_C are calculated from the Hall voltage and the current as shown below.

$$R_C = \frac{V_H}{I} \qquad (2.7.1)$$

$$R_H = \frac{R_C d}{B} \qquad (2.7.2)$$

The Hall carrier concentration *n* is then calculated based on the free electron model from the Hall coefficient by the following equation.

$$n = \frac{1}{eR_H} \qquad (2.7.3)$$

Where *e* is electron charge and *d* is the thickness of the sample. The Hall carrier concentration is positive for holes and negative for electrons. The Hall mobility also can be calculated by $\mu_H = \frac{R_H}{\rho}$, if the resistivity ρ is known.

References

[1] K. A. Borup *et al., Energy Environ. Sci.,* **8**, 423–435, (2015).
[2] T. C. Harman, D. L. Spears and M. P. Walsh, *J. Electron. Mater.*, **28**, L1–L5, (1999).
[3] T. C. Harman, P. J. Taylor, D. L. Spears and M. P. Walsh, *J. Electron. Mater.,* **29**, L1–L2, (2000).
[4] C. J. Vineis, T. C. Harman, S. D. Calawa, M. P. Walsh, R. E. Reeder, R. Singh and A. Shakouri, *Phys. Rev.* B: *Condens. Matter Mater. Phys*., **77**, 235202, (2008).
[5] H. Wang, Y. Pei, A. D. LaLonde and G. J. Snyder, *Adv. Mater*., **23**, 1366–1370, (2011).
[6] H. Wang, Y. Pei, A. D. LaLonde and G. J. Snyder, *Proc. Natl. Acad. Sci.* U. S. A., 109, 9705–9709, (2012).
[7] J. Martin, *Rev. Sci. Instrum*., **83**, 065101–065109, (2012).
[8] P. H. M. Bottger, E. Flage-Larsen, O. B. Karlsen and T. G. Finstad, *Rev. Sci. Instrum.,* **83**, 025101, (2012).
[9] R. L. Kallaher, C. A. Latham and F. Shari, *Rev. Sci. Instrum*., **84**, 013907, (2013).
[10] S. Iwanaga, E. S. Toberer, A. LaLonde and G. J. Snyder, *Rev.Sci. Instrum.,* **82**, 063905 (2011).
[11] L. J. Vander Pauw, *Philips Res. Rep.,* **13**, 1, (1958).
[12] C. Wood, D. Zoltan and G. Stapfer, *Rev. Sci. Instrum.,* **56**, 719–722, (1985).
[13] A. Guan, H. Wang, H. Jin, W. Chu, Y. Guo and G. Lu, *Rev. Sci. Instrum.,* **84**, 043903 (2013).
[14] J. Martin, *Meas. Sci. Technol*., **24**, 085601, (2013).
[15] J. Martin, T. Tritt and C. Uher, *J. Appl. Phys.*, **108**, 121101, (2010).
[16] J. de Boor and E. Muller, *Rev. Sci. Instrum*., **84**, 065102, (2013).
[17] H. Wang, *et al., J. Electron. Mater.,* **42**, 654–664, (2013).
[18] N. D. Lowhorn, *et al., Appl. Phys. A: Mater. Sci. Process.,* **94**, 231–234, (2009).
[19] Z. Lu, N. D. Lowhorn, W. Wong-Ng, W. Zhang, M. Otani, E. E. Thomas, M. L. Green and T. N. Tran, *J. Res. Natl. Inst.Stand. Technol.*, **114**, 37–55, (2009).
[20] J. de Boor and V. Schmidt, *Adv. Mater.,* **22**, 4303–4307, (2010).
[21] T. C. Harman, J. H. Cahn and M. J. Logan, *J. Appl. Phys.,* **30**, 1351–1359, (1959).
[22] X. Y. Ao, J. de Boor and V. Schmidt, *Adv. Energy Mater.,* **1**, 1007–1011, (2011).
[23] J. W. Vandersande, A. Zoltan and C. Wood, *Int. J. Thermophys*., **10**, 251–257, (1989).
[24] C. B. Vining, A. Zoltan and J. W. Vandersande, *Int. J. Thermophys.*, **10**, 259–268, (1989).
[25] W. J. Parker, R. J. Jenkins, C. P. Butler and G. L. Abbott, *J. Appl. Phys.*, **32**, 1679–1684, (1961).

CHAPTER 3: THERMOELECTRIC PERFORMANCE OF Cr-DOPED PbSe

3.1. Introduction

Lead chalcogenide thermoelectric (TE) materials have drawn increasing attention due to their high peak dimensionless figure of merit (*ZT*) at higher temperatures [1-6]. However, the TE device efficiency (η) depends not on the peak *ZT,* rather it depends on the average *ZT* of the TE material over the temperature range under which the device is operating. Mathematically the maximum efficiency, η_{max} of a TE device is expressed by Equation 3.1.1.

$$\eta_{max} = \left(1 - \frac{T_c}{T_h}\right)\frac{(1+ZT_{av})^{1/2}-1}{(1+ZT_{av})^{1/2}+\frac{T_c}{T_h}} \qquad (3.1.1)$$

Where T_{av} is average temperature, T_h is the temperature at the hot junction and T_C the temperature at the cold junction [7-11].

Segmented leg approach; which is a method of combining in series different thermoelectric materials with different peak *ZT* temperatures, may boost the efficiency a thermoelectric device [12-16]. However, devices from segmented legs suffer from the added complexity of bonding, interfacial mass diffusion, and thermal expansion mismatch that gradually lead to adverse device degradation and severe efficiency reduction. It is therefore, more plausible to use a single material to span the whole temperature range of operation. In the case of lead chalcogenides, peak *ZT*s normally appear at around 573-873 K [1-6]. The *ZT* curve of lead chalcogenides increases steeply from room temperature to the peak *ZT* temperature, resulting in relatively low average *ZT*, especially for PbSe [17-18]. Through the combination of nanostructures and complex

band structure, a better average *ZT* was obtained in Na-doped p-type PbTe/Ag_2Te (300-750 K) [19] compared with pure Na-doped PbTe [20] and La-doped n-type PbTe/Ag_2Te [21]. A relatively better average *ZT* was also achieved in Na-doped $Pb_{0.97}Mg_{0.03}Te$ (300-750 K) due to the stabilization of the optimal carrier concentration [22]. In comparison to PbTe, PbSe is abundant and cheaper, however, its average *ZT* needs to be further improved to substitute PbTe for TE device applications. Among all reported n-type and p-type PbSe systems [4,17,18,23-26], Al-doped n-type PbSe has the highest average *ZT*, which may be due to nanostructures that reduce thermal conductivity and resonant states that improved the Seebeck coefficient [26]. Cr was also reported as effective dopant in increasing the Seebeck coefficient and power factor of PbTe. However, resonant effect was not observed, rather it was found to form a deep level of 100 meV above the bottom of the conduction band and pinned the Fermi level [27-31]. A similar effect was also found in Cr-doped PbSe at energy of 124 meV above the bottom of the conduction band [32]. In our work, we have not observed any resonant scattering in Cr doped PbSe. However, we observed interesting features on its room temperature thermoelectric properties. In this chapter, we will see the systematic study of different transition element doped n-type PbSe (Ti-[33-35], V-, Cr-, Nb- and Mo-doped PbSe) with enhanced power factors and *ZT*s (below 600 K). Cr-doped PbSe, in particular also has a peak $ZT > 1$, promising to have a potential device efficiency of ~12 % for acold-side temperature of 300 K and a hot-side temperature of 773 K, higher than those of all other reported n-type PbSe thermoelectric materials [4,17,18,23-26].

3.2. Experimental Methods

We prepared n-type PbSe with different doping elements $A_xPb_{1-x}Se$ (A: Ti, V, Cr, Nb, and Mo, $x \leq 0.02$) by melting, hand milling, and hot pressing. Ingots of samples of $Cr_xPb_{1-x}Se$ with (x = 0.0025, 0.005, 0.0075, and 0.01), were prepared in a carbon coated quartz tube from high-purity elements (Cr pieces, 99.99%; Pb granules, 99.99%; Te chunks 99.999%; Se granules, 99.99%) according to their stoichiometric weights. The tubes were evacuated to ~3×10^{-4} Pa and sealed, then slowly heated to 1000-1100 ^{o}C at a rate of 200 ^{o}C/hour and then held at that temperature for 6 hours, then slowly cooled at the same rate to 650 ^{o}C and kept there for 50 hours, and then finally cooled to room temperature. The ingots obtained from this procedure were cleaned and hand milled in a glove box with an argon environment. The hand-milled powder was then loaded into a half inch graphite die, hot pressed at 600 ^{o}C for 2 minutes, air cooled, polished, cleaned, and cut to a desired shape for characterization. X-ray diffraction spectra analysis was conducted on a PANalytical multipurpose diffractometer with an X'celerator detector (PANalytical X'Pert Pro). The electrical resistivity (ρ) and Seebeck coefficient (S) were simultaneously measured on a commercial system (ULVAC ZEM-3). The thermal conductivity k was calculated using $k = D\alpha C_p$, where D is volumetric density determined by the Archimedes method, α the thermal diffusivity obtained on a laser flash apparatus (Netzsch LFA 457), and C_p the specific heat measured on a differential scanning calorimetry thermal analyzer (Netzsch DSC 404 C). The Hall Coefficient R_H at room temperature was measured using PPMS (Quantum Design Physical Properties Measurement System). The Hall carrier concentration n_H and Hall mobility μ_H were

calculated using $n_H = 1/(eR_H)$ and $\mu_H = \sigma R_H$, respectively. The uncertainty for the electrical conductivity is 3%, the Seebeck coefficient 5%, the thermal conductivity 7% (comprising uncertainties of 4% for the thermal diffusivity, 5% for the specific heat, and 3% for the density), so the combined uncertainty for the power factor is 10% and that for *ZT* value is 12%. Error bars were not used in the figures to increase the readability of the curves.

3.3. Thermoelectric Properties of Cr- doped PbSe

Single-phase $Cr_xPb_{1-x}Se$ was prepared with different Cr doping concentrations (x = 0.0025, 0.005, 0.0075, and 0.01), which is indexed to the face-centered structure (space group $Fm\bar{3}m$) and shown in Figure 3.3.1. Due to the large difference in the ionic radius of Pb^{2+} (1.20 Å) and Cr^{3+} (0.52 Å), all peaks shift right with increasing x. Even though secondary phases $Cr_{3+\delta}Te_4$ and Cr_2Te_3 were observed when PbTe was doped with more than 0.4 atm. % Cr [30], no impurity phase was formed in Cr-doped PbSe even up to 1 atm. % doping level.

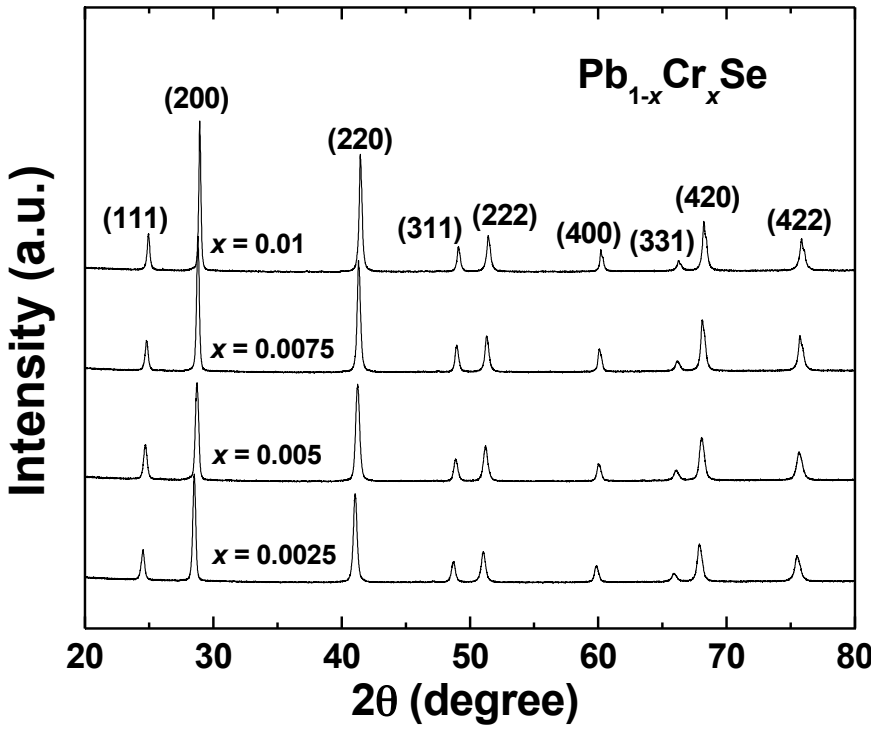

Figure 3.3.1 XRD patterns for $Pb_{1-x}Cr_xSe$ (x = 0.0025, 0.005, 0.0075, and 0.01).

Normally, lead chalcogenides are favorable for hot-side temperatures at 673-873 K. $(Bi_{1-x}Sb_x)_2(Te_{1-y}Se_y)_3$ is usually considered over the temperature range from 300 to 473 K. Therefore, a combination of $(Bi_{1-x}Sb_x)_2(Te_{1-y}Se_y)_3$ with mid to high temperature TE materials will yield a higher device efficiency across a large temperature range. We found comparable TE properties in PbSe based materials to those in $Bi_2Te_{2.7}Se_{0.3}$ from 300 to 473 K when Cr was doped into PbSe to enable higher average ZT across a large temperature range (300-873 K). Figure 3.3.2 (a-f) presents the temperature dependence of electrical conductivity, Seebeck coefficient, power factor, thermal diffusivity, specific heat capacity, total thermal conductivity and lattice thermal conductivity for $Cr_xPb_{1-x}Se$ (x = 0.0025, 0.005, 0.0075, and 0.01) compared with reported data on n-type $Bi_2Te_{2.7}Se_{0.3}$

[36]. All samples show metallic transport behavior. The electrical conductivity is higher than $Bi_2Te_{2.7}Se_{0.3}$, and the Seebeck coefficient is comparable with $Bi_2Te_{2.7}Se_{0.3}$ below 473 K. The room temperature power factor reaches ~ 3.0×10^{-3} W m^{-1} K^{-2}, higher than all the reported doped PbSe and even $Bi_2Te_{2.7}Se_{0.3}$ [4,17,18,23-26,36]. Even though, a high room temperature power factor of ~ 3.85×10^{-3} W m^{-1} K^{-2} was reported in the 1.45 atm. % Cr-doped PbTe [28], the overall *ZT* is not favorable due to the high thermal conductivity. PbSe has been shown to have lower lattice thermal conductivity than PbTe, which is attributed to the higher degree of anhamonicity of lattice vibrations in PbSe [17]. The lattice thermal conductivity of Cr-doped PbSe was calculated by subtracting the charge carrier thermal conductivity from total thermal conductivity ($k_L = k_{total}-k_e = k_{total}-L\sigma T$), where *L* is the Lorenz number calculated using a two-band model [18]. Combined with this relatively lower thermal conductivity, the room temperature *ZT* reaches ~0.4 (shown in Figure 3.3.3), much higher than the previous In-doped n-type PbSe [18], but still lower than the room temperature *ZT* of $Bi_2Te_{2.7}Se_{0.3}$ [36]. The *ZT* values continuously increase and reach ~1.0 at ~573 K for $Cr_{0.0075}Pb_{0.9925}Se$ and ~673 K for $Cr_{0.005}Pb_{0.995}Se$ and stay above 0.9 from 573 K to 773 K, which strongly increases the average *ZT* of PbSe based materials, as will be discussed later.

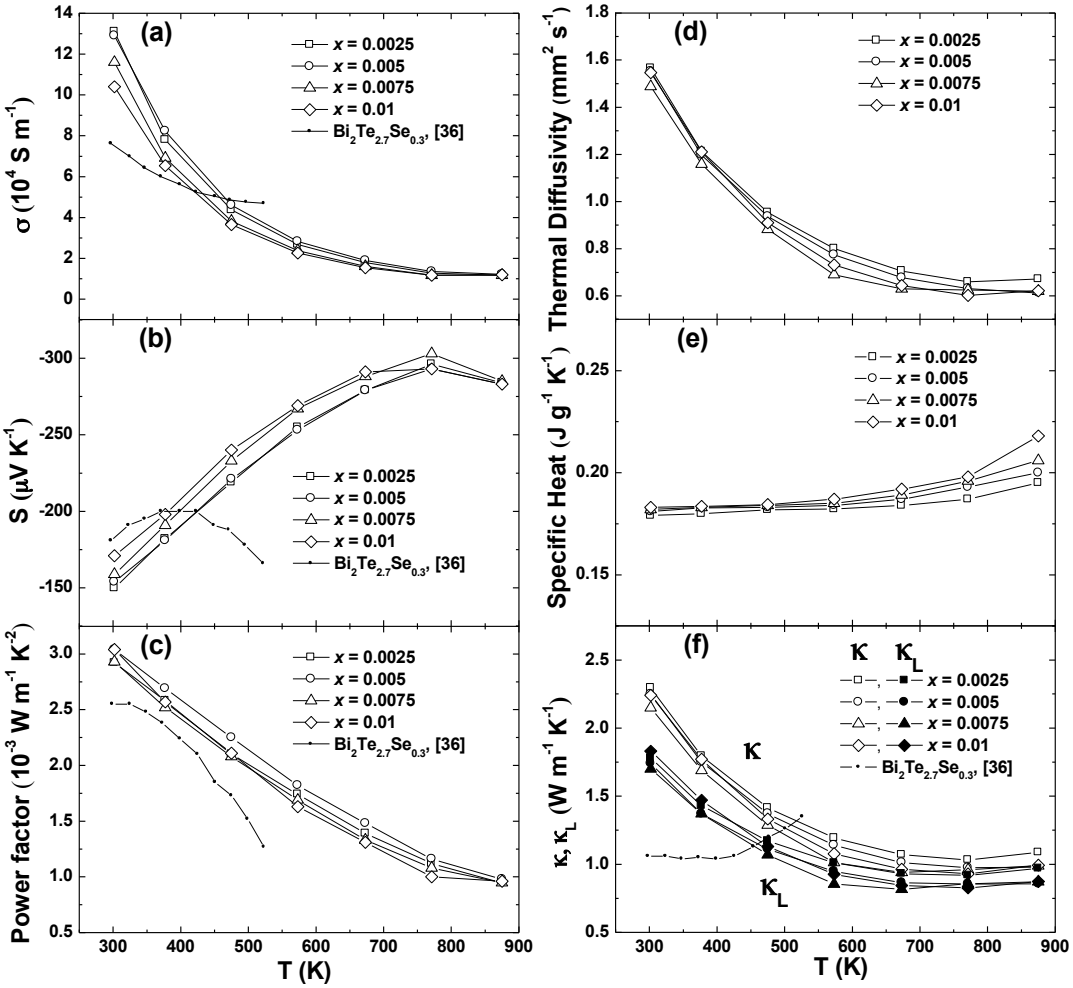

Figure 3.3.2 Temperature dependence of (a) electrical conductivity, (b) Seebeck coefficient, (c) power factor, (d) thermal diffusivity, (e) specific heat and (f) total thermal conductivity and lattice thermal conductivity for $Cr_xPb_{1-x}Se$ (x = 0.0025, 0.005, 0.0075, and 0.01) in comparison with reported data on n-type $Bi_2Te_{2.7}Se_{0.3}$ by Yan *et al*., [36] (small solid circles).

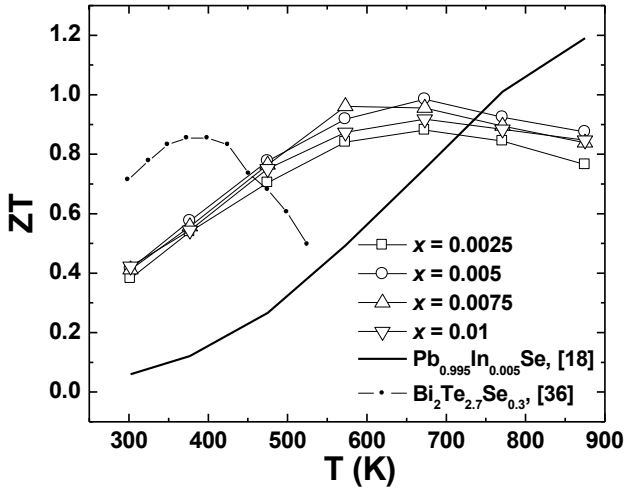

Figure 3.3.3 Temperature dependence of *ZT* for $Pb_{1-x}Cr_xSe$ (x = 0.0025, 0.005, 0.0075, and 0.01) in comparison with reported data on $Bi_2Te_{2.7}Se_{0.3}$ by Yan *et al.,* [36] (small solid circles) and our previous data on In-doped PbSe [18] (solid line).

Following a similar method as in Cr-doped PbSe, we also doped other transition metals close to Cr (in the periodic table of elements) into PbSe. The temperature dependence of the electrical conductivity, Seebeck coefficient, power factor, thermal diffusivity, specific heat, total thermal conductivity, and lattice thermal conductivity for optimized $Pb_{1-x}A_xSe$ (A: Ti, V, Cr, Nb, and Mo) (x = 0.005 or 0.01) in comparison with reported data on In-doped PbSe [18] (solid line) are shown in Figure 3.3.4. The samples still show the typical behavior of degenerate semiconductors. It is interesting that the TE properties of all the transition metal-doped PbSe show a consistent trend, but different from the previous two categories doping (like Ga-, In-, and Br-, Cl-doped PbSe [18,24,25]). The electrical conductivity of transition metal-doped PbSe is lower and the Seebeck coefficient is higher across the whole temperature range (300–873 K). The power factor decreased with increasing temperature.

The highest room-temperature power factor is ~3.3×10^{-3} W m^{-1} K^{-2} for 1 atm. % Mo-doped PbSe. Because of the lower electrical conductivity, the total thermal conductivity is also lower compared with In-doped PbSe [18]. With a lower thermal conductivity and a higher power factor at lower temperatures, the *ZT* values of all the studied samples are higher than In-doped PbSe [18] below 600 K (shown in Figure 3.3.5). The highest room temperature *ZT* is ~0.5 for 1 atm. % Mo-doped PbSe and the highest peak *ZT* is ~1.0 for 0.5 atm. % Cr-doped PbSe at about 673 K.

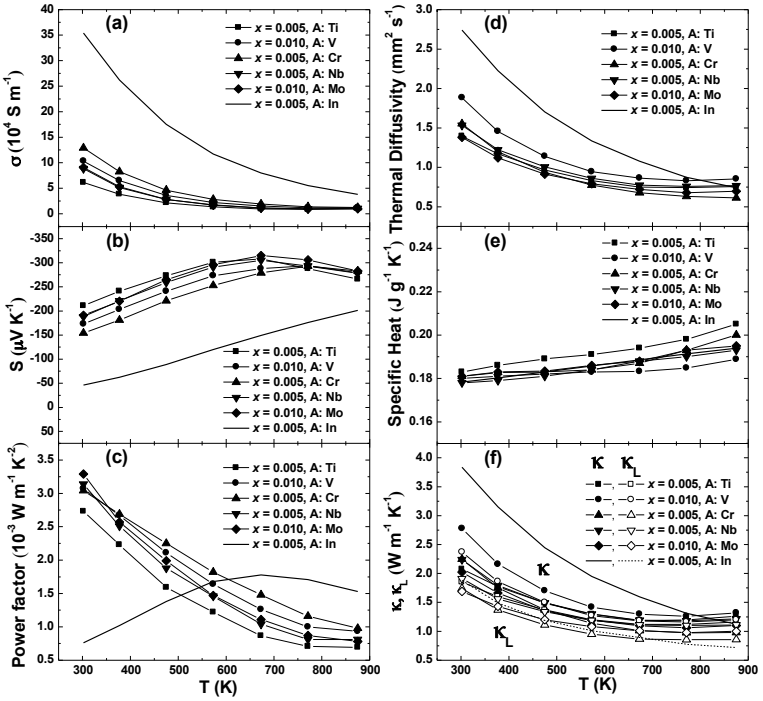

Figure 3.3.4 Temperature dependence of (a) electrical conductivity, (b) Seebeck coefficient, (c) power factor, (d) thermal diffusivity, (e) specific heat, and (f) total thermal conductivity and lattice thermal conductivity for optimized $A_xPb_{1-x}Se$ (A: Ti, V, Cr, Nb, and Mo) (x = 0.005 or 0.01) in comparison with previously reported data on $Pb_{1-x}In_xSe$ (x = 0.005) [18] (solid line).

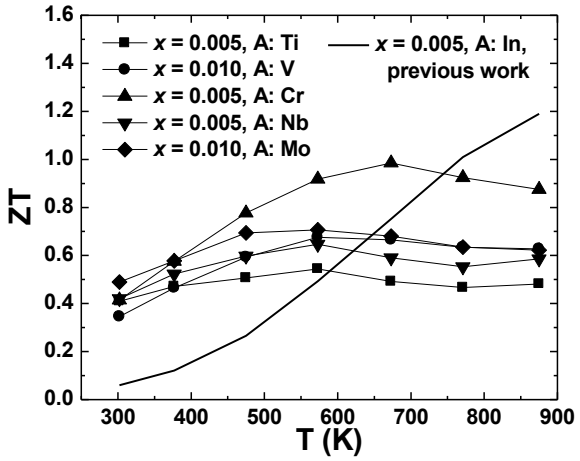

Figure 3.3.5 Temperature dependence of *ZT* for $A_xPb_{1-x}Se$ (A: Ti, V, Cr, Nb, and Mo) (x = 0.005 or 0.01) in comparison with reported data on $Pb_{1-x}In_xSe$ (x = 0.005) [18] (solid line).

What is the reason for these attractive room-temperature power factors? In Figure 3.3.6, we summarized the room temperature Pisarenko relations for $A_xPb_{1-x}Se$ (A: Ti, V, Nb, and Mo) (x = 0.005 or 0.01) and $Cr_xPb_{1-x}Se$ (x = 0.0025, 0.005, 0.0075, and 0.01) (filled triangles) in this work in comparison with all the reported n-type PbSe [18,24-26]. Considering the nonparabolicity of the conduction band of PbSe, a two-band Kane (TBK) model was used to fit the data. The Cl- and Br-doped PbSe are fitted well with effective mass of $m^* = 0.27\ m_e$ (dashed line) [24,25], and B-, Ga- and In-doped PbSe with effective mass of $m^* = 0.5\ m_e$ (solid line) [18]. Due to the resonant scattering, Al-doped PbSe deviates from the fitting line, showing almost constant Seebeck coefficient with increasing carrier concentration [26]. Similar to B-, Ga- and In-doped PbSe, all transition metal Ti-, V-, Cr-, Nb-, and Mo-doped PbSe fell onto the fitting line with effective mass of $m^* = 0.5\ m_e$.

In spite of the speculation for formation of deep resonant levels in Cr-doped PbSe [32], resonant scattering was observed neither in Cr, nor in any of (Ti, V, Nb and Mo) doped PbSe materials. In addition, the room temperature relationships between μ and n for the optimal transition metal-doped PbSe, together with all the reported n-type PbSe are shown in Figure 3.3.7 [18,24-26]. Only Al-doped PbSe deviates largely due to resonant scattering [26]. The higher Seebeck coefficient in the samples is mostly attributed to the lower carrier concentration, which is in the range of $(4\text{-}10)\times10^{18}$ cm^{-3}. To compare our data, we included most of the room temperature properties for optimally n-type doped PbSe by Ti, V, Cr, Nb, and Mo; B, Al, Ga, and In; and Cl in table 3.2.1. The higher room temperature ZT is mainly related to the higher room temperature power factor ($PF = S^2 n\mu e$). Both Seebeck coefficient (S) and Hall mobility (μ) are inversely proportional to Hall carrier concentration (n) (see Figure 3.3.6 and Figure 3.3.7). With relatively low carrier concentration (n), the transition metal-doped PbSe has both higher S and μ, contributing to the higher power factor at room temperature. We usually optimize the Hall carrier concentration to ~10^{19}-10^{20} cm^{-3} for high peak ZT values. However, it seems that the optimal Hall carrier concentration is ~10^{18}-10^{19} cm^{-3} for good ZT values near room temperature. Hence, ideal average ZT value can be obtained by balancing the Hall carrier concentration.

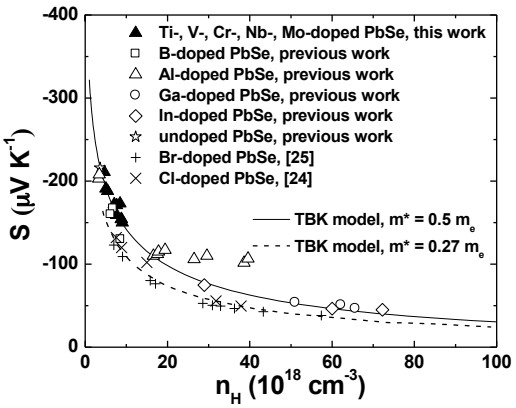

Figure 3.3.6 Room-temperature Pisarenko plots for $A_xPb_{1-x}Se$ (A: Ti, V, Nb, and Mo) (x = 0.005 or 0.01) and $Cr_xPb_{1-x}Se$ (x = 0.0025, 0.005, 0.0075, and 0.01) (filled triangles) in comparison with reported data on B-doped PbSe (open squares), Al-doped PbSe (open triangles), Ga-doped PbSe (open circles), In-doped PbSe (open diamonds) and undoped PbSe (open stars) [18,26], Cl-doped PbSe by Androulakis *et al*., (crosses) [24] and Br-doped PbSe by Wang *et al*., (pluses) [25]. Black curve is based on nonparabolic two-band Kane model (TBK) with the electron effective mass of PbSe m* = 0.5 m_e [18]. Dashed curve is based on nonparabolic TBK with the electron effective mass of PbSe m* = 0.27 m_e [25].

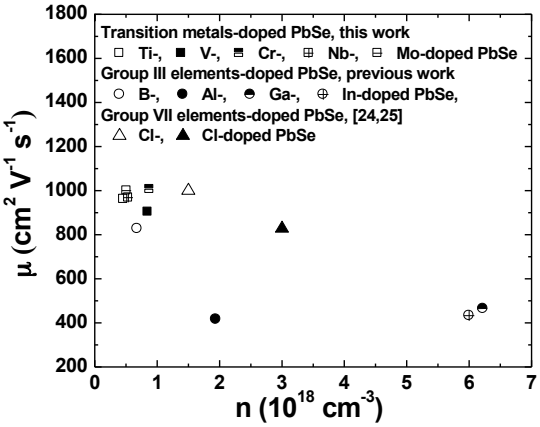

Figure 3.3.7 Room-temperature relationships between μ and n for transition metals-doped PbSe: $Ti_{0.005}Pb_{0.995}Se$, (open squares) $V_{0.01}Pb_{0.99}Se$ (solid squares), $Cr_{0.005}Pb_{0.995}Se$ (half open squares), $Nb_{0.005}Pb_{0.995}Se$ (plus in squares), and $Mo_{0.01}Pb_{0.99}Se$ (minus in squares) in comparison with reported data on PbSe doped with group III elements: $B_{0.02}Pb_{0.98}Se$ (open circles), $Al_{0.01}Pb_{0.99}Se$ (solid circles), $Ga_{0.005}Pb_{0.995}Se$ (half open circles), and $In_{0.005}Pb_{0.995}Se$ (plus in circles) [18,26], and PbSe doped with group VII elements: $PbSe_{0.996}Cl_{0.004}$ (open triangles) [24], and $Pb_{1.002}Se_{0.9982}Br_{0.0018}$ (solid triangles) [25]. The data of Al-doped PbSe (solid circle) deviates largely due to the resonant scattering.

Table 3.3.1 Comparison of room-temperature properties for optimally doped n-type PbSe by Ti, V, Cr, Nb, and Mo; B [18], Al [26], Ga [18], and In1 [8], and Cl [24].

Composition	σ (10^4 S m^{-1})	S (μV K^{-1})	PF (10^{-3} W m^{-1} K^{-2})	n (10^{19} cm^{-3})	μ (cm^2 V^{-1} s^{-1})	κ_{total} (W m^{-1} K^{-1})	κ_L (W m^{-1} K^{-1})	ZT
$Pb_{0.995}Ti_{0.005}Se$	6.13	-211	2.73	0.46	962	2.077.0	1.85	0.41.0
$Pb_{0.99}V_{0.01}Se$	10.3	-173	3.07	0.85	904	2.078.0	2.37	0.35.0
$Pb_{0.995}Cr_{0.005}Se$	12.9	-154	3.04	0.88	1006	2.247	1.74	0.42.0
$Pb_{0.995}Nb_{0.005}Se$	8.84	-188	3.14	0.54	968	2.239	1.91	0.42.0
$Pb_{0.99}Mo_{0.01}Se$	9.05	-191	3.29	0.51	1000	2.025	1.69	0.49.0
$Pb_{0.98}B_{0.02}Se$	8.72	-167	2.42	0.68	827	2.119	1.79	0.34.0
$Pb_{0.99}Al_{0.01}Se$	12.9	-117	1.17	1.94	416	2.280	1.34	0.23.0
$Pb_{0.995}Ga_{0.005}Se$	38.5	-51	1.0	6.22	465	3.759	1.69	0.08.0
$Pb_{0.995}In_{0.005}Se$	35.4	-46.4	0.76	6	433	3.838	1.86	0.06.0
$PbSe_{0.996}Cl_{0.004}$	23	-105	2.53	1.5	1000	2.67	1.9	0.27.0

The discretization method of Mahan was used to estimate the device efficiency of the TE legs made by some of the n-type PbSe (solid lines) and n-type $Bi_2Te_{2.7}Se_{0.3}$ (dashed line) with thecold-side temperature at 300 K [37-40]. We assumed that, heat flow in the legs to be one-dimensional, neglecting losses from the sidewalls of the legs [13]. The results are shown in Figure 3.3.8. Even though, higher peak *ZT*s are achieved in other n-type PbSe materials, (1.3 at 850 K for Al doped PbSe [26], 1.2 at 850 K for Br-doped PbSe [25], and 1.2 at 873 K for Ga-, In-doped PbSe [18]) Cr-doped PbSe has the highest efficiency for a wide range of hot-side temperatures (350-873 K). At the lower temperature range, when the hot-side temperature is between 350 K and 523 K, the device efficiency of Cr-

doped PbSe is only slightly lower than that of the temperature-limited n-type $Bi_2Te_{2.7}Se_{0.3}$ [36]. At high hot-side temperatures, Al-doped PbSe only rivals the efficiency of Cr-doped PbSe, but it has much lower efficiency at lower hot-side temperatures. These results emphasize the benefits of a flatter *ZT* curve. In a flatter *ZT* curve, not only is the efficiency higher at high temperatures, but also it is higher at a wide range of hot-side temperatures.

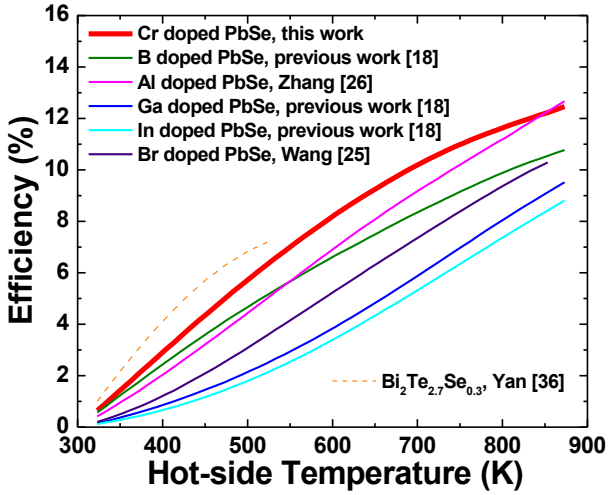

Figure 3.3.8 Temperature dependence of device efficiency for 0.5 atm. % Cr doped PbSe (this work, red) in comparison with the optimized B-doped PbSe (green) [18] Al-doped PbSe (pink) [26], Ga- doped PbSe (blue) [18], In-doped PbSe (light blue) [18], Br-doped PbSe (purple) [25], and $Bi_2Te_{2.7}Se_{0.3}$ (dashed orange) [36] withcold-side temperature 300 K.

Instead of the comparison of the peak *ZT*s, we present average *ZT*s (integrating of the area below the *ZT* curves) from 300 to 873 K (Figure 3.3.9a, left panel) and device *ZT*s (obtained from the theoretically calculated efficiency) operated between 300 K and 873 K (Figure 3.3.9b, left panel) for some of the n-type PbSe materials. We also present the average *ZT*s between 300 K and 523 K (Figure 3.3.9a, right panel) and device *ZT*s operated between 300 K and 523 K (Figure 3.3.9b, right

panel) for some n-type PbSe materials compared with n-type $Bi_2Te_{2.7}Se_{0.3}$. Cr-doped PbSe has higher average *ZT* and device *ZT* compared to other n-type PbSe materials, especially when working between 300 K and 523 K, though not as good as $Bi_2T_{2.7}Se_{0.3}$. Furthermore, the device *ZT* of Cr-doped PbSe (between 300 K and 873 K) is even higher than that of the reported n-type PbTe:La/Ag_2Te (between 300 K and 775 K) which has a peak *ZT* of ~1.6 at 775 K [21]. Many of the best p-type PbTe materials, such as PbTe:Na (between 300 K and 750 K) with peak *ZT* ~1.4 at about 750 K [20], PbTe:Tl (between 300 K and 775 K) with peak *ZT* ~1.4 at about 775 K [1], PbTe:Na/SrTe (between 300 K and 775 K) with peak *ZT* ~1.5 at about 775 K [41], and $PbTe_{0.85}Se_{0.15}$:Na (between 300 K and 800 K) with peak *ZT* ~1.8 at about 800 K [3], could benefit from a flatter *ZT* curve. Considering the cost of Se compared to Te, and the higher device efficiency and wider working temperature range of PbSe than PbTe, PbSe has the potential to replace PbTe for thermoelectric applications. However, still more work is expected in increasing the device efficiency of p-type PbSe.

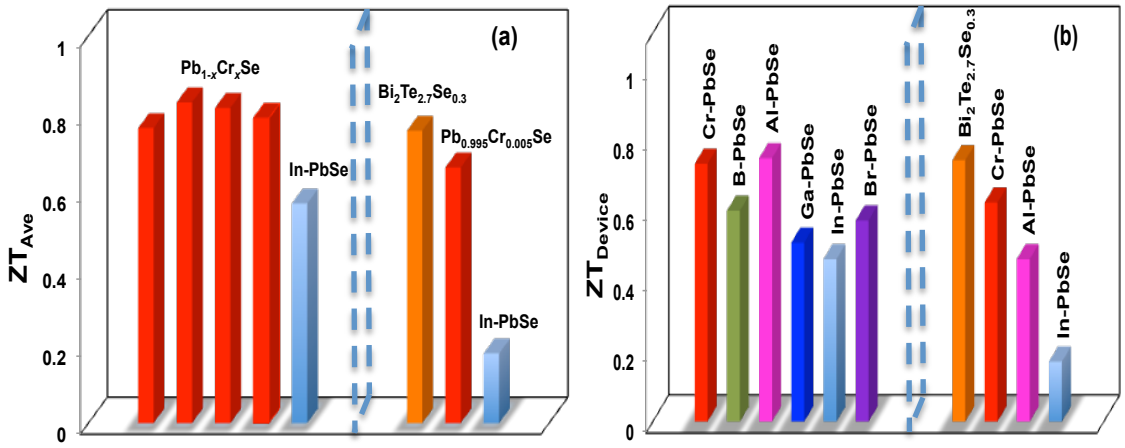

Figure 3.3.9 (a) Comparison of average *ZT* from 300 K to 873 K between $Pb_{1-x}Cr_xSe$ (x = 0.0025, 0.005, 0.0075, and 0.01) (this work, red) and optimized In-doped PbSe (light blue) (left panel) [18]. Comparison of average *ZT* from 300 K to 523 K for $Bi_2Te_{2.7}Se_{0.3}$ (orange) [36], 0.5 atm. % Cr doped PbSe (this work, red) and optimized In-doped PbSe (light blue) (right panel) [18]. (b) Comparison of device *ZT* operated between 300 K and 873 K for 0.5 atm. % Cr-doped PbSe (this work, red) and optimized B- (green), [18] Al- (pink), [26] Ga- (blue) [18], In- (light blue) [18], and Br- (purple) doped PbSe (left panel) [25]. Comparison of device *ZT* operated between 300 K and 523 K for $Bi_2Te_{2.7}Se_{0.3}$ (orange) [36], 0.5 atm. % Cr-doped PbSe (this work, red) and optimized Al- (pink) [26], In-doped PbSe (light blue) [18] (right panel).

3.4. Conclusion

Transition metals (Ti, V, Cr, Nb, and Mo) can enhance the lower-temperature (below 600 K) TE properties of n-type PbSe. Specifically, Cr doping in PbSe increases the room temperature *ZT* to ~0.4 and the peak *ZT* to ~1.0 between 573 K and 673 K, hence increasing the average *ZT* and efficiency of n-type PbSe over a wide temperature range (300 K to 873 K). This boost is not attributed to a resonant states effect. By further tuning the carrier concentration, even better properties can be expected. Cr-doped n-type PbSe is believed to be promising for power generation applications.

References

[1] J. P. Heremans, V. Jovovic, E. S. Toberer, A. Saramat, K. Kurosaki, A. Charoenphakdee, S. Yamanaka and G. J. Snyder, *Science*, **321**, 554, (2008).
[2] A. D. LaLonde, Y. Z. Pei and G. J. Snyder, *Energy Environ. Sci*, **4**, 2090, (2011).
[3] Y. Z. Pei, X. Y. Shi, A. LaLonde, H. Wang, L. D. Chen and G. J. Snyder, *Nature*, **473,** 66, (2011).
[4] Q. Zhang, F. Cao, W. S. Liu, K. Lukas, B. Yu, S. Chen, C. Opeil, G. Chen and Z. F. Ren, *J. Am. Chem. Soc.*, **134**, 10031, (2012).
[5] Q. Y. Zhang, H. Z. Wang, Q. Zhang, W. S. Liu, B. Yu, H. Wang, D. Z. Wang, G. Ni, G. Chen and Z. F. Ren, *Nano Lett.* **12,** 2324, (2012).
[6] R. J. Korkosz, *et al., J. Am. Chem. Soc.* **136**, 3225, (2014).
[7] D. M. Rowe, CRC Handbook of Thermoelectrics, Macro to Nano; CRC Press, Taylor & Francis Group, Boca Raton, (2006).
[8] B. Poudel, *et al., Science*, **320**, 634, (2008).
[9] D. Kraemer, *et al., Nature Materials*, **10**, 532, **(**2011).
[10] L. P. Hu, T. J. Zhu, Y. G. Wang, H. H. Xie, Z. J. Xu and X. B. Zhao, *NPG Asia Mater.*, **6**, e88, (2014).
[11] F. Cao, K. McEnaney, G. Chen and Z. F. Ren, *Energy Environ. Sci.*, **7**, 1615, (2014).
[12] G. H. Zeng, *et al., Appl. Phys. Lett.*, 95, 083503, (2009).
[13] W. S. Liu, K. Lukas, K. McEnaney, S. Lee, Q. Zhang, C. Opeil, G. Chen and Z. F. Ren, *Energy Environ. Sci.*, **6**, 552, (2013).
[14] C. Hadjistassou, E. Kyriakides and J. Georgiou, *Energ. Convers. Manage.*, **66,** 165, (2013).
[15] S. Yoon, *et al.,* J. *Elec. Mater.,* **43**, 414, (2014).
[16] P. H. Ngan, *et al., Phys. Status Solidi A*, **211**, 9, (2014).
[17] H. Wang, Y. Pei, A. D. LaLonde and G. J. Snyder, *Adv. Mater.*, **23**, 1366 (2011).
[18] Q. Zhang, *et al., J. Am. Chem. Soc.,* **134**, 17731, (2012).
[19] Y. Z. Pei, *et al., Energy Environ. Sci.*, **4**, 3640, (2011).
[20] Y. Pei, A. LaLonde, S. Iwanaga and G. J. Snyder, *Energy Environ. Sci.*, **4**, 2085, (2011).
[21] Y. Pei, J. Lensch-Falk, E. S. Toberer, D. L. Medlin and G. J. Snyder, *Adv. Funct. Mater.*, **21**, 241, (2011).
[22] Y. Z. Pei, *et al., Adv. Mater.,* **23**, 5674, (2011).
[23] G. T. Alekseeva, *et al., Semicond*., **30**, 1125, (1996).
[24] J. Androulakis, *et al., Phys. Rev.* B, **84**, 155207, (2012).
[25] H. Wang, Y. Z. Pei, A. D. LaLonde and G. J. Snyder, *Proc. Natl. Acad. Sci. USA.*, **109**, 9705, (2012).
[26] Q. Y. Zhang, *et al., Energy Environ. Sci.*, **5**, 5246, (2012).
[27] M. I. Baleva and L. D. Borissova, *J. Phys. C: Solid State Phys.*, **16**, L907, (1983).
[28] B. Paul and P. Banerji, *J. Appl. Phys.*, **109**, 103710, (2011).

[29] B. Paul, P. K. Rawat and P. Banerji, *Appl. Phys. Lett.*, **98**, 262101, (2011).
[30] M. D. Nielsen, *et al., Phys. Rev.* B, **85**, 045210, (2012).
[31] E. P. Skipetrov, *et al., Semiconductors*, **47**, 729, (2013).
[32] T. Story, *et al., Acta Phys. Polonica,* A, **87**, 229, (1995).
[33] F. F. Sizov, *et al., Sov. Phys. Semicond.*, **14**, 1063, (1980).
[34] V. V. Teterkin, *et al., Sov. Phys. Semicond.*, **17**, 489, (1983).
[35] J. D. König, *et al., Phys. Rev.* B, **84**, 205126, (2011).
[36] X. Yan, *et al., Nano Lett.*, **10**, 3373, (2010).
[37] G. D. Mahan, *J. Appl. Phys.*, **70**, 4551, (1991).
[38] J. Snyder and T. S. Ursell, *Phys. Rev. Lett.*, **91**, 148021, (2003).
[39] H. J. Goldsmid, *Introduction to thermoelectricity*, Springer-Verlag, Berlin Heidelberg, (2010).
[40] A. Muto, J. Yang, B. Poudel, Z. F. Ren and G. Chen, *Adv. Energy Mater.*, **3**, 245, (2013).
[41] K. Biswas, *et al., Nat. Chem.*, **3**, 160, (2011).

CHAPTER 4: THERMOELECTRIC PROPERTIES OF CR DOPED N-TYPE $PbTe_{1-y}Se_y$

4.1. Introduction

As discussed in preceding chapters, improving the performance of thermoelectric materials requires tuning of the coupled thermal and electrical transport properties [1-4]. Despite the difficulty of tuning these parameters independently, significant efforts have been put into decoupling them using various techniques [5,6]. These include but are not limited to nanostructuring [7-8], which gives the opportunity to independently tune these parameters and reduces the thermal conductivity by scattering a broad spectrum of phonons [9-10], band structure modifications, by alloying [11-13] or doping to create impurity levels that resonate with the host band [14,15] or both [16,17], lead to significant achievements in obtaining higher *ZT* values. In chapter three, we have seen that Cr doping improved the thermoelectric performance of PbSe near room temperature. Since PbSe and PbTe are isostructural compounds, we also investigated the effect of Cr doping on the thermoelectric performance PbTe near room temperature.

Lead telluride (PbTe), with its intrinsically low thermal conductivity [18,19] is one of the most-studied thermoelectric materials for medium temperature applications [20]. The thermoelectric performance of PbTe has been enhanced by alloying with its isostructural sister compound PbSe. The partial substitution of Te by Se leads to disorder via atomic mass fluctuations, distortion in the crystal lattice and formation of defect states, which can effectively scatter phonons more than charge carriers (electrons or holes) to reduce thermal conductivity [9,10,12]. Significant progresses have been reported in improving

the *ZT* of PbTe by simultaneous alloying, doping, and band engineering. Tl acts as a resonant dopant in PbTe to enhance the *ZT* to ~1.5 by modifying the band structure [14]. By potassium doping, a peak *ZT* value of ~1.7 at 873 K was achieved in $K_{0.02}Pb_{0.98}Te_{0.15}Se_{0.85}$ [20]. A *ZT* of ~1.8 was obtained in p-type $Na_{0.02}Pb_{0.98}Te_{0.85}Se_{0.15}$ by band convergence [11]. Even though, the peak *ZT*s of these materials at high temperatures is high, their average *ZT*s are low. This is due to their lower *ZT* values below 400 K [22-23] that significantly reduce the efficiency of the materials. Cr was reported as a resonant donor in PbTe, PbSe, and $PbTe_{1-y}Se_y$ systems at low temperatures [24]. The room-temperature Seebeck coefficient and power factor in PbTe [25] and PbSe [26] can be increased by Cr doping. However, the improvement was proved to not be due to resonant scattering. One study shows the formation of a Cr resonant state in PbTe, with an energy 100 meV above the conduction band bottom of PbTe at 0 K, but the state moves into the band gap when the temperature increases to room temperature and hence doesn't contribute to a power factor enhancement at or above room temperature [27]. Another study also found that Cr impurity states within the conduction band of PbTe [25]. However, the band distortion that comes from such a resonance of the Cr impurity level is not broadened well enough to properly align the Fermi level with the enhanced density of states and hence doesn't contribute to the enhancement of Seebeck coefficient. In this chapter, we will address our systematic study of the enhancement of both the *ZT* near room temperature and the average *ZT* of $PbTe_{1-y}Se_y$ (y = 0, 0.25, 0.50, 0.75, 0.85, and 1) across a wide range of temperature by Cr doping. The reduction in thermal conductivity due to phonon scattering by the introduced point defects from the alloying,

together with the optimized electronic properties by Cr doping, contributed to the enhancement of the room temperature *ZT* to ~0.6 for Te-rich $Cr_{0.015}Pb_{0.985}Te_{0.75}Se_{0.25}$ and a peak *ZT* of ~1 at about 573 K to 673 K for Se-rich $Cr_{0.01}Pb_{0.99}Te_{0.25}Se_{0.75}$ with a room temperature *ZT* of ~0.5. The calculated single leg efficiency of $Cr_{0.015}Pb_{0.985}Te_{0.75}Se_{0.25}$ and $Cr_{0.01}Pb_{0.99}Te_{0.25}Se_{0.75}$ is ~ 10 % and ~12 %, respectively, with acold-side temperature of 300 K and hot-side temperature of 773 K.

4.2. Experimental Methods

Ingots of samples of $Cr_xPb_{1-x}Te_{1-y}Se_y$ with x = 0.005, 0.01, 0.015, and 0.02, and y = 0, 0.25, 0.50, 0.75, 0.85, and 1 were prepared in a carbon coated quartz tube from high purity elements (Cr pieces, 99.99%; Pb granules, 99.99%; Te chunks 99.999%; Se granules, 99.99%) according to their stoichiometric weights. The tubes were evacuated to ~3×10^{-4} Pa and sealed, then slowly heated to 1000-1100 ^{o}C at a rate of 200 ^{o}C/hour and then held at that temperature for 6 hours, then slowly cooled at the same rate to 650 ^{o}C and kept there for 50 hours, and then finally cooled to room temperature. The ingots obtained from this procedure were cleaned and hand milled in a glove box with an argon environment. The hand-milled powder was then loaded into a half inch graphite die, hot pressed at 600 ^{o}C for 2 minutes, air cooled, polished, cleaned, and cut to a desired shape for characterization. The microstructures were investigated by a scanning electron microscope (SEM, LEO 1525). Seebeck coefficient (*S*) and electrical conductivity (σ) measurements were done using a static direct current method and a four-point direct current switching method, respectively, on a commercial (ULVAC ZEM-3) system. The room-temperature Hall coefficient (R_H) was measured using a Quantum Design Physical

Properties Measurement System. The Hall carrier concentration n_H and Hall mobility μ_H were calculated from the Hall coefficient R_H by $n_H = (eR_H)^{-1}$ and $\mu_H = \sigma R_H$, respectively. The thermal diffusivity (α) was measured by a laser flash analyzer (Netzsch LFA 457) and the specific heat (C_p) was measured on a differential scanning calorimetry thermal analyzer (Netzsch DSC 404 C) whereas the volumetric density (D) was measured by the Archimedes method. The thermal conductivity was calculated by $\kappa = D\alpha C_p$. Our measurements are accurate to within 12 % for the *ZT* and 10 % for the power factor, coming from a 3 % error in electrical conductivity, a 5 % error in Seebeck coefficient, and a 7 % error in thermal conductivity. Error bars were not used in the Figures to increase the readability of the curves.

4.3. Thermoelectric Transport Properties of Cr doped $PbTe_{1-y}Se_y$

The lower thermal conductivity due to large Grüneisen parameter values and nanocomposite microstructures [26,28] with the high power factor by Cr doping has improved the average *ZT* of n-type PbSe over a wide temperature range (300 K-873 K) [26]. When Cr is doped into PbTe, the room temperature power factor increased dramatically compared with the other n-type PbTe alloys [25]. The best power factor at room temperature is ~36.50 μW cm^{-1} K^{-2} in $Cr_{0.025}Pb_{0.975}Te$, which is approximately a 22 % increase compared to Cr-doped PbSe. This result is close to the values reported by B. Paul *et al.,* [25] on Cr-doped PbTe. However, the thermal conductivity increased to ~2.6 W m^{-1} K^{-1} at room temperature and ~1.3 W m^{-1} K^{-1} at 773 K, higher than that of Cr-doped PbSe (~2.2 W m^{-1} K^{-1} at room temperature and ~1.0 W m^{-1} K^{-1} at 773 K). Figure 4.3.1

shows the temperature dependence of the thermoelectric properties of Cr-doped PbTe at various Cr concentrations.

The calculated *ZT* is ~0.45 at room temperature and ~0.8 at 600 K to 773 K. The relatively lower thermal conductivity in PbSe and higher room temperature power factor from Cr doped PbTe motivated us to further optimize the alloy system by achieving the best power factor and lower thermal conductivity to get a higher room temperature *ZT* and average *ZT*. We used the highest C_p of $Cr_{0.03}Pb_{0.97}Te$ for all samples $Cr_xPb_{1-x}Te$ with various Cr concentrations (Figure 4.3.1e) so as to void underestimation of thermal conductivity. For other $Cr_xPb_{1-x}Te_{1-y}Se_y$ samples, the selected measured C_ps are shown in Figure 4.3.2. The lattice thermal conductivity is obtained by subtracting the electronic thermal conductivity ($\kappa_e = L\sigma T$, where L is the Lorenz number calculated using a two-band Kane model) from the total thermal conductivity.

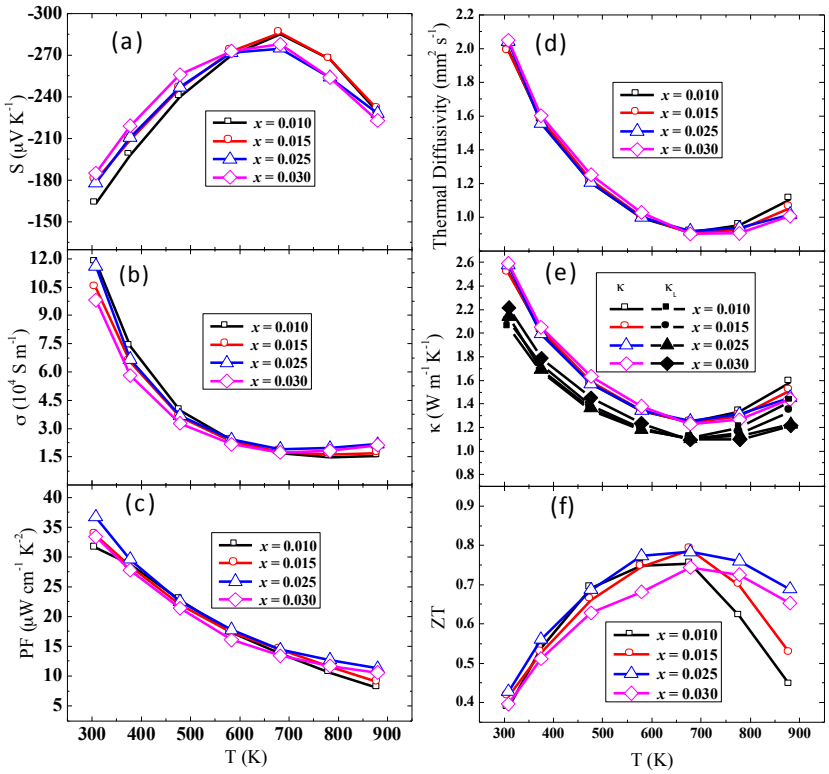

Figure 4.3.1 Temperature-dependent thermoelectric properties of $Cr_xPb_{1-x}Te$ at various dopant concentrations (x = 0.01, 0.015, 0.025, and 0.03). (a) Seebeck coefficient, (b) electrical conductivity, (c) power factor, (d) thermal diffusivity, (e) total thermal conductivity and lattice thermal conductivity, and (f) *ZT*.

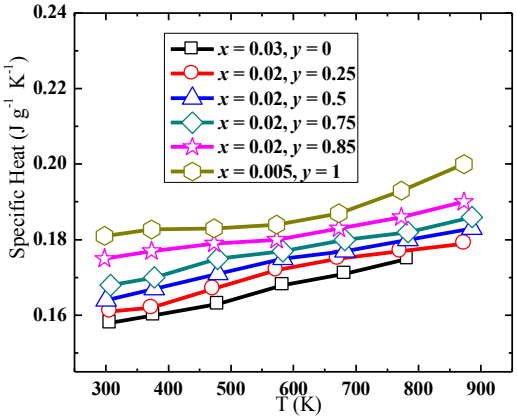

Figure 4.3.2 Temperature-dependent specific heat of $Cr_xPb_{1-x}Te_{1-y}Se_y$ (x = 0.005, 0.02, and 0.03, y = 0, 0.25, 0.5, 0.75, 0.85, and 1).

Samples with compositions $Cr_xPb_{1-x}Te_{0.75}Se_{0.25}$ and $Cr_xPb_{1-x}Te_{0.25}Se_{0.75}$ were prepared and the temperature dependences of the thermoelectric properties are shown in Figure 4.3.3 and Figure 4.3.4 respectively. For $Cr_xPb_{1-x}Te_{0.75}Se_{0.25}$, the Seebeck coefficient shows a slight increase and a strong bipolar effect at above 600 K when the Cr doping level increases from 1 atm. % to 2 atm. %. The electrical conductivity first increased until the Cr doping reaches a critical value of 1.5 atm. % and then decreased when the doping concentration of Cr increased to 2 atm. %. This is due to the reduction in the mobility of electrons with increasing defect density as the dopant contributes to disorder at higher concentrations. It shows a relatively higher electrical conductivity at 1.5 atm. % Cr doping level, which is attributed to the higher carrier mobility (~1120 $cm^2\ V^{-1}\ s^{-1}$) as confirmed by room-temperature Hall measurement. This electrical conductivity in combination with the high Seebeck coefficient, yields a higher room temperature power factor of ~24 $\mu W\ cm^{-1}\ K^{-2}$ (Figure 4.3.3c). This room temperature mobility (1120 $cm^2\ V^{-1}\ s^{-1}$) and power factor (~24 $\mu W\ cm^{-1}\ K^{-2}$) is respectively lower by ~ 20 % and 37 % compared to the mobility (~1404 $cm^2\ V^{-1}\ s^{-1}$) and power factor (~38 $\mu W\ cm^{-1}\ K^{-2}$) of Cr doped PbTe studied by B. Paul *et al.,* [25]. However, in spite of the 37 % power factor reduction, the *ZT* value of $Cr_{0.015}Pb_{0.985}Te_{0.75}Se_{0.25}$ is ~ 66 % higher than that of Cr doped PbTe [25] thanks to the highly suppressed thermal conductivity. The thermal conductivity is decreased due to the introduced atomic scale defects by alloying via atomic mass disorder, plenty of grain boundaries and multiple defects such as vacancies and dislocations present in the samples as we can see from the HRTEM images in Figure 4.3.6 (b).

The atomic scale defects (atomic mass disorder and vacancies) strongly scatter phonons of high frequency and short mean free path that contribute to most of the thermal conductivity in $PbTe_{1-y}Se_y$ compounds [29]. On the other hand, low frequency and long mean free path phonons are scattered by the mesoscale defects (grain boundaries and dislocations). All the $Cr_xPb_{1-x}Te_{1-y}Se_y$ samples consist of both big grains with diameters of several tens of microns and small grains of size ~50 nm which scatter a broad spectrum of phonons with mean free path greater than 50 nm. However, in lead-telluride and lead-selenide alloys, it has been proven that only phonons of mean free path less than 10 nm contribute to most of the thermal conductivity and a grain size of less than 10 nm needed to be achieved to bring a significant reduction of the thermal conductivity by nanostructuring [29]. The lowest thermal conductivity is ~0.9 W m^{-1} K^{-1} at 573 K. However, there is a small influence on the room temperature value with Cr doping. It decreased and then increased when the Cr doping level varied from 1 atm. % to 2 atm. % showing a minimum value of ~1.2 W m^{-1} K^{-1} at a doping concentration of 1.5 atm. %, which lead to a record *ZT* of ~0.6 in lead chalcogenide systems at room temperature. This *ZT* value is not too much lower than the *ZT* of the well-known state-of-the-art n-type room temperature material $Bi_2Te_{2.7}Se_{0.3}$ [30]. The increase of the thermal conductivity at elevated temperatures is clearly due to the excitation of minority carriers.

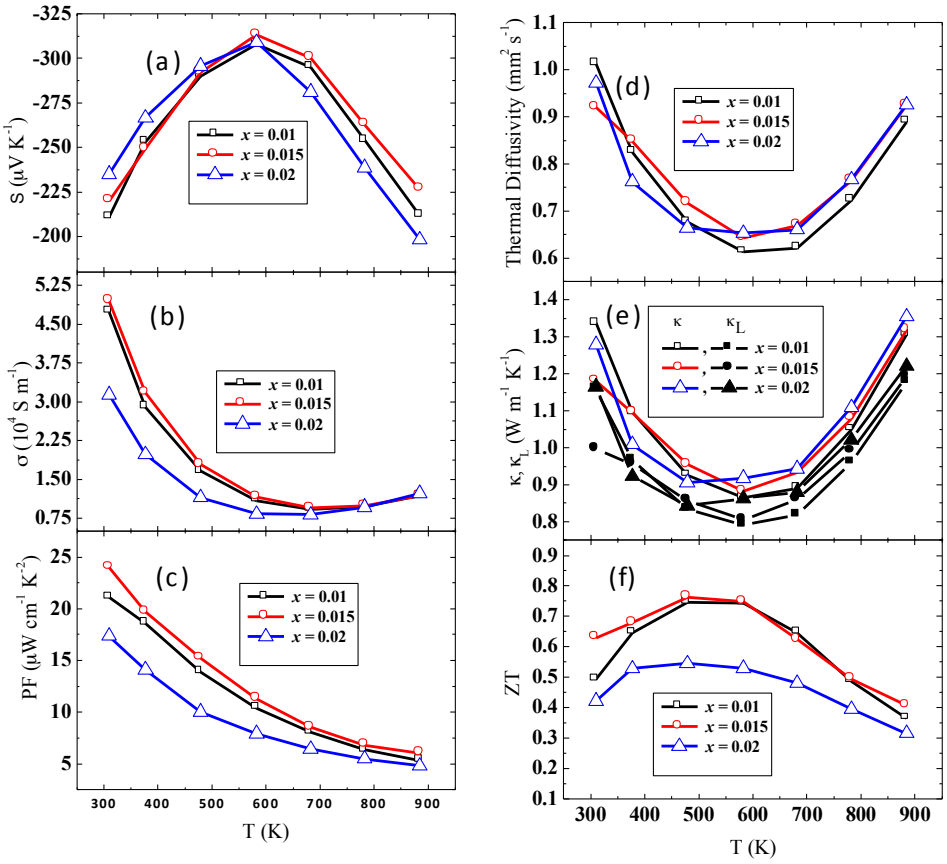

Figure 4.3.3 Temperature-dependent thermoelectric properties of $Cr_xPb_{1-x}Te_{0.75}Se_{0.25}$ (x = 0.01, 0.015, and 0.02). (a) Seebeck coefficient, (b) electrical conductivity, (c) power factor, (d) thermal diffusivity, (e) total thermal conductivity and lattice thermal conductivity, and (f) *ZT*.

For $Cr_xPb_{1-x}Te_{0.25}Se_{0.75}$, as shown in Figure 4.3.4, the Seebeck coefficient shows a similar trend as the Te-rich (Figure 4.3.3) system with increasing Cr concentration. Nevertheless, this composition is less susceptible to bipolar conduction and the bipolar temperature is higher than that of the Te-rich composition. This is due to the suppression of minority carriers by the band gap increase in the Se-rich composition with increasing temperature consistent with previous studies [31]. The electrical conductivity also follows a similar trend as the Te-rich composition in

such a way that it increased when the Cr concentration increased to a critical value of 1.5 atm. % then decreased when it exceeds this critical level. The lowest room-temperature thermal conductivity is ~1.25 and ~0.8 at about 673 K in $Cr_{0.01}Pb_{0.99}Te_{0.25}Se_{0.75}$, that gave rise to a room temperature *ZT* of ~0.5 and peak *ZT* of ~1 from ~ 573 K to 673 K.

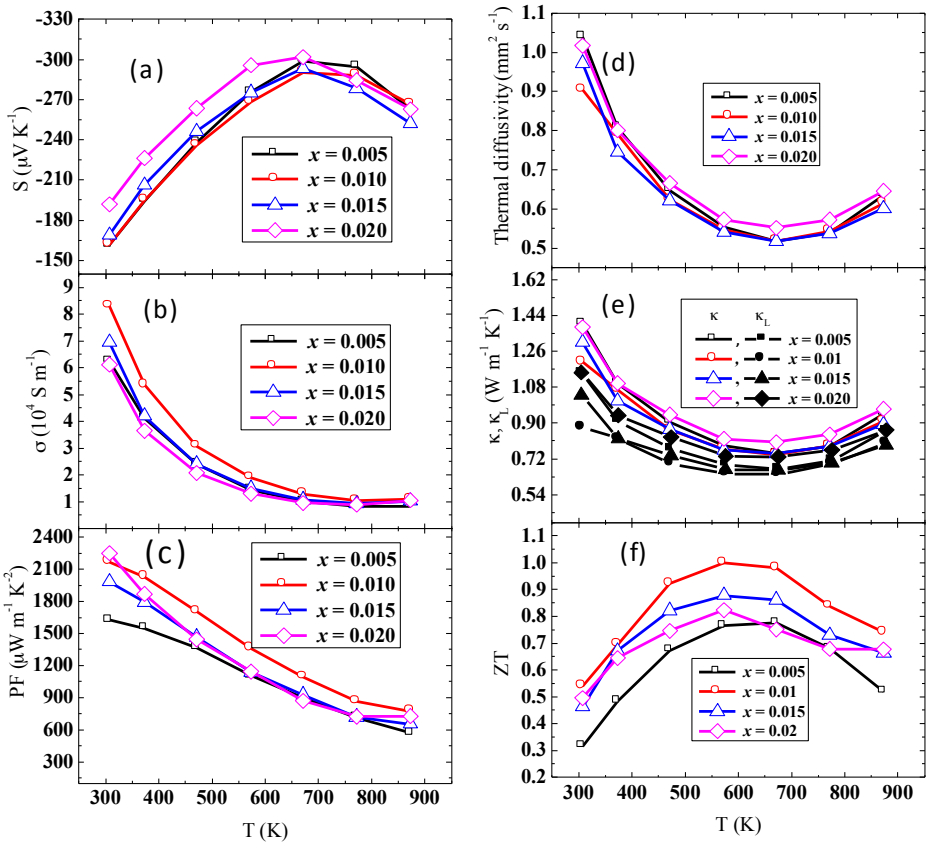

Figure 4.3.4 Temperature-dependent thermoelectric properties of $Cr_xPb_{1-x}Te_{0.25}Se_{0.75}$ (x = 0.005, 0.01, 0.015, and 0.02). (a) Seebeck coefficient, (b) electrical conductivity, (c) power factor, (d) thermal diffusivity, (e) total thermal conductivity and lattice thermal conductivity, and (f) *ZT*.

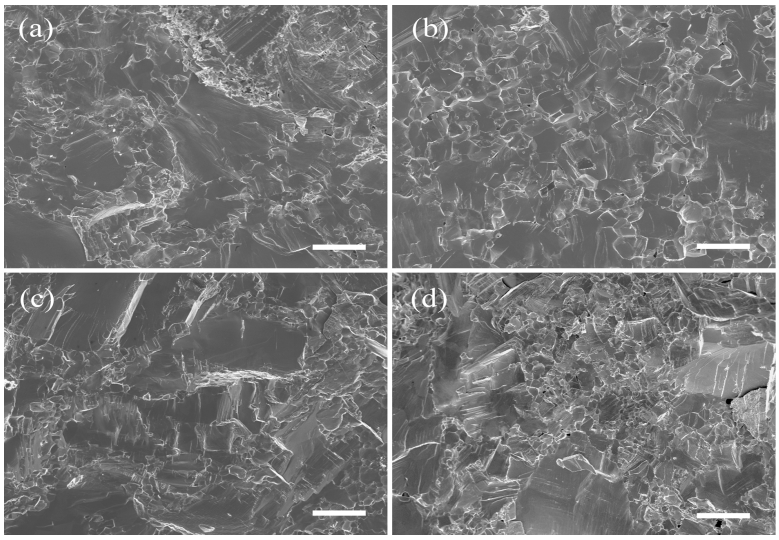

Figure 4.3.5 SEM images of (a) $Cr_{0.025}Pb_{0.975}Te$, (b) Te-rich $Cr_{0.015}Pb_{0.985}Te_{0.75}Se_{0.25}$, (c) Se-rich $Cr_{0.01}Pb_{0.99}Te_{0.25}Se_{0.75}$, and (d) $Cr_{0.005}Pb_{0.995}Se$. The scale bar is 10 μm.

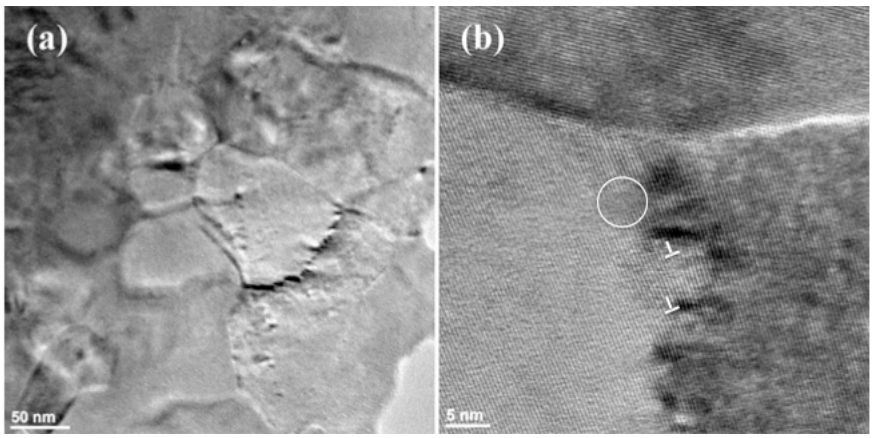

Figure 4.3.6 Low-magnification TEM image (a), and HRTEM image (b) showing grain boundaries, point defects marked by circles, and thread dislocations marked by (_|_).

We then prepared different samples with different Se concentrations to check the alloying effect. Figure 4.3.7 shows the temperature dependence of (a) the Seebeck coefficient, (b) the electrical conductivity, (c) the power factor, (d) the thermal diffusivity, (e) the total thermal conductivity and the lattice thermal conductivity, and (f) the *ZT* with a fixed Cr

concentration of 1 atm. % and different Se concentrations of y = 0.25, 0.5, 0.75, 0.85. The electrical conductivity of all the samples decreased with increasing temperature, consistent with the attributes of degenerate semiconductors. At fixed concentration of 1 atm. % Cr doping, the room-temperature Seebeck coefficient decreased from -211 μV K^{-1} to -157 μV K^{-1} with increasing Se concentration. The Seebeck coefficient of all the samples decreased at higher temperatures showing a bipolar transport nature and it was found that the temperature at which the bipolar effect becomes important for Te-rich samples is lower than that of Se-rich samples. The electrical conductivity increased when the Se concentration increased to 75 atm. % and then decreased above this concentration showing a higher value at an optimum Se concentration of 75 atm. %. The high electrical conductivity manifested by the Se-rich sample $Cr_{0.01}Pb_{0.99}Te_{0.25}Se_{0.75}$ resulted in a higher power factor across the whole temperature range. This high electrical conductivity is attributed to the relatively higher carrier concentration (~8.12×10^{18} cm^{-3}) as evidenced by the room temperature Hall measurement. The thermal conductivity is heavily decreased compared to Cr doped PbTe and PbSe samples due to phonon scattering by the point defects resulting from alloying. We see a minimum thermal conductivity of ~0.8 W m^{-1} K^{-1} at 573 K in $Cr_{0.01}Pb_{0.99}Te_{0.5}Se_{0.5}$ with equal amount of Te and Se. This is approximately a 72 % decrease compared to PbTe for the same Cr doping level of 1 atm. %. This reduction is related to the maximum distortion of the crystal lattice due to the maximum entropic atomic mass fluctuation as confirmed by theoretical calculations and experimental studies [21,29].

The increase in thermal conductivity at higher temperatures is due to the contribution of heat transport by minority carriers (holes). The highest *ZT* is ~1 at approximately from 573 K to 673 K in Se-rich $Cr_{0.01}Pb_{0.99}Te_{0.25}Se_{0.75}$.

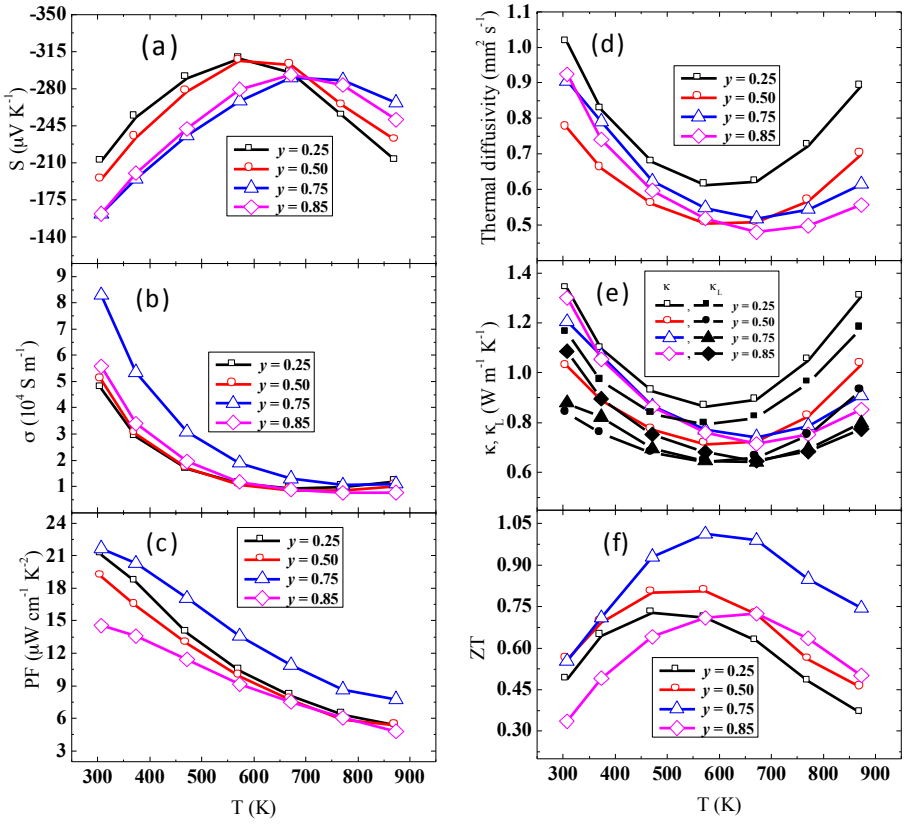

Figure 4.3.7 Temperature-dependent thermoelectric properties of $Cr_{0.01}Pb_{0.99}Te_{1-y}Se_y$ (y = 0.25, 0.5, 0.75, 0.85) with fixed Cr concentration of 1 atm. %. (a) Seebeck coefficient, (b) electrical conductivity, (c) power factor, (d) thermal diffusivity, (e) total thermal conductivity and lattice thermal conductivity, and (f) *ZT*.

At a Cr-doping concentration of 1.5 atm. %, as shown in Figure 4.3.8, the Seebeck coefficient follows a similar trend as in 1 atm. % Cr doping (Figure 4.3.7) with increasing Se concentration. A peak room-temperature Seebeck coefficient of -220 μV K^{-1} was obtained in Te-rich $Cr_{0.015}Pb_{0.985}Te_{0.75}Se_{0.25}$.

The electrical conductivity increases when the Se concentration is higher than 50 atm. %. The minimum electrical conductivity is observed at equal amount of Te and Se because of the reduction in carrier mobility due to the maximum defect density and lower electrical conductivity. As shown in Figure 4.3.8, Se-rich samples show higher electrical conductivity but the power factor is not enhanced that much due to the lower Seebeck coefficient. A highest room-temperature power factor of ~24 μW cm^{-1} K^{-2} is shown by the Te-rich $Cr_{0.015}Pb_{0.985}Te_{0.75}Se_{0.25}$, which is due to the high value of the Seebeck coefficient and carrier mobility. The thermal conductivity is highly reduced due to the alloying effect. A room-temperature thermal conductivity of ~1.2 W m^{-1} K^{-1} was obtained for the Te-rich sample $Cr_{0.015}Pb_{0.985}Te_{0.75}Se_{0.25}$ and it is a 52 % decrease compared to PbTe for the same 1.5 atm. % Cr doping level. Thus, by simultaneously reducing the thermal conductivity and enhancing the power factor, a record *ZT* of ~0.63 is achieved in Te-rich $Cr_{0.015}Pb_{0.985}Te_{0.75}Se_{0.25}$ at room temperature.

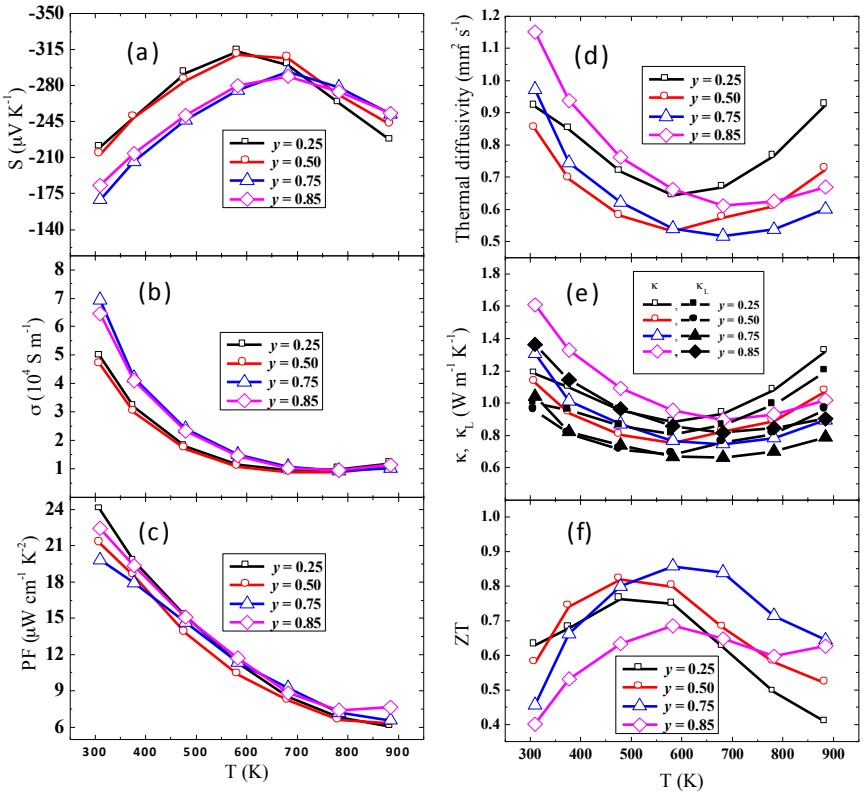

Figure 4.3.8 Temperature-dependent thermoelectric properties of $Cr_{0.015}Pb_{0.99}Te_{1-y}Se_y$ (y = 0.25, 0.5, 0.75, 0.85) with fixed Cr concentration of 1.5 atm. %. (a) Seebeck coefficient, (b) electrical conductivity, (c) power factor, (d) thermal diffusivity, (e) total thermal conductivity and lattice thermal conductivity, and (f) *ZT*.

The room-temperature Pisarenko relation between the Seebeck coefficient and the Hall carrier concentration of $Cr_xPb_{1-x}Te_{1-y}Se_y$ is plotted in Figure 4.3.9. All the Hall carrier concentrations are lower than 1.0×10^{19} cm^{-3} and the absolute Seebeck coefficients are higher than 150 μV K^{-1} which is more than twice the room temperature Seebeck coefficients of other state-of-the-art p and n-type lead chalcogenide alloys such as;

$Na_{0.02}Pb_{0.98}Te_{0.75}Se_{0.25}$ [11], $K_{0.02}Pb_{0.98}Te_{0.15}Se_{0.85}$ [20], $In_{0.001}Pb_{0.999}Te_{0.7}Se_{0.3}$ [32] and $PbTe_{0.5}Se_{0.5}$:0.0005 (PbI_2) [33]. The Hall carrier concentration is lower than that of Cr-doped PbTe if the Se concentration is low (y = 0.25 and 0.5, Te-rich samples), and increases to be higher than that of Cr-doped PbTe with higher Se concentration (y = 0.75 and 1, Se-rich samples). With increasing Hall carrier concentration, the Seebeck coefficient decreased. This is fitted well by the non-parabolic two-band Kane (TBK) model of PbTe and PbSe where acoustic phonon scattering is considered as the dominant carrier scattering mechanisms in both cases. From this result, the high room-temperature Seebeck coefficient is not obtained by the band structure modification due to resonance and how Cr doping affected the band structure is something need further study to be figured out.

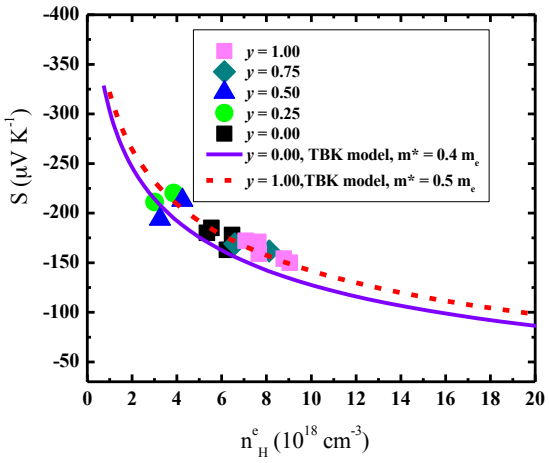

Figure 4.3.9 Room-temperature Pisarenko plots of $Cr_xPb_{1-x}Te_{1-y}Se_y$, (■) $Cr_xPb_{1-x}Te$ (x = 0.01, 0.015, 0.025, and 0.03), (●) $Cr_xPb_{1-x}Te_{0.75}Se_{0.25}$ (x = 0.01 and 0.015), (▲) $Cr_xPb_{1-x}Te_{0.5}Se_{0.5}$ (x = 0.01 and 0.015), (◆) $Cr_xPb_{1-x}Te_{0.25}Se_{0.75}$ (x = 0.01 and 0.015), (■) $Cr_xPb_{1-x}Se$ (x = 0.0025, 0.005, 0.0075, 0.01, and 0.02). The purple solid curve is based on a nonparabolic two-band Kane model (TBK) with the electron effective mass of PbTe m* = 0.4 m_e; the red dashed curve is based on a nonparabolic two-band Kane model (TBK) with the electron effective mass of PbSe m* = 0.5 m_e.

From our systematic optimization of the thermoelectric properties of Cr-doped $PbTe_{1-y}Se_y$ by changing Cr concentration or Te:Se ratio, we have identified the best compositions as: $Cr_{0.015}Pb_{0.985}Te_{0.75}Se_{0.25}$ and $Cr_{0.01}Pb_{0.99}Te_{0.25}Se_{0.75}$. Table 4.3.1 summarizes the room temperature properties of these compositions. The density of both samples are close to their theoretical density and their carrier concentrations are less than 10^{19} cm^{-3}.

Table 4.3.1 Room-temperature properties of Se-rich $Cr_{0.01}Pb_{0.99}Te_{0.25}Se_{0.75}$ and Te-rich $Cr_{0.015}Pb_{0.985}Te_{0.75}Se_{0.25}$ samples.

Composition	S ($\mu V\ K^{-1}$)	σ ($10^4\ S\ m^{-1}$)	PF ($\mu W\ cm^{-1}\ K^{-2}$)	κ ($W\ m^{-1}\ K^{-1}$)	ZT	n_H ($10^{18}\ cm^{-3}$)	μ_H ($cm^2\ V^{-1}\ s^{-1}$)
$Cr_{0.01}Pb_{0.99}Te_{0.25}Se_{0.75}$	-162	8.29	21.70	1.23	0.55	8.12	638
$Cr_{0.015}Pb_{0.985}Te_{0.75}Se_{0.25}$	-220	6.94	24	1.17	0.63	3.87	1120

Figure 4.3.10 summarizes the effect of Te substitutions by Se on the (a) room-temperature and (b) peak *ZT*s at fixed Cr doping levels of 1 atm. % (black squares) and 1.5 atm. % (red circles). As can be seen from the figure, the room-temperature *ZT* increased when the Se concentration increased up to a certain optimum alloying limit and then decreased when it exceeded this limit. High room-temperature *ZT*s of ~0.63 and ~0.55 were obtained by substitution of 25 atm. % and 75 atm. % Te by Se at Cr doping levels of 1.5 atm. % and 1 atm. %, respectively. As shown in Figures 4.3.7 and 4.3.8, at fixed Cr concentrations the best peak *ZTs* are in Se-rich samples. A maximum peak *ZT* of ~1 is obtained in $Cr_{0.01}Pb_{0.99}Te_{0.25}Se_{0.75}$. The peak *ZT*s of all the samples are greater than ~0.7 indicating that Cr doping on PbTe alloyed with PbSe brings the best room

temperature thermoelectric properties without or with minimal reduction of the peak *ZT*s. Hence, the average *ZT* is improved over the whole temperature range that makes the materials promising for power generation applications.

To show clearly this improvement by Cr doping in $PbTe_{1-y}Se_y$, we also plotted the (a) room temperature power factor, (b) room temperature *ZT*, and (c) average *ZT* of $Cr_{0.01}Pb_{0.99}Te_{0.25}Se_{0.75}$ and $Cr_{0.015}Pb_{0.985}Te_{0.75}Se_{0.25}$ as a function of carrier concentration compared with the reported optimized p-type and n-type doped $PbTe_{1-y}Se_y$ in Figure 4.3.11. Similar to n-type doped PbSe [26], both the room temperature power factor and *ZT* value decreased steeply with increasing of the room temperature Hall carrier concentration. In spite of almost the same carrier concentration, Cr-doped $PbTe_{1-y}Se_y$ has much higher room temperature power factor and *ZT* than I-doped $PbTe_{1-y}Se_y$. Although with low peak *ZT* ~1.0 at about 573 K-673 K, the average *ZT* of Cr-doped $PbTe_{1-y}Se_y$ is as high as those of p-type $Na_{0.02}Pb_{0.98}Te_{0.75}Se_{0.25}$ (peak *ZT* ~1.8 at about 850 K) [11] and n-type $PbTe_{0.5}Se_{0.5}$:0.0005 (PbI_2) [33] (peak *ZT*~1.5 at about 625 K), and higher than those of p-type $K_{0.02}Pb_{0.98}Te_{0.15}Se_{0.85}$ (peak *ZT* ~1.7 at about 873 K) [20] and n-type $In_{0.001}Pb_{0.999}Te_{0.7}Se_{0.3}$ [32]. The efficiency of thermal to electrical conversion of these selected compositions is discussed in the next section.

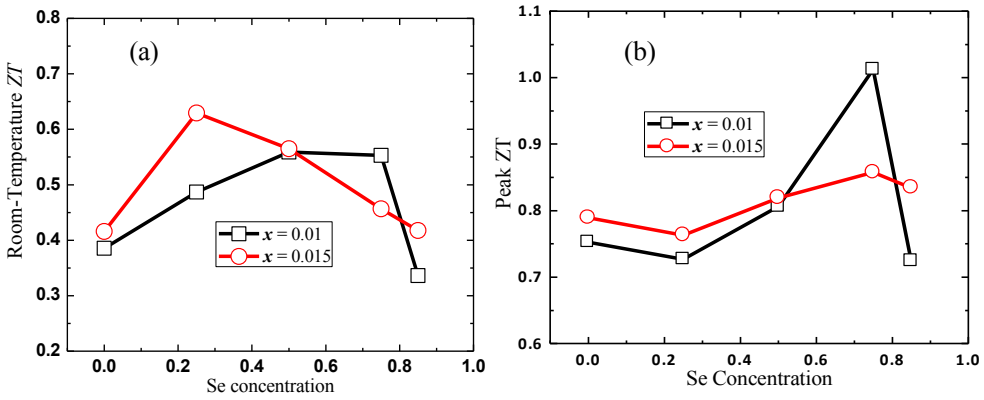

Figure 4.3.10 Se concentration dependence of the room temperature *ZT* and peak *ZT* for $Cr_xPb_{1-x}Te_{1-y}Se_y$.

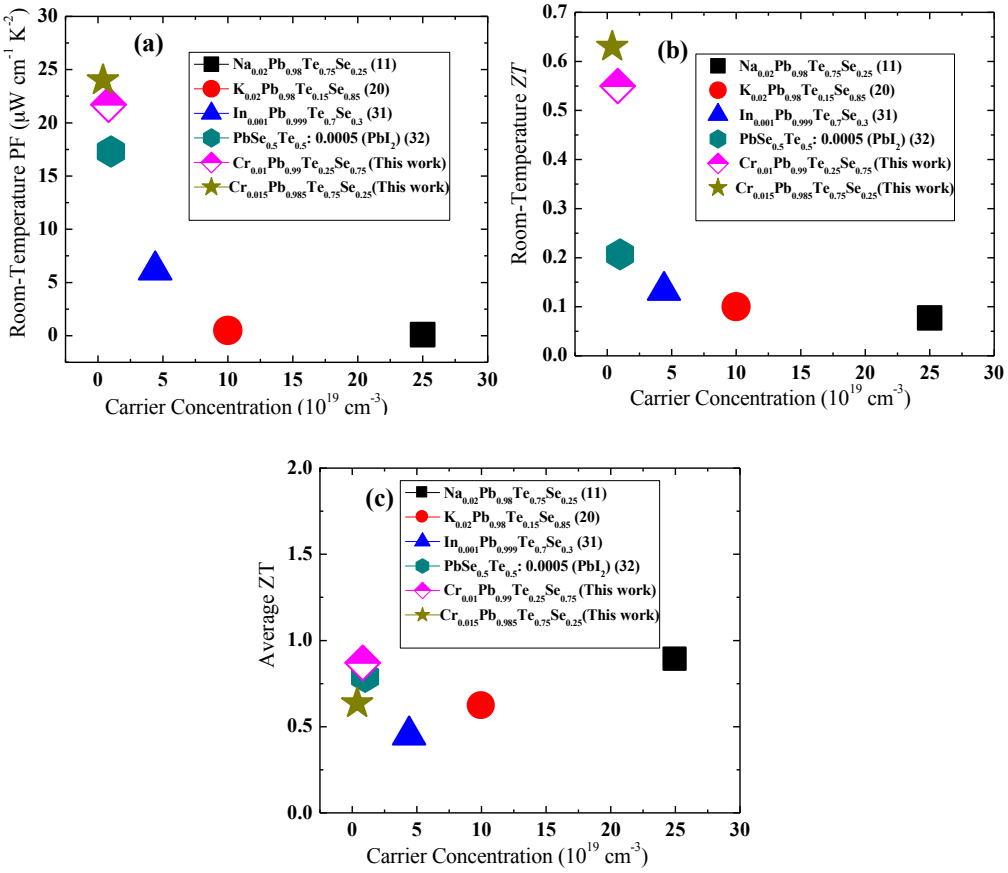

Figure 4.3.11 (a) Room-temperature power factor (b) room temperature *ZT* and (c) Average *ZT*s of $Cr_{0.01}Pb_{0.99}Se_{0.75}Te_{0.25}$ and $Cr_{0.015}Pb_{0.985}Se_{0.25}Te_{0.75}$ as a function of carrier concentration compared with state of the art PbTe-PbSe based compounds of high peak *ZT* values.

The efficiency of a thermoelectric power generator depends on the Carnot efficiency and the thermoelectric figure of merit of the devices [34], which is intrinsic to the materials making up the device. This relation is expressed by Equation 4.3.1.

$$\eta_e = \frac{T_h - T_c}{T_h}\left(\frac{\sqrt{1+Z\overline{T}}-1}{\sqrt{1+Z\overline{T}}+\frac{T_c}{T_h}}\right) \qquad (4.3.1)$$

Where T_h is the hot-side temperature, T_c is the cold-side temperature, and $\overline{T}$ is the average temperature between T_c and T_h. The temperature dependent properties of the legs are incorporated in the $Z\overline{T}$ term in Equation 4.3.1 and replaced by the average ZT over the whole temperature range when calculating the efficiency. One proposed method of improving the efficiency of thermoelectric generators is designing a segmented device where each segment has a high ZT for the temperature anticipated in the segment [35,36]. However, this technique has its own drawbacks in effectiveness since it suffers from the added complexity of bonding, mass diffusion, and thermal expansion mismatch at the interfaces. Hence, it is important to find a single material with better thermoelectric properties to use over the whole temperature range of operation. Here, we propose $Cr_{0.015}Pb_{0.985}Te_{0.75}Se_{0.25}$ and $Cr_{0.01}Pb_{0.99}Te_{0.25}Se_{0.75}$ as potential candidates for single leg device applications to operate from 300 K to 773 K. The leg efficiency can be calculated more accurately, by either Snyder and Ursell [37] or Mahan's [35] discretization methods. In this work, we used Mahan's method where one dimensional heat flow is assumed in the legs and no heat is lost from the sidewalls. The discretized equations in the leg are given in Equations 4.3.2, Equations 4.3.3, and Equations 4.3.4.

$$\frac{dT}{dx} = \frac{JST-Q}{k} \quad (4.3.2)$$

$$\frac{dQ}{dx} = \rho J^2 + JS\frac{dT}{dx} \quad (4.3.3)$$

$$\frac{dV}{dx} = -\rho J - S\frac{dT}{dx} \quad (4.3.4)$$

Where J, Q, ρ, V, S, k and T are the current density, heat flux density, electrical resistivity, voltage, Seebeck coefficient, thermal conductivity, and temperature, respectively. The leg efficiency is calculated from the output power and input heat flux into the leg by:

$$\eta_{leg} = \frac{J(V_c-V_h)}{Q_h} \quad (4.3.5)$$

The set of coupled first order differential Equations (4.3.2), (4.3.3), (4.3.4) were iteratively solved with the appropriate temperature boundary conditions at different current densities until the optimum value of J that maximizes the leg efficiency is found. We calculated the efficiency of the best compounds, $Cr_{0.015}Pb_{0.985}Te_{0.75}Se_{0.25}$ and $Cr_{0.01}Pb_{0.99}Te_{0.25}Se_{0.75}$, as shown in Figure 4.3.12 in comparison with the efficiency of the best-optimized Cr doped PbSe ($Cr_{0.005}Pb_{0.995}Se$), Cr doped PbTe ($Cr_{0.025}Pb_{0.975}Te$), and I doped PbTe ($I_{0.0012}PbTe_{0.9988}$). An efficiency of ~10 % and ~12 % is obtained for the individual legs of $Cr_{0.015}Pb_{0.985}Te_{0.75}Se_{0.25}$ and $Cr_{0.01}Pb_{0.99}Te_{0.25}Se_{0.75}$, respectively, when thecold-side temperature is set at 300 K and hot-side temperature at 773 K. In spite of having high ZT exceeding 1.4 near 700 K for $I_{0.0012}PbTe_{0.9988}$, the efficiency is still lower than that of $Cr_{0.01}Pb_{0.99}Te_{0.25}Se_{0.75}$, especially below 700 K. This result is also comparable with the efficiency of other thermoelectric materials withcold-side temperature 300 K and hot-side temperature 773 K, for example Bi_2Te_3-Bi_2Se_3-Bi_2S_3 (12.5%) [38], PbSe:Al

(9.4%) [38,15], half Heuslers (8.4%), [38,39], filled Skutterrudites (13.1%) [38,40], and PbTe: La (6.7%) [38,41]. This high single-leg efficiency over a wide range of temperatures comes from the improvement of the room-temperature *ZT* and then the enhanced average *ZT* over the whole temperature range.

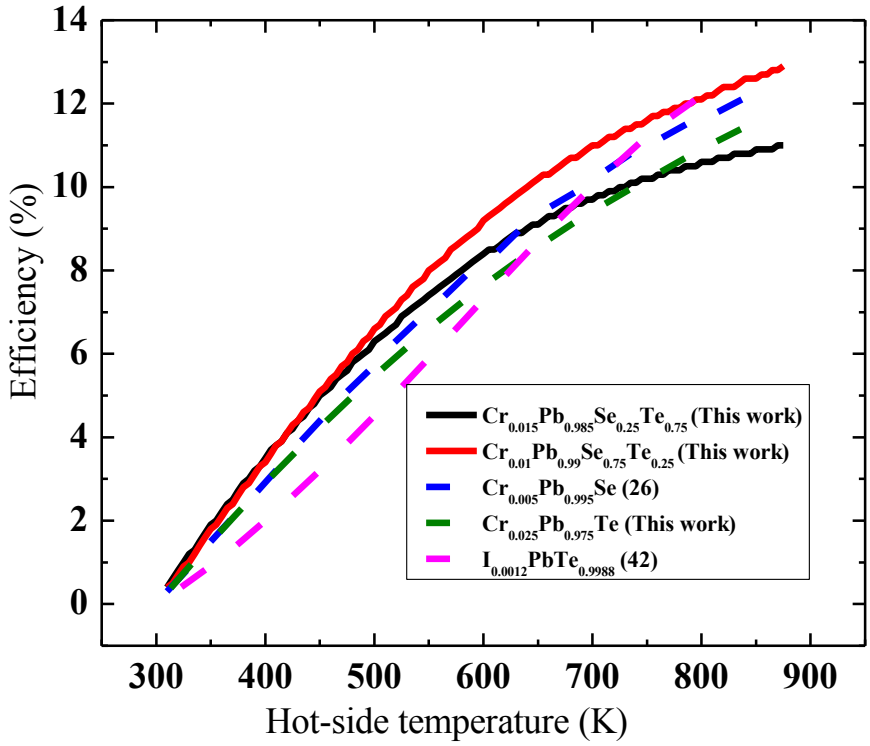

Figure 4.3.12 Temperature dependence of the calculated leg efficiencies of $Cr_{0.015}Pb_{0.985}Te_{0.75}Se_{0.25}$ (solid black line), $Cr_{0.01}Pb_{0.99}Te_{0.25}Se_{0.75}$ (solid red line), $Cr_{0.005}Pb_{0.995}Se$ [26] (dashed blue line), $Cr_{0.025}Pb_{0.975}Te$ (dashed green line), and $I_{0.0012}PbTe_{0.9988}$ [42] (dashed pink line) with a cold-side temperature at 300 K.

4.4. Conclusion

In this systematic study of Cr doping in $PbTe_{1-y}Se_y$, a high figure of merit of ~0.6 at room temperature was achieved in Te-rich $Cr_{0.015}Pb_{0.985}Te_{0.75}Se_{0.25}$ resulting from the combination of a higher power factor and a lower thermal conductivity. A peak *ZT* of ~1 was obtained in Se-rich $Cr_{0.01}Pb_{0.99}Te_{0.25}Se_{0.75}$ at about 573 to 673 K with a room temperature *ZT* of ~0.5. The calculated thermal to electrical conversion efficiencies of Te-rich $Cr_{0.015}Pb_{0.985}Te_{0.75}Se_{0.25}$ and Se-rich $Cr_{0.01}Pb_{0.99}Te_{0.25}Se_{0.75}$ are ~10 % and ~12 %, respectively, with hot-side temperature of 773 K and cold-side temperature of 300 K and hence could be potentially useful for medium-temperature power generation applications.

References

[1] G. J. Snyder and E. S. Tobber, *Nature Mater.* **7,** 105, (2008).

[2] Z. G. Chen, G. Han, L. Yang, L. Cheng, and J. Zou, Nanostructured Thermoelectric Materials: Current Research and Future Challenge, Progress in *Natural Science: Materials International,* **22**, 535, (2012).

[3] T. C. Harman, P. J. Taylor, M. P. Walsh and B. E. Laforge, *Science,* **297,** 2229**,** (2002).

[4] M. S. Dresselhaus, G. Chen, M. Y. Tang, R. Yang, H. Lee, D. Wang, Z. F. Ren, J. P. Fleurial and P. Gogna, *Adv. Mater.,* **19**, 1043, (2007).

[5] B. C. Sales, D. Mandrus and R. K. Williams, *Science,* **272**, 1325, (1996).

[6] H. Kleinke, *Chem. Mater.,* **22,** 604, (2010).

[7] Q. Zhang, T. Sun, F. Cao, M. Li, M. H. Hong, J. K. Yuan, Q. Y. Yan, H. H. Hng, N. Q. Wu and X. G. Liu, *Nanoscale,* 2, 1256, (2010).

[8] W. S. Liu, X. Yan, G. Chen and Z. F. Ren, *Nano Energy,* **1,** 42, (2012).

[9] M. S. Dresselhaus, G. Chen, M. Y. Tang, R. G. Yang, H. Lee, D. Z. Wang, Z. F. Ren, J. P. Fleurial and P. Gogna, in Materials and Technologies for Direct Thermal-to-Electric Energy Conversion, MRS Symp. Proc. Eds: J. Yang, T. P. Hogan, R. Funahashi, G. S. Nolas, *Materials Research Society Press, Pittsburgh, PA,* pp. 3-12, (2005).

[10] M. S. Dresselhaus and J. P. Heremans, in *Thermoelectrics Handbook: Macro to Nano*, Ed: D. M. Rowe, Taylor and Francis, CRC, Boca Raton, FL, Ch. 39, pp. 1-24, (2006).

[11] Y. Pei, X. Shi, A. LaLonde, H. Wang, L. Chen and G. J. Snyder, *Nature,* **473**, 66, (2011).

[12] S. N. Girard, J. He, X. Zhou, D. Shoemaker, C. M. Jaworski, C. Uher, V. P. Dravid, J. P. Heremans and M. G. Kanatzidis, *J. Am. Chem. Soc.,* **133,** 16588, (2011).

[13] Y. Pei, A. D. LaLonde, N. A. Heinz, X. Shi, S. Iwanaga, H. Wang, L. Chen and G. J. Snyder, *Adv. Mater.,* **23,** 5674, (2011).

[14] J. P. Heremans, V. Jovovic, E. S. Toberer, A. Saramat, K. Kurosaki, A. Charoenphakdee, S. Yamanaka and G. J. Snyder, *Science,* **321,** 554, (2008).

[15] Q. Y. Zhang, H. Wang, W. Liu, H. Wang, B. Yu, Q. Zhang, Z. Tian, G. Ni, S. Lee, K. Esfarjani, G. Chen and Z. F. Ren, *Energy Environ. Sci.,* **5,** 5246, (2012).

[16] J. P. Heremans, B. Wiendlocha and A. M. Chamoire, *Energy Environ. Sci.,* **5,** 5510, (2012).

[17] C. M. Jaworski, B. Wiendlocha, V. Jovovic and J. P. Heremans, *Energy Environ. Sci.,* **4,** 4155, (2011).

[18] D. M. Rowe CRC Handbook of Thermoelectrics, CRC Press, Boca Raton London New York Washington, D.C., (1995).

[19] A. D. Lalonde, Y. Pei, H. Wang and G. J. Snyder, *Mater. Today,* **14,** 526, (2011).

[20] Q. Zhang, F. Cao, W. Liu, K. Lukas, B. Yu, S. Chen, C. Opeil, D. Broido, G. Chen and Z. F. Ren, *J. Am. Chem. Soc.,* **134,** 10031, (2012).
[21] B. Basu, S. Bhattacharya, R. Bhatt, A. Singh, D. K. Aswal and S. K. Gupta, *J. Electron. Mater.,* **42,** 2292, **(**2013).
[22] Z. P. Wen, I. Yoshio, I. Yukihiro, S. Yoshikazi, J. X. Peng and Z. G. Tian, *Chin. Phys. Lett.,* **22,** 2103, (2005).
[23] P. Zhu, Y. Imai, Y. Isoda, Y. Shinohara, X. Jia, G. Ren and G. Zou, *Mater. Transactions,* **45,** 3102, (2004).
[24] E. Grodzicka, W. Dobrowolski, T. Story, A. Wilamowski and B. Witkowska, *Ins. Phys. Conf. Ser., No* **144**: *section 3* (1995).
[25] B. Paul and P. Banerji, *J. Appl. Phys.,* **109,** 103710, (2011).
[26] Q. Zhang, E. K. Chere, J. Sun, F. Cao, K. Dahal, S. Chen, G. Chen and Z. Ren, *Adv. Energy Mater.,*1500360, (*2015*).
[27] M. D. Nielsen, E. M. Levin, C. M. Jaworski, K. Schmidt-Rohr and J. P. Heremans, *Phys. Rev.,* B, **85,** 045210, (2012).
[28] D. Parker and D. J. Singh, *Phys. Rev.,* B, **82,** 035204, (2010).
[29] Z. Tian, J. Garg, K. Esfarjani, T. Shiga, J. Shiomi and G. Chen, *Phys. Rev.* B, **85** 184303, (2012).
[30] X. Yan, B. Poudel, Y. Ma, W. S. Liu, G. Joshi, H. Wang, Y. Lan, D. Wang, G. Chen and Z. F. Ren, *Nano Lett.,* **10,** 3373, (2010).
[31] H. Wang, Y. Pei, A. D. LaLonde and G. J. Snyder, *Proc. Natl. Acad. Sci.,* USA, **25,** 109, 9705–9709, (2012).
[32] A. Bali, H. Wang, G. J. Snyder and R. C. Mallik, *J. Appl. Phys.*, **116,** 033707, (2014).
[33] P. K. Rawat, B. Paul and P. Banerji, *Nanotechnology,* **24,** 215401, (2013).
[34] H. J. Goldsmid, Introduction to Thermoelectricity, Springer-Verlag, Berlin Heidelberg, (2010).
[35] G. D. Mahan, *J. Appl. Phys.,* **70,** 4551, (1991).
[36] N. B. Elmer, J. Chin and G. H. Reynolds, in *Proceedings of the Third International Conference on Thermoelectric Energy Conversion*, Arlington, TX, edited by K. R. Rao (IEEE, New York, 1980), p. 105.
[37] G. J. Snyder and T. S. Ursell, *Phys. Rev. Lett.,* **91,** 148301, (2003).
[38] W. S. Liu, K. C. Lukas, K. McEnaney, S. Lee, Q. Zhang, C. Opeil, G. Chen and Z. F. Ren, *Energy Environ. Sci.,* **6,** 552, (2013).
[39] G. Joshi, X. Yan, H. Z. Wang, W. S. Liu, G. Chen and Z. F. Ren, *Adv. Energy Mater.,* **1,** 643, (2011).
[40] X. Shi, J. Yang, J. R. Salvador, M. F. Chi, J. Y. Cho, H. Wang, S. Q. Bai, J. H. Yang, W. Q. Zhang and L. D. Chen, *J. Am. Chem. Soc.,* **133**, 7837, (2011).
[41] Y. Z. Pei, J. Lensch-Falk, E. S. Toberer, D. L. Medlin and G. J. Snyder, *Adv. Func. Mater.,* **21**, 241, (2011).
[42] A. D. LaLonde, Y. Pei and G. J. Snyder, *Energy Environ. Sci.,* **4,** 2090, (2011).

CHAPTER 5: STUDIES OF THE THERMOELECTRIC PERFORMANCE OF $PbTe_{1-y}S_y$ ALLOY

5.1. Introduction

In the preceding chapters, we have pointed out that Pb-chalcogenides have high peak *ZT* values from 573 K-873 K. These high *ZT* values are achieved by optimization of the thermal and electronic transport properties by different techniques such as optimized carrier concentration by controlled doping [1-4], enhanced Seebeck coefficient because of resonant doping [5-8], or band convergence [9-11], enhanced Hall mobility due to weak electron-phonon coupling [12], or modulation doping [13,14], and lowered thermal conductivity with intrinsic complex structures [15-18], or artificial nanostructures [19,20]. Additional strategies to further increase the *ZT* values are always pursued. Due to their intrinsic high valley degeneracy yielding high Seebeck coefficient [9], and intrinsic phonon anharmonicity, yielding low thermal conductivity [21,22], peak *ZT*s as high as ~2 have been obtained in p-type [23-25], and ~1.5 in n-type lead chalcogenides [26]. However, it is worth to point out that the average *ZT* over the whole temperature range (300 K-873 K) is still low due to the very low *ZT*s near room temperature. Several recent studies show gradual progress on the improvement of the *ZT* below 200 ^{o}C, such as by combination of the nanostructures and complex band structure [27] alloying PbTe with MgTe to stabilize the optimal carrier concentration in the large temperature range [28], we also discussed in chapter 3 and 4 that our work on Cr doping of PbSe and $PbTe_{1-x}Se_x$ effectively enhanced the room temperature power factor and *ZT* [29,30]. It has been also predicted that deep defect states in narrow band-gap semiconductors could lead to the

enhancement of the thermoelectric properties by annihilating the minority carriers, which helps to keep the Seebeck coefficient high and the thermal conductivity low at higher temperatures [31-37]. Normally, in most researches on lead chalcogenides, the carrier concentration was optimized to achieve high peak *ZT* values at higher temperature [2-4]. However, this strategy failed to achieve high average *ZT* across a wide range of temperature in particular in n-type lead chalcogenides due to the associated lower *ZT* values near room temperature. Optimizing the carrier concentration to achieve high *ZT* values at lower temperature by deep lying doping can enhance the average *ZT* in a wide temperature range. In this chapter, we will discuss the improvement of room temperature and average *ZT* in $PbTe_{1-x}S_x$ by combination of deep lying states in indium-doped PbTe [34], minimizing the thermal conductivity by alloy scattering [38-41], and the spinodal decomposition [25,42-45].

5.2. Experimental Methods

Ingots with nominal compositions $Pb_{1-x}In_xS$, $Pb_{1-x}In_xTe$, and $Pb_{0.98}In_{0.02}Te_{1-y}S_y$ ($0< x <0.03$, $0< y <1$), were prepared by melting the raw materials (Pb granules, 99.99%; Te chunks, 99.999%; Se granules, 99.99%; S pieces, 99.99%; and In powder, 99.99%) inside sealed quartz tube with carbon coating. The quartz tubes were slowly raised to 1100 ^oC and kept for 10 h, then quenched from 1100 ^oC into water. The obtained ingots were cleaned and hand milled in a glove box. The reason we used hand mill instead of ball mill is to avoid sample softening above 500 ^oC. The obtained powder was loaded into a graphite die and consolidated by hot pressing. X-ray diffraction spectra analysis was conducted on a PANalytical multipurpose diffractometer with an X'celerator detector

(PANalytical X'Pert Pro). The microstructures were investigated by a scanning electron microscope (SEM, LEO 1525) and a high-resolution transmission electron microscope (HRTEM, JEOL 2100F). The electrical resistivity (ρ) and Seebeck coefficient (S) were simultaneously measured on a commercial system (ULVAC ZEM-3). The thermal conductivity k was calculated using $k = D\alpha C_p$, where D is volumetric density determined by the Archimedes method, α is the thermal diffusivity obtained on a laser flash apparatus (Netzsch LFA 457), and C_p is the specific heat measured on a differential scanning calorimetry thermal analyzer (Netzsch DSC 404 C) (shown in Figure S1). The Hall carrier concentration n_H at room temperature was measured using the PPMS (Physical Properties Measurement System, Quantum Design). The Hall mobility μ_H was calculated using $\mu_H = \sigma/(qn_H)$. The uncertainty for the electrical conductivity is 3%, the Seebeck coefficient 5%, the thermal conductivity 4%, so the combined uncertainty for power factor is 10% and that for ZT value is 11%. Error bars were not used in the Figures to increase the readability of the curves.

5.3. Thermoelectric Properties of $In_{0.02}Pb_{0.98}Te_{1-y}S_y$

Indium can create deep defect states in PbTe, which is expected to lead to enhancement of the high temperature TE properties by keeping higher Seebeck coefficient and lower thermal conductivity at higher temperature due to the suppressed bipolar effect [31-37]. On the other hand, it is difficult for the deep impurities to ionize to the conduction band, and only a fraction of the impurities contributed to free carriers. Consequently, the carrier concentration is limited to only ~2×10^{18} cm^{-3} at room temperature and is much lower than the carrier concentration of I-doped PbTe [46], which is shallow lying doping [36]. PbS

has also recently attracted much attention due to the advantage of abundance, inexpensive and possible higher operation temperature [6,47-49]. Both n-type (Cl-doped) [48] and p-type (Na-doped) [49] PbS have *ZT* values higher than 1 at about 925 K. Moreover, both In-doped PbTe and In-doped PbS have negative Seebeck coefficients, similar to reported In-doped PbSe [3], indicating consistent n-type doping. With increasing temperature, the band gap (~ 0.42 eV at 300 K) of PbS increases [47,50], showing no obvious sign of bipolar effect in highly In-doped PbS. Since PbS is lighter than PbTe and PbSe, its lattice thermal conductivity is higher than those of both PbTe and PbSe. This property is also observed in Cl-doped PbS without nanostructures [47], that has comparable lowest lattice thermal conductivity and highest *ZT* value.

By alloying PbTe with PbS, the electrical conductivity of In-doped PbTe was found to increase at fixed indium concentration. Many studies have shown the existence of a miscibility gap in the phase diagram of ternary $PbTe_{1-y}S_y$ compound with possibility for spinodal decomposition [25,42-45]. Figure 5.3.1 presents the XRD patterns for $In_{0.02}Pb_{0.98}Te_{1-y}S_y$ (y = 0.05, 0.10, 0.20, 0.30, and 1.0). There is no impurity phase induced by In doping. Both $In_{0.02}Pb_{0.98}Te$ (y = 0) and $In_{0.005}Pb_{0.995}S$ (y = 1) are single phase crystallized in face-centered cubic rock salt structure (space group $Fm\bar{3}m$). With increasing S content, all peaks gradually shift to right when $y \leq 0.2$, indicating the solid solution of PbS in PbTe, which is also confirmed by good fitting to Vegard's law (Figure 5.3.1 (b)). A second phase (S-rich phase) was detected when $y \geq 0.1$ due to the spinodal decomposition. For convenience, we still use $In_{0.02}Pb_{0.98}Te_{1-y}S_y$ to represent the corresponding compounds.

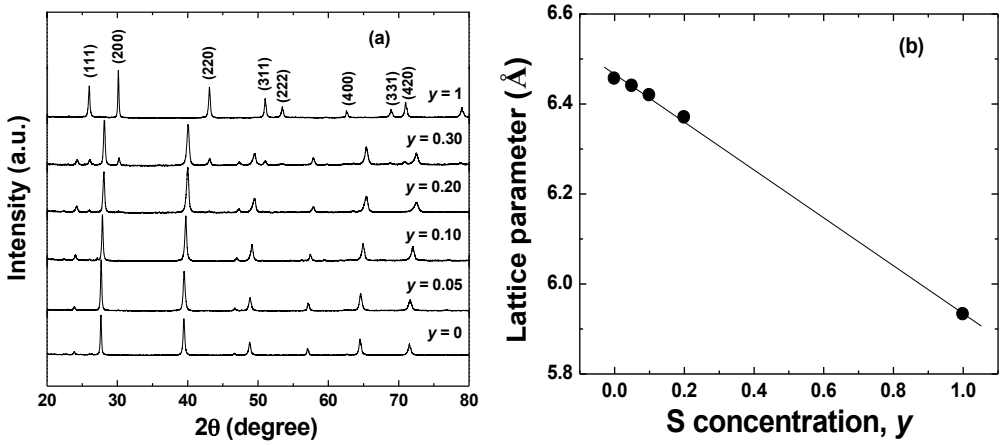

Figure 5.3.1 (a) XRD patterns for $In_{0.02}Pb_{0.98}Te_{1-y}S_y$ (y = 0.05, 0.10, 0.20, and 0.30) compared with $In_{0.02}Pb_{0.98}Te$ and $In_{0.005}Pb_{0.995}S$. (b) The lattice parameter relation with S concentration y.

Figure 5.3.2 shows the temperature dependence of (a) electrical conductivity, (b) Seebeck coefficient, (c) power factor, (d) thermal diffusivity, (e) total thermal conductivity and lattice thermal conductivity, and (f) ZT for $In_{0.02}Pb_{0.98}Te_{1-y}S_y$ (y = 0.05, 0.10, 0.20, and 0.30) at fixed In concentration. With increasing y, the electrical conductivity increased as expected and the Seebeck coefficient decreased, as a result of the increased Hall carrier concentration (Figure 5.3.3 (a)). The incorporation of PbS could move the impurity level from above the valence band maximum close to the bottom of the conduction band, with tendency to become shallow lying doping.

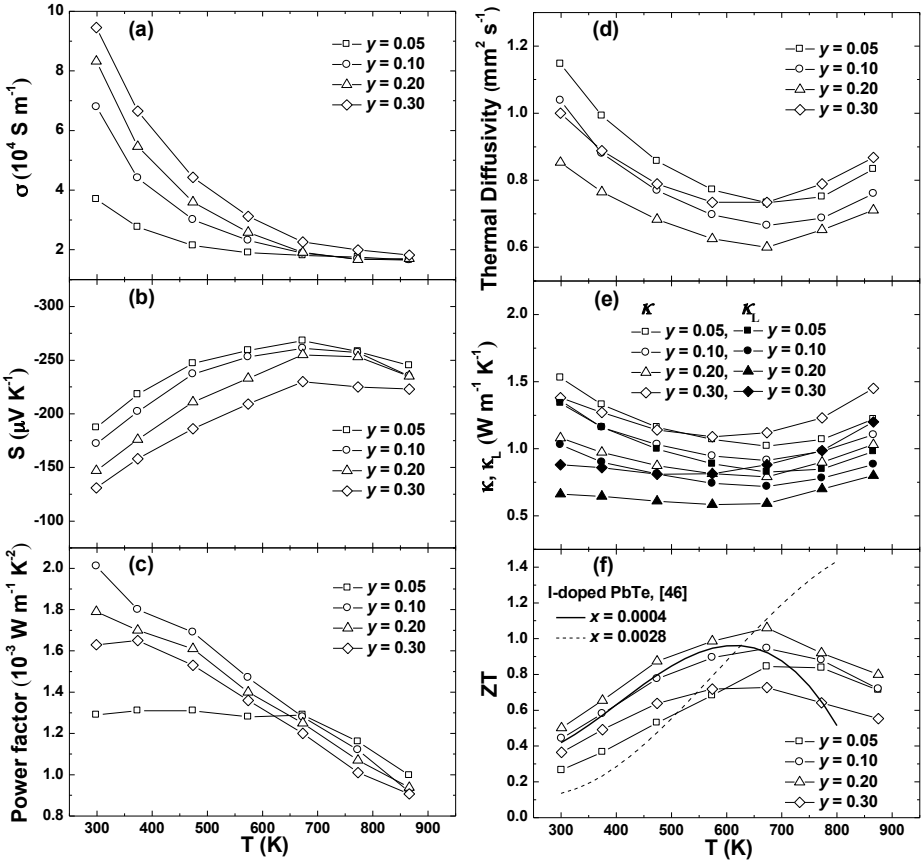

Figure 5.3.2 Temperature dependence of (a) electrical conductivity, (b) Seebeck coefficient, (c) power factor, (d) thermal diffusivity, (e) total thermal conductivity and lattice thermal conductivity, and (f) *ZT* for $In_{0.02}Pb_{0.98}Te_{1-y}S_y$ (y = 0.05, 0.10, 0.20, and 0.30). The *ZT* value of $PbTe_{1-x}I_x$ is plotted in (f) for comparison [46].

The room-temperature Pisarenko relation for $In_{0.02}Pb_{0.98}Te_{1-y}S_y$ (Figure 5.3.3 (b)) indicated no resonant states in agreement with the first principles calculation [34]. Due to deep lying doping, the n_H is difficult to reach that high when $y \leq 0.2$, but this relative low n_H lead to high room temperate *ZT* in this system.

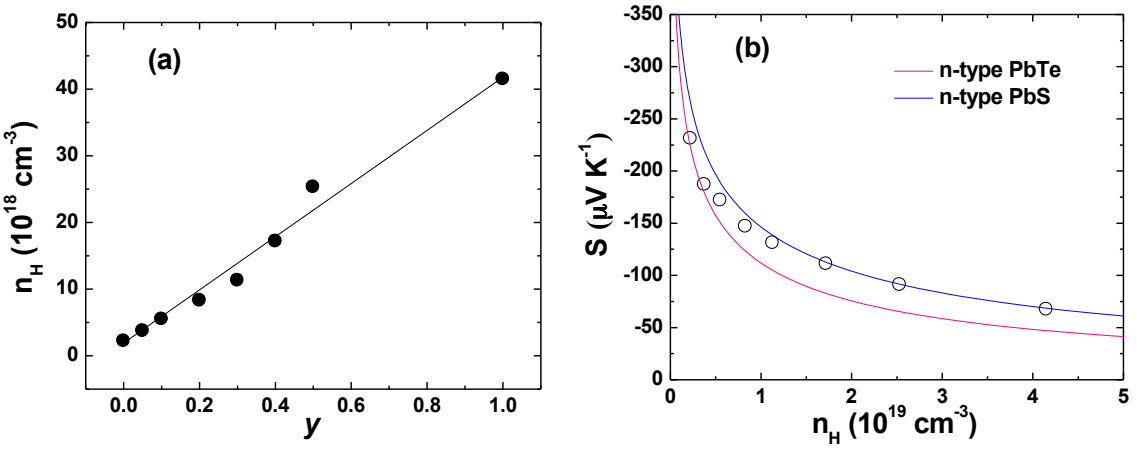

Figure 5.3.3 (a) Room-temperature Hall carrier concentration as a function of S concentration y (b) Room temperature Pisarenko plots for $In_{0.02}Pb_{0.98}Te_{1-y}S_y$ (y = 0, 0.05, 0.10, 0.20, 0.30, 0.40, 0.50, and 1). Red curve is based on single Kane model (SKB) with the electron effective mass of PbTe m* = 0.25 m_e. Blue curve is based on single Kane model (SKB) with the electron effective mass of PbS m* = 0.39 m_e.

Figure 5.3.4 shows the calculated power factor (a) and *ZT* (b) as a function of Hall carrier concentration for n-type PbTe and PbS at different temperature (300 K and 600 K). The transport coefficients for PbTe and PbS were calculated using a single non-parabolic Kane band model (SKB) that includes deformation potential scattering of L-point conduction band electrons by acoustic phonons and polar scattering of electrons by optical phonons. The optimal carrier concentration for both peak power factor and peak *ZT* increased with increasing operation temperature and increasing PbS concentration. The measured room temperature power factor is consistent with the calculated results. However, lower power factor values (Figure 5.3.4 (a)) caused by alloy scattering induced lower Hall mobility. This lower Hall mobility also lowered the electronic thermal conductivity, leading to a peak room temperature *ZT* of ~ 0.5 in $In_{0.02}Pb_{0.98}Te_{0.8}S_{0.2}$ with

Hall carrier concentration of ~8×10^{18} cm^{-3}, just in between of the calculated peak *ZT*s of n-type PbTe and PbS at room temperature (Figure 5.3.4 (b)). At normal doping, the high temperature *ZT* will decrease dramatically due to the bipolar effect with this relative low n_H, like I-doped PbTe (solid line) shown in Figure 2 (f) [46]. However, in this case, electrons in deep lying states annihilated the minority carriers, which kept the high Seebeck coefficient, low thermal conductivity, and then still decent *ZT* at higher temperature, resulting in engineering figure of merit (more accurate estimation of average *ZT*), $(ZT)_{eng}$, even comparable with optimized composition with very high peak *ZT* by I doping (n_H is ~4×10^{19} cm^{-3}) (dashed line) [46]. When $y = 0.3$, the carrier concentration increased to ~ 1.1×10^{19} cm^{-3}, whereas the bipolar temperature decreased in spite of the increase in band gap by incorporation of PbS, which indicated the change of the deep lying doping to the shallow lying doping.

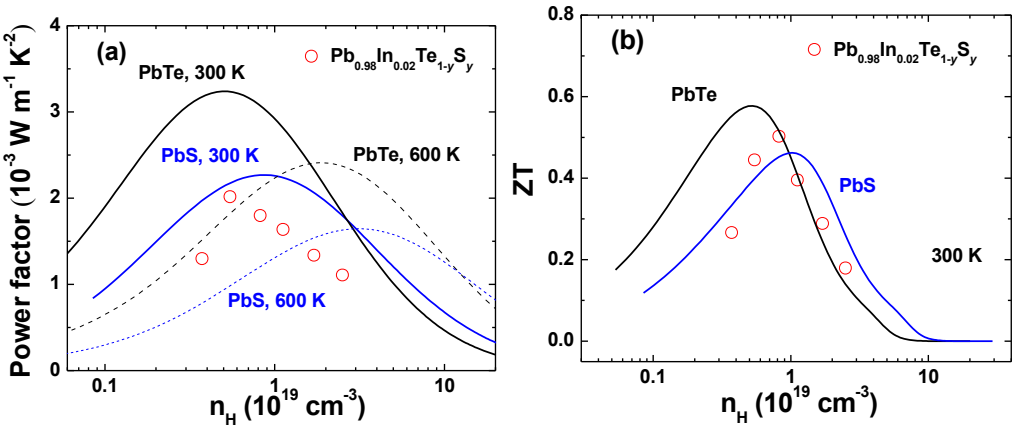

Figure 5.3.4 Room-temperature power factor (a) and *ZT* (b) as a function of Hall carrier concentration for $In_{0.02}Pb_{0.98}Te_{1-y}S_y$ (y = 0.05, 0.10, 0.20, 0.30, 0.40, and 0.50). Black curve is calculated power factor (a) and *ZT* (b) as a function of Hall carrier concentration for n-type PbTe, blue curve is calculated power factor (a) and *ZT* (b) as a function of Hall carrier concentration for n-type PbS. The dashed lines represent the power factor at 600 K. All the calculations are based on single Kane model (SKB). We used the fitted lattice thermal conductivity of $In_{0.02}Pb_{0.98}Te_{1-y}S_y$ for the calculation of the room temperature *ZT*.

Incorporation of PbS onto PbTe not only increased the electrical conductivity, but also strongly decreased the lattice thermal conductivity. The entire lattice thermal conductivity of $In_{0.02}Pb_{0.98}Te_{1-y}S_y$ (y = 0.05, 0.10, 0.20, and 0.30) (Figure 5.3.2(e)) decreased compared to that of In-doped PbTe. The lowest lattice thermal conductivity is ~0.6 W m^{-1} K^{-1} at about 673 K for $Pb_{0.98}In_{0.02}Te_{0.8}S_{0.2}$. Figure 5.3.5 shows the calculated room temperature lattice thermal conductivity of $In_{0.02}Pb_{0.98}Te_{1-y}S_y$ ($0 \leq y < 1$) and $In_{0.005}Pb_{0.995}S$. Unlike the $PbTe_{1-y}Se_y$ system, that has lowest lattice thermal conductivity at around y = 0.5 due to alloy scattering [30,38], there are two inflecting points (y = 0.20 and 0.95) in $PbTe_{1-y}S_y$ system. According to the XRD patterns (Figure 5.3.1a), only four compositions (y = 0, 0.05, 0.95, and 1, with open ovals in Figure 5.3.5) are single phase. The dramatic k_L decrease in $In_{0.02}Pb_{0.98}Te_{0.95}S_{0.05}$ and $In_{0.02}Pb_{0.98}Te_{0.05}S_{0.95}$ is the result of effective alloying. Other compositions are within the immiscible gap, having two phases (Te-rich phase and S-rich phase) confirmed by both XRD in Figure 5.3.1 (a) and SEM images in Figure 5.3.5 (a)-(f) (only shown compositions with y = 0.10, 0.20, 0.30, 0.50, 0.70, and 0.90 (filled circles)) with the same naturally formed striped structure, but different width of the strips. All these compositions underwent spinodal decomposition without nucleation barrier, which continuously contributed to the decrease of k_L. The lowest room temperature k_L is ~ 0.68 W m^{-1} K^{-1} for $In_{0.02}Pb_{0.98}Te_{0.8}S_{0.2}$ with the thinnest strips (~30 nm in width) (Figure 5.3.5 (b)). Even thinner strips (~2 nm) coming from nanoscale compositional fluctuations in this composition were detected at many places by transmission electron microscopy (TEM) and are shown in Figure 5.3.6 (a). More contributions for lower lattice thermal conductivity also comes from the partial

nucleation and growth features in some regions, like the nanocrystals ~30 nm in Figure 5.3.6 (b) [44,45], and many edge dislocations in Figure 5.3.6 (c), where the variety of image contrast and the bend of atomic strings induced by the dislocations are remarkable, and the inserted half planes are clearly seen in the filtered image [29,30].

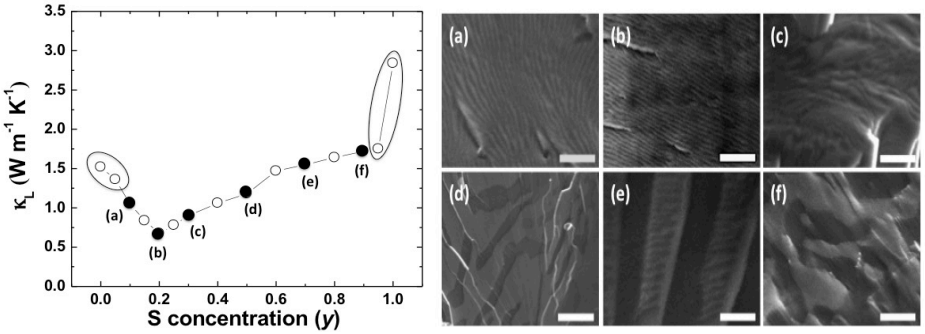

Figure 5.3.5 Room-temperature lattice thermal conductivity for $In_{0.02}Pb_{0.98}Te_{1-y}S_y$ ($0 \leq y < 1$) and $In_{0.005}Pb_{0.995}S$. The SEM images for different composition (filled circles) are shown in Figure (a)-(f), respectively. The scale bar is 200 nm for (a), (b), (c), (e), and (f), and 2 mm for (d).

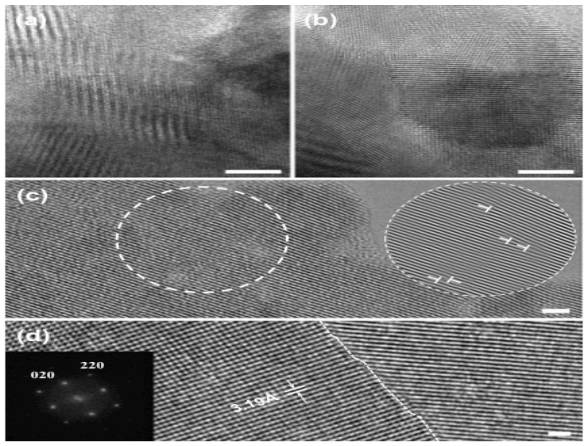

Figure 5.3.6 TEM images for $In_{0.02}Pb_{0.98}Te_{0.8}S_{0.2}$, showing spinodal decomposition (a), nanograins (b), many edge dislocations, and the extra half planes marked by ⊥ in magnified filtered image of the circular area (c), and clean grain boundary (d). FFT of the left area of the boundary is presented in inset to show the good crystallization. The scale bars are 10 nm for (a), and (b), and 2 nm for (c), and (d).

Figure 5.3.6 (d) is a [001] high-resolution TEM image for a grain boundary, the inserted fast Fourier transform (FFT) of the left area on the boundary showing the well crystallization as cubic structure $Fm\bar{3}m$ which are in consistent with the XRD result. The clean boundaries and good crystallinity are beneficial to the transport of charge carriers [19].

We calculated the engineering figure of merit, $(ZT)_{eng}$, (that is a more accurate estimate of the average ZT that measures the cumulative performance at a given T_h and T_c) and the efficiency of $In_{0.02}Pb_{0.98}Te_{0.8}S_{0.2}$. Figure 5.3.7 shows the calculated $(ZT)_{eng}$ and efficiency of $Pb_{0.98}In_{0.02}Te_{0.8}S_{0.2}$ plotted together with Cr-doped $PbTe_{1-y}Se_y$ [30], I-doped $PbTe_{1-y}Se_y$ [51], Cl-doped $PbSe_{1-y}S_y$ [52], Cl-doped $PbTe_{1-x-y}Se_xS_y$ [53], Cl-doped $PbS_{1-y}Te_y$ [54], and In-doped $PbTe_{1-y}Se_y$ [55] for comparison. We used cumulative temperature dependent (CTD) model [56] to calculate the engineering $(ZT)_{eng}$ and efficiency, where the maximum efficiency and engineering ZT are expressed in Equation 5.3.1 an Equation 5.3.3 respectively.

$$\eta_{\max} = \eta_c \frac{\sqrt{1+(ZT)_{eng}\alpha_1\eta_c^{-1}}-1}{\alpha_0\sqrt{1+(ZT)_{eng}\alpha_1\eta_c^{-1}}+\alpha_2} \tag{5.3.1}$$

$$\alpha_i = \frac{S(T_h)\Delta T}{\int_{T_c}^{T_h} S(T)\,dT} - \frac{\int_{T_c}^{T_h}\tau(T)\,dT}{\int_{T_c}^{T_h} S(T)\,dT} W_T\eta_c - iW_J\eta_c \quad (i = 0,1 \text{ and } 2) \tag{5.3.2}$$

$$(ZT)_{eng} = \frac{\left(\int_{T_c}^{T_h} S(T)\,dT\right)^2}{\int_{T_c}^{T_h}\rho(T)\,dT\int_{T_c}^{T_h}\kappa(T)\,dT}\Delta T \tag{5.3.3}$$

Where $W_J = \dfrac{\int_{T_c}^{T_h}\int_{T}^{T_h}\rho(T)\,dT\,dT}{\Delta T\int_{T_c}^{T_h}\rho(T)\,dT}$ and, $W_T = \dfrac{\int_{T_c}^{T_h}\int_{T}^{T_h}\tau(T)\,dT\,dT}{\Delta T\int_{T_c}^{T_h}\tau(T)\,dT}$

$(ZT)_{eng}$ is the engineering figure of merit as a direct indicator, representing overall performance of the material at a given T_h and T_c, where all the thermoelectric transport properties (Seebeck coefficient ($S(T)$), electric resistivity ($\rho(T)$), thermal conductivity ($\kappa(T)$), and Thomson coefficient ($\tau(T)$) are temperature dependent. W_J and W_T are weight factors providing a practical contribution of Joule and Thomson heat respectively.

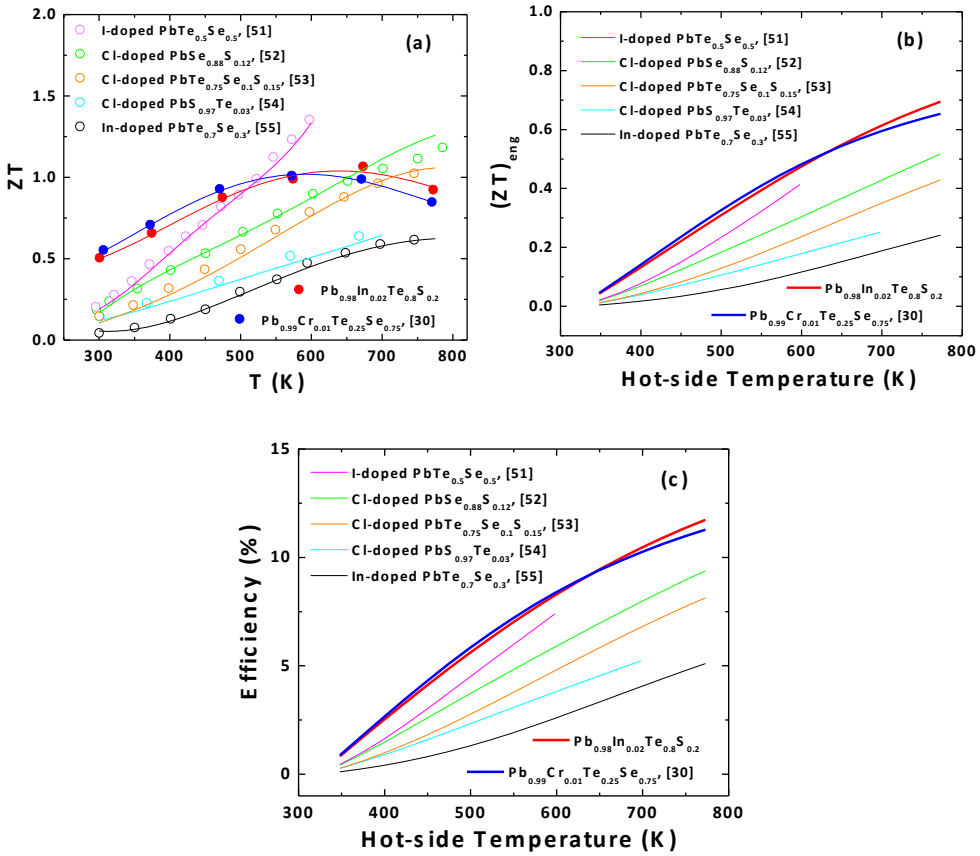

Figure 5.3.7 Temperature dependence of (a) ZT, (b) $(ZT)_{eng}$, and (c) Device efficiency for $In_{0.02}Pb_{0.98}Te_{0.8}S_{0.2}$ in comparison with the other reported n-type ternary and quaternary lead chalcogenides: Cr-doped $PbTe_{1-y}Se_y$ [30], I-doped $PbTe_{1-y}Se_y$ [51], Cl-doped $PbSe_{1-y}S_y$ [52], Cl-doped $PbTe_{1-x-y}Se_xS_y$ [53], Cl-doped $PbS_{1-y}Te_y$ [54], and In-doped $PbTe_{1-y}Se_y$ [55] withcold-side temperature 323 K.

In spite of high peak *ZT*s in I-doped $PbTe_{1-y}Se_y$ (~1.5 at about 600 K) [51], Cl-doped $PbSe_{1-y}S_y$ (~1.3 at about 900 K) [52], and Cl-doped $PbTe_{1-x-y}Se_xS_y$ (~1.1 at about 800 K) [53], (Figure 5.3.7 (a)), $(ZT)_{eng}$ (Figure 5.3.7 (b)) and the efficiency (Figure 5.3.7 (c)) of both $Cr_{0.01}Pb_{0.99}Te_{0.25}Se_{0.75}$ (previous work with high $(ZT)_{eng}$) [30] and $In_{0.02}Pb_{0.98}Te_{0.8}S_{0.2}$ are higher than others with T_h up to 773 K. It clearly shows that increase of $(ZT)_{eng}$ is more important than achieving high peak *ZT*. An engineering figure of merit, $(ZT)_{eng}$ of ~ 0.7 and the efficiency of ~ 12% can be achieved in $Pb_{0.98}In_{0.02}Te_{0.8}S_{0.2}$ with T_h at 773 K and T_c at 323 K.

5.4. Conclusion

PbS was incorporated into In-doped PbTe to increase the electrical conductivity by band modification and to decrease the thermal conductivity by alloy scattering and spinodal decomposition. With high room-temperature *ZT* optimized by deep lying doping, desirable average *ZT* and $(ZT)_{eng}$ are achieved in $In_{0.02}Pb_{0.98}Te_{0.8}S_{0.2}$, leading to an efficiency of ~12% withcold-side at 323 K and hot-side at 773 K. In-doped $PbTe_{1-y}S_y$ has high $(ZT)_{eng}$ due to the deep lying doping to achieve optimal carrier concentration for good room temperature *ZT*. This method could be applied to other material systems for higher TE efficiencies.

References

[1] G. J. Snyder and E. S. Tobber, *Nature Mater.* **7,** 105, (2008).

[2] Y. I. Ravich, B. A. Efimova and I. A. Smirnov, *Semiconducting Lead Chalcogenides*; Plenum, (1970).

[3] Q. Zhang, F. Cao, K. Lucas, W. S. Liu, K. Esfarjani, C. Opeil, D. Broido, D. Parker, D. J. Singh, G. Chen and Z. F. Ren, *J. Am. Chem. Soc.*, **134**, 17731, (2012).

[4] Y. Z. Pei, Z. M. Gibbs, A. Gloskovskii, B. Balke, W. G. Zeier and G. J. Snyder, *Adv. Energy Mater*., **4**, 1400486, (2014).

[5] J. P. Heremans, V. Jovovic, E. S. Toberer, A. Saramat, K. Kurosaki, A. Charoenphakdee, S. Yamanaka and G. J. Snyder, *Science*, **321**, 554, (2008).

[6] C. M. Jaworski, B. Wiendlocha, V. Jovovic and J. P. Heremans, *Energy Environ. Sci.*, **4**, 4155, (2011).

[7] Q. Y. Zhang, H. Wang, W. S. Liu, H. Z. Wang, B. Yu, Q. Zhang, Z. T. Tian, G. Ni, S. Lee, K. Esfarjani, G. Chen and Z. F. Ren, *Energy Environ. Sci.*, **5**, 5246, (2012).

[8] Q. Zhang, B. L. Liao, Y. C. Lan, K. Lukas, W. S. Liu, K. Esfarjani, C. Opeil, D. Broido, G. Chen and Z. F. Ren, *Proc. Natl. Acad. Sci. USA.*, **110**, 13261, (2013).

[9] Y. Z. Pei, X. Y. Shi, A. LaLonde, H. Wang, L. D. Chen and G. J. Snyder, *Nature*, **473**, 66, (2011).

[10] Q. Zhang, F. Cao, W. S. Liu, K. Lukas, B. Yu, S. Chen, C. Opeil, G. Chen and Z. F. Ren, *J. Am. Chem. Soc.*, **134**, 10031, (2012).

[11] X. H. Liu, T. J. Zhu, H. Wang, L. P. Hu, H. H. Xie, G. Y. Jiang, G. J. Snyder and X. B. Zhao, *Adv. Energy Mater*., **3**, 1238, (2013).

[12] H. Wang, Y. Z. Pei, A. D. LaLonde and G. J. Snyder, *Proc. Natl. Acad. Sci. USA.*, **109**, 9705, (2012).

[13] M. Zebarjadi, G. Joshi, G. H. Zhu, B. Yu, A. Minnich, Y. C. Lan, X. W. Wang, M. Dresselhaus, Z. F. Ren and G. Chen, *Nano Lett.*, **11**, 2225, (2011).

[14] B. Yu, M. Zebarjadi, H. Wang, K. Lukas, H. Z. Wang, D. Z. Wang, C. Opeil, M. Dresselhaus, G. Chen and Z. F. Ren, *Nano Lett.*, **12**, 2077, (2012).

[15] B. C. Sales, D. Mandrus and R. K. Williams, *Science*, **272**, 1325, (1996).

[16] K. F. Hsu, S. Loo, F. Guo, W. Chen, J. S. Dyck, C. Uher, T. Hogan, E. K. Polychroniadis and M. G. Kanatzidis, *Science*, **303**, 818, (2004).

[17] L. D. Zhao, S. H. Lo, Y. S. Zhang, H. Sun, G. J. Tan, C. Uher, C. Wolverton, V. P. Dravid and M. G. Kanatzidis, *Nature*, **508**, 373, (2014).

[18] Q. Zhang, E. K. Chere, J. Y. Sun, F. Cao, K. Dahal, S. Chen, G. Chen and Z. F. Ren, *Adv. Energy Mater*., **5**, 1500360, (2015).

[19] B. Poudel, Q. Hao, Y. Ma, Y. C. Lan, A. Minnich, B. Yu, X. Yan, D. Z. Wang, A. Muto, D. Vashaee, X. Chen, J. Liu, D. S. Dresselhaus, G. Chen and Z. F. Ren, *Science*, **634**, 2008320, (2008).

[20] R. J. Mehta, Y. Zhang, C. Karthik, B. Singh, R. W. Siegel, T. Borca-Tasciuc and

G. Ramanath, *Nat. Mater.*, **11**, 233, (2012).
[21] O. Delaire, J. Ma, K. Marty, A. F. May, M. A. McGuire, M-H. Du, D. J. Singh, A. Podlesnyak, G. Ehlers, M. D. Lumsden and B. C. Sales, *Nat. Mater.*, **10**, 614, (2011).
[22] S. Lee, K. Esfarjani, T. F. Luo, J. W. Zhou, Z. T. Tian and G. Chen, *Nat. Commun.*, **5**, 3525, (2014).
[23] K. Biswas, J. Q. He, I. D. Blum, C. I. Wu, T. P. Hogan, D. N. Seldman, V. P. Dravid and M. G. Kanatzidis, *Nature*, **489,** 414, (2012).
[24] H. J. Wu, L. D. Zhao, F. S. Zheng, D. Wu, Y. L. Pei, X. Tong, M. G. Kanatizidis and J. Q. He, *Nat. Commun*., **5**, 4515, (2014).
[25] D. Wu, *et al*., *Energy Environ. Sci.* DOI: 10.1039/C5EE01147G.
[26] Y. Lee, S-H. Lo, C. Q. Chen, H. Sun, D-Y. Chung, T. C. Chasapis, C. Uher, V. P. Dravid and M. G. Kanatzidis, *Nat. Commun.*, **5**, 3640, (2014).
[27] Y. Z. Pei, A. H. Nicholas, A. LaLonde and G. J. Snyder, *Energy Environ. Sci.*, **4**, 3640, (2011).
[28] Y. Z. Pei, A. D. LaLonde, N. A. Heinz, X. Y. Shi, S. Iwanaga, H. Wang, L. D. Chen and G. J. Snyder, *Adv. Mater.*, **23**, 5674, (2011).
[29] Q. Zhang, E. K. Chere, K. McEnaney, M. L. Yao, F. Cao, Y. Z. Ni, S. Chen, C. Opeil, G. Chen and Z. F. Ren, *Adv. Energy Mater*., **5**, 1401977, (2015).
[30] E. K. Chere, Q. Zhang, K. McEnaney, M. L. Yao, F. Cao, C. Opeil, G. Chen and Z. F. Ren, *Nano Energy*, **13**, 355, (2015).
[31] K. Weiser, *Phys. Rev. B*, **23**, 2741, (1981).
[32] B. A. Volkov, L. I. Ryabova and D. R. Khokhlov, *Phys. Usp.*, **45**, 819, (2002).
[33] Y. Gelbstein, Z. Dashevsky and M. P. Dariel, *Physica B*, **363**, 196, (2005).
[34] S. Ahmad, K. Hoang and S. D. Mahanti, *Phys. Rev. Lett.*, **96**, 056403, (2006).
[35] K. Hoang, S. D. Mahanti and P. Jena, *Phys. Rev. B*, **76**, 115432, (2007).
[36] S. Ahmad, S. D. Mahanti, K. Hoang and M. G. Kanatzidis, *Phys. Rev. B*, **74**, 155205, (2006).
[37] V. Jovovic, S. J. Thiagarajan, J. P. Heremans, T. Komissarova, D. Khokhlov and A. Nicorici, *J. Appl. Phys.*, **103**, 053710, (2008).
[38] Z. T. Tian, J. Garg, K. Esfarjani, T. Shiga, J. Shiomi and G. Chen, *Phys. Rev. B*, **85**, 184303, (2012).
[39] H. Wang, A. D. LaLonde, Y. Z. Pei and G. J. Snyder, *Adv. Funct. Mater.*, **23**, 1586, (2013).
[40] J. Q. He, L. D. Zhao, J. C. Zheng, J. W. Doak, H. J. Wu, H. Q. Wang, Y. Lee, C. Wolverton, M. G. Kanatzidis and V. P. Dravid, *J. Am. Chem. Soc.*, **135**, 4624, (2013).
[41] L. P. Hu, T. J. Zhu, X. H. Liu and X. B. Zhao *Adv. Funct. Mater*., **24**, 5211, (2014).
[42] J. Androulakis, C. H. Lin, H. J. Kong, C. Uher, C. I. Wu, T. Hogan, B. A. Cook, T. Caillat, K. M. Paraskevopoulos and M. G. Kanatzidis, *J. Am. Chem. Soc.*, **129**, 9780, (2007).
[43] Q. Zhang, X. B. Zhao, T. J. Zhu and J. P. Tu, *Phys. Stat. Sol. (RRL)*, **2**, 56, (2008).

[44]H. Lin, E. S. Bozin, S. J. L. Billinge, J. Androulakis, C. D. Malliakas, C. H. Lin and M. G. Kanatzidis, *Phys. Rev. B*, **80**, 045204, (2009).
[45] S. N. Girard, K. Schmidt-Rohr, T. C. Chasapis, E. Hatzikraniotis, B. Njegic, E. M. Levin, A. Rawal, K. M. Paraskevopoulos and M. G. Kanatzidis, *Adv. Funct. Mater.*, **23**, 747, (2013).
[46] A. D. LaLonde, Y. Z. Pei and G. J. Snyder, *Energy Environ. Sci.*, **4**, 2090, (2011).
[47] H. Wang, E. Schechtel, Y. Z. Pei and G. J. Snyder, *Adv. Energy Mater.*, **3**, 48, (2013).
[48] L. D. Zhao, S. H. Lo, J. Q. He, H. Li, K. Biswas, J. Androulakis, C. Wu, T. P. Hogan, D. Y. Chung, V. P. Dravid and M. G. Kanatzidis, *J. Am. Chem. Soc.*, **133**, 20476, (2011).
[49] L. D. Zhao, J. Q. He, C. Wu, T. P. Hogan, X. Y. Zhou, C. Uher, V. P. Dravid and M. G. Kanatzidis, *J. Am. Chem. Soc.*, **134**, 7902, (2012).
[50] Y. V. Maltsev, E. D. Nensberg, A. V. Petrov, Semileto.Sa and Y. I. Ukhanov, *Sov. Phys. Solid State*, **8**, 1713, (1967).
[51] P. K. Rawat, B. Paul and P. Banerji, *Nanotechnology*, **24**, 215401, (2013).
[52] J. Androulakis, I. Todorov, J. Q. He, D. Y. Chung, V. Dravid and M. Kanatzidis, *J. Am. Chem. Soc.*, **133**, 10920, (2011).
[53] S. A. Yamini, H. Wang, D. Ginting, D. R. G. Mitchell, S. X. Dou and G. J. Snyder, *ACS Appl. Mater. Interfaces*, **6**, 11476, (2014).
[54] S. Johnsen, J. Q. He, J. Androulakis, V. P. Dravid, I. Todorov, D. Y. Chung, and M. G. Kanatzidis, *J. Am. Chem. Soc.*, **133**, 3460, (2011).
[55] A. Bali, H. Wang, G. J. Snyder and R. C. Mallik, *J Appl. Phys.*, **116**, 033707, (2014).
[56] H. S. Kim, W. S. Liu, G. Chen, C. W. Chu and Z. F. Ren, *Proc. Natl. Acad. Sci. USA.*, **112**, 8209, (2015).

CHAPTER 6: I-DOPED N-TYPE TIN SELENIDE

6.1. Introduction

Explorations of different materials, ranging from metals to alloys and from single crystals to nanostructures lead to high performance thermoelectric materials overtime [1-11]. As we have seen in the last three chapters, the various thermal and electrical transport property optimization techniques, such as resonant doping [12,13], band convergence [14,15], all-scale hierarchical structuring [16,17] etc., have been effective in improving the performance of group IV–VI semiconductors especially lead chalcogenides. These optimizations lead to achieving peak *ZT* values as high as ~2 in different lead chalcogenide alloys [16,18,19]. In spite of decent thermoelectric figure of merit in lead chalcogenide compounds, the issue of toxicity has always been a concern. This inspired to the investigation of lead-free compounds such as; tin chalcogenides [20–31]. All tin chalcogenides (SnTe, SnSe, and SnS) were proved to be topological insulators [32–34] and rarely studied for thermoelectric applications. It has been reported that p-type In-doped SnTe has *ZT* value higher than ~1 [20]. Recently, a highest *ZT* value of ~ 2.6 at 923 K reported in p-type single crystalline SnSe along one of its crystallographic direction [23]. This material was not studied as thermoelectric material due to its large band gap ~ 0.9 eV [35–39]. The high *ZT* is solely attributed to the intrinsically ultralow thermal conductivity due to high anharmonicity of the chemical bonds [23,40,41]. Considering the large-scale applications and the poor mechanical properties in the layered single crystal SnSe (crystallized in the orthorhombic Pnma space group), SnSe polycrystals were then studied [26]. However, due to lower electrical conductivity and

higher thermal conductivity, the peak *ZT* value was significantly decreased to lower than 1 at about 800 K [26]. Many kinds of p-type dopants were tested to increase the carrier concentration and electrical conductivity, and best peak *ZT* of ≈ 0.6 at about 750 K was achieved in Ag-doped polycrystalline SnSe [27]. SnS (crystallized in orthorhombic Pbmn space group) has similar layered structure with SnSe and even larger band gap ~1.21 eV [35,36,38,39,42,43].

Potential application of this environmentally compatible and low-cost material was predicted by first principles calculation [44] and a *ZT* of ~ 0.6 at about 900 K was recently obtained in p-type Ag-doped polycrystalline SnS [29]. In this chapter, we will address the thermoelectric performance of anisotropic I-doped n-type SnSe and SnSe-SnS polycrystalline alloys.

6.2. Experimental Methods

N-type iodine doped polycrystalline SnSe, $SnSe_{0.9}S_{0.1}$, and $SnSe_{0.7}S_{0.3}$ were prepared by melting the raw materials (Sn granules, 99.9%; Se granules, 99.99%; S pieces, 99.999%; and SnI_2 beads, 99.99%) in the double sealed quartz tubes. The raw materials were slowly (100 ^oC/h) raised to 920 ^oC and kept for 6 h, then slowly (100 ^oC/h) cooled to 600 ^oC and stayed at that temperature for 70 h, finally slowly (100 ^oC/h) cooled to room temperature. The obtained ingots were cleaned and broken by a high-energy ball mill SPEX 8000D (SPEX Sample Prep.) for 1 min to get the powder. The powder was loaded into the half-inch die and hot pressed by alternating current (ac-HP) press at 600 ^oC for 7 min under 50 MPa to get a 14 mm pillar. Considering the anisotropy of SnSe and SnS, all the samples were cut from both parallel and perpendicular to the pressing direction and

measured along both directions. X-ray diffraction spectra analysis was conducted on a PANalytical multipurpose diffractometer with an X'celerator detector (PANalytical X'Pert Pro) from different directions of the anisotropic sample. The lattice parameters were calculated by the Rietveld refinement method. The microstructures were investigated by a scanning electron microscope (SEM, LEO 1525). The electrical resistivity (ρ) and Seebeck coefficient (S) were simultaneously obtained on a commercial system (ULVAC ZEM-3). The thermal conductivity κ was calculated using $\kappa = D\alpha C_p$, where D is volumetric density determined by the Archimedes method, α the thermal diffusivity obtained on a laser flash apparatus (Netzsch LFA 457) for an half inch disk with thickness of < 1.5 mm, and C_p the specific heat measured on a differential scanning calorimetry thermal analyzer (Netzsch DSC 404 C). The Hall Coefficient R_H at room temperature was measured using PPMS (Quantum Design Physical Properties Measurement System) with a magnetic field of -3 T and 3 T and an electrical current of 8 mA. The Hall carrier concentration n_H was calculated using $n_H = 1/(eR_H)$. The uncertainty for the electrical conductivity is 3%, the Seebeck coefficient 5%, the thermal conductivity 7% (comprising uncertainties of 4% for the thermal diffusivity, 5% for the specific heat, and 3% for the density), so the combined uncertainty for the power factor is 10% and that for *ZT* value is 12%. Error bars were not used in the Figures to increase the readability of the curves.

6.3. Thermoelectric Properties of n-type Polycrystalline $SnSe_{1-x}I_x$

SnSe crystallizes in a layered structure with orthorhombic Pnma space group (PDF #32-1382) at room temperature [29]. Figure 6.3.1 shows the XRD patterns taken in the plane

parallel to the hot pressing direction (a) and perpendicular to hot pressing direction (b). The calculated lattice parameters for undoped SnSe (a = 11.48, b = 4.15, and c = 4.43) are consistent with the reported data [23,26]. There is obvious difference in diffraction intensity in (400) and (111) planes (the ratio of the integral intensity of peak (400) to peak (111) is 0.47 in panel (a) and 2.2 in panel (b) for undoped SnSe). This indicates the existence of anisotropy in the samples in agreement with the microstructure shown in SEM image (Figure 6.3.2a). All the peaks were indexed without any impurity in spite of the high iodine concentration. A structural phase transition from orthorhombic low symmetric (Pnma) phase to orthorhombic high symmetric (Cmcm) phase undergoes at about 780 K [23,26,45]. This is confirmed from the temperature dependence of specific heat for $SnSe_{1-y}S_y$ (y = 0, 0.1, and 0.3) as shown in Figure 6.3.3. The phase transition temperature pushed to a higher temperature when SnSe is alloyed with SnS.

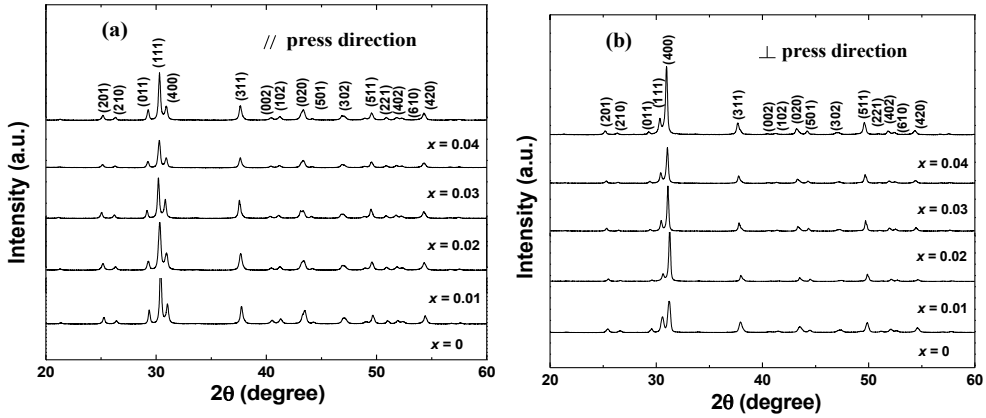

Figure 6.3.1 XRD patterns of $SnSe_{1-x}I_x$ (x = 0, 0.01, 0.02, 0.03, and 0.04) of bulk samples (a) parallel to the hot pressing direction and (b) perpendicular to the hot pressing direction.

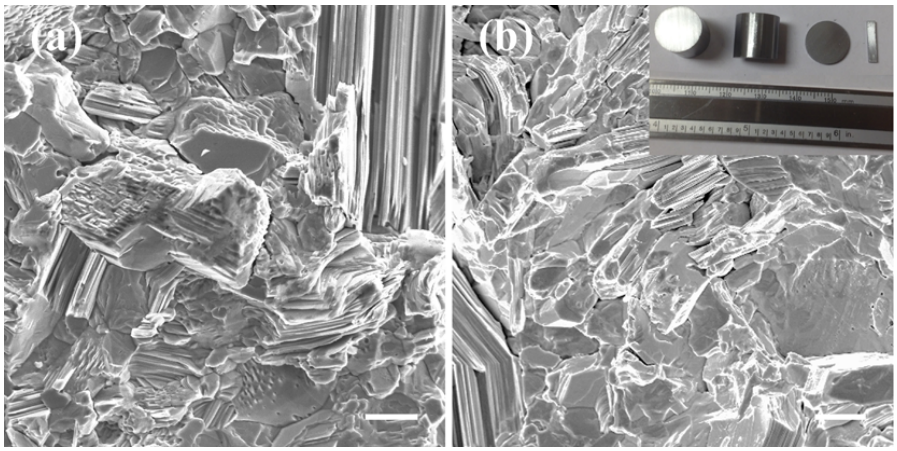

Figure 6.3.2 SEM fracture images of I-doped $SnSe_{0.97}I_{0.03}$ a) on bulk samples perpendicular to the hot pressing direction and I-doped $SnSe_{0.87}S_{0.1}I_{0.03}$ b) on bulk samples parallel to the hot pressing direction. The scale bar is 10 μm. Inset image: the hot pressed disk.

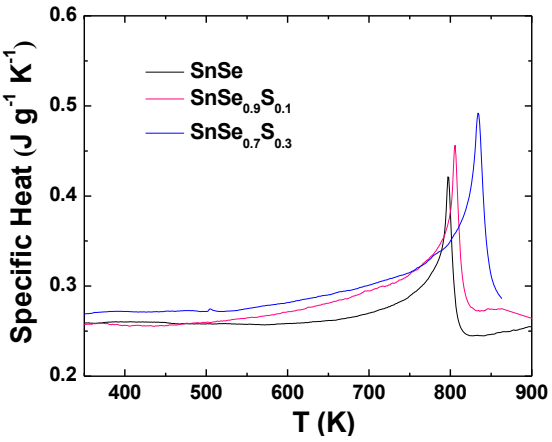

Figure 6.3.3 Temperature dependence of specific heat for $SnSe_{1-y}S_y$ (y = 0, 0.1, and 0.3). To be conservative, C_p of the undoped SnSe, $SnSe_{0.9}Se_{0.1}$, and $SnSe_{0.7}Se_{0.3}$ are used for the calculation of the total thermal conductivity of I-doped SnSe, $SnSe_{0.9}Se_{0.1}$, and $SnSe_{0.7}Se_{0.3}$, respectively. The small peak at about 500 K corresponds to the melting of maybe a very small amount of elemental Sn [26].

The electrical conductivity of single crystalline SnSe is much lower than that of traditional state-of-the-art thermoelectric materials. The very high *ZT* of single crystalline SnSe is attributed to the ultralow thermal conductivity due to the

intrinsically high anharmonicity of the chemical bonds [23,40]. Polycrystalline SnSe has even lower electrical conductivity compared to single crystal SnSe [26]. The Hall carrier concentration can be increased from ~ $2x10^{17}$ cm^{-3} to ~$9x10^{18}$ cm^{-3} by Ag doping [27]. However, the electrical conductivity is still low because of the lower carrier mobility in polycrystals. Figure 6.3.4 shows the temperature dependence of electrical conductivity (a), Seebeck coefficient (b), power factor (c), thermal diffusivity (d), total thermal conductivity (e), and *ZT* (f) of all doped $SnSe_{1-x}I_x$ (x = 0.01, 0.02, 0.03, and 0.04) compared with undoped SnSe measured along the hot pressing direction.

All the electrical conductivities increased with increasing temperature, showing typical semiconductor behavior. It has been reported that nominal stoichiometric SnSe shows p-type intrinsic behavior [27], like the undoped result shown in Figure 6.3.4. In our study, the real composition is found to be close to $SnSe_{0.86}$ with Se defect due to the evaporation of Se during melting and annealing (Table 6.3.1). However, Se evaporation is not observed after long time annealing (70 h). If added up to 5 atm. % of extra Se during preparation, the compound still shows p-type with negligible carrier density change and become n-type with 5 atm. % extra Sn (but not stable) [27]. In this study, iodine doping changed the conductivity type from p to n in the whole temperature range when $x \geq 0.01$ confirmed by both the measured Seebeck coefficients and Hall coefficients (Figure 6.3.5) (the sample is also not stable when x = 0.005, showing p-type at room temperature as shown in Figure 6.3.5 and n-type at higher temperature, not shown here). Both iodine doping and Sn overweight together

created electrons, but the electron carrier density is limited to only ~ $5x10^{15}$ cm^{-3} for $x = 0.01$ and to ~$2x10^{17}$ cm^{-3} for $x = 0.04$. The electrical conductivity decreased first ($x \leq 0.01$) then increased ($x \geq 0.01$) with increasing content of iodine, but the value is still as low as the undoped SnSe when $x = 0.04$. Thus, in spite of the high Seebeck coefficient, the power factor is only ~ 4 μW cm^{-1} K^{-2} at about 800 K.

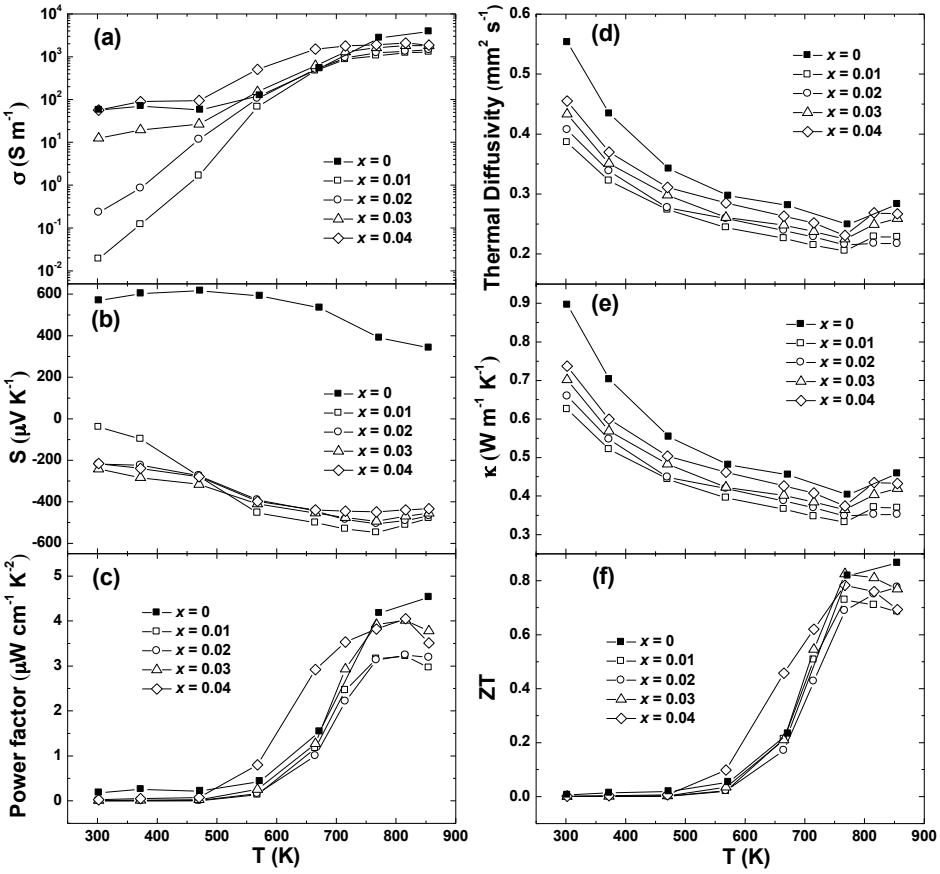

Figure 6.3.4 Temperature dependence of (a) electrical conductivity, (b) Seebeck coefficient, (c) power factor, (d) thermal diffusivity, (e) total thermal conductivity and (f) *ZT* for $SnSe_{1-x}I_x$ (x = 0, 0.01, 0.02, 0.03, and 0.04) measured along the hot pressing direction.

Table 6.3.1 Room-temperature real composition, density, Hall carrier concentration, electrical conductivity, and total thermal conductivity for $SnSe_{1-x}I_x$ and $SnSe_{0.97-y}S_yI_{0.03}$.

Nominal Comp.	Real Comp.	Density ($g\ cm^{-3}$)	n_H ($10^{17}\ cm^{-3}$)	σ ($S\ m^{-1}$)	κ ($W\ m^{-1}\ K^{-1}$)
SnSe	$SnSe_{0.86}$	6.05	2.3	56.5	0.90
$SnSe_{0.995}I_{0.005}$	$SnSe_{0.891}I_{0.006}$	5.90	1.6	0.22	0.65
$SnSe_{0.99}I_{0.01}$	$SnSe_{0.883}I_{0.013}$	5.87	0.05	0.02	0.63
$SnSe_{0.98}I_{0.02}$	$SnSe_{0.856}I_{0.021}$	5.84	0.15	0.23	0.66
$SnSe_{0.97}I_{0.03}$	$SnSe_{0.884}I_{0.034}$	5.81	0.46	12.5	0.70
$SnSe_{0.96}I_{0.04}$	$SnSe_{0.873}I_{0.04}$	5.80	2.4	56.8	0.74
$SnSe_{0.87}S_{0.1}I_{0.03}$	$SnSe_{0.88}S_{0.07}I_{0.04}$	5.75	0.38	15.8	0.72
$SnSe_{0.67}S_{0.3}I_{0.03}$	$SnSe_{0.68}S_{0.29}I_{0.03}$	5.61	0.25	7.19	0.49

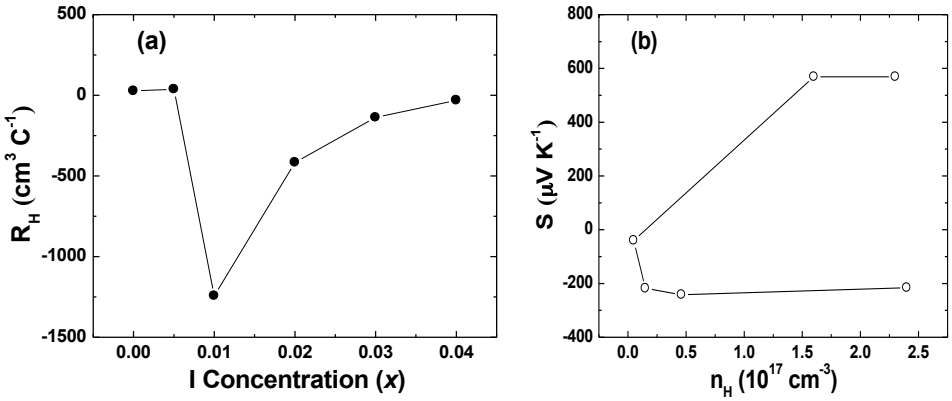

Figure 6.3.5 Relationship between room-temperature Hall coefficient (R_H) and iodine concentration (x) (a) and room temperature Pisarenko relation for $SnSe_{1-x}I_x$ (x = 0, 0.005, 0.01, 0.02, 0.03, and 0.04) (b).

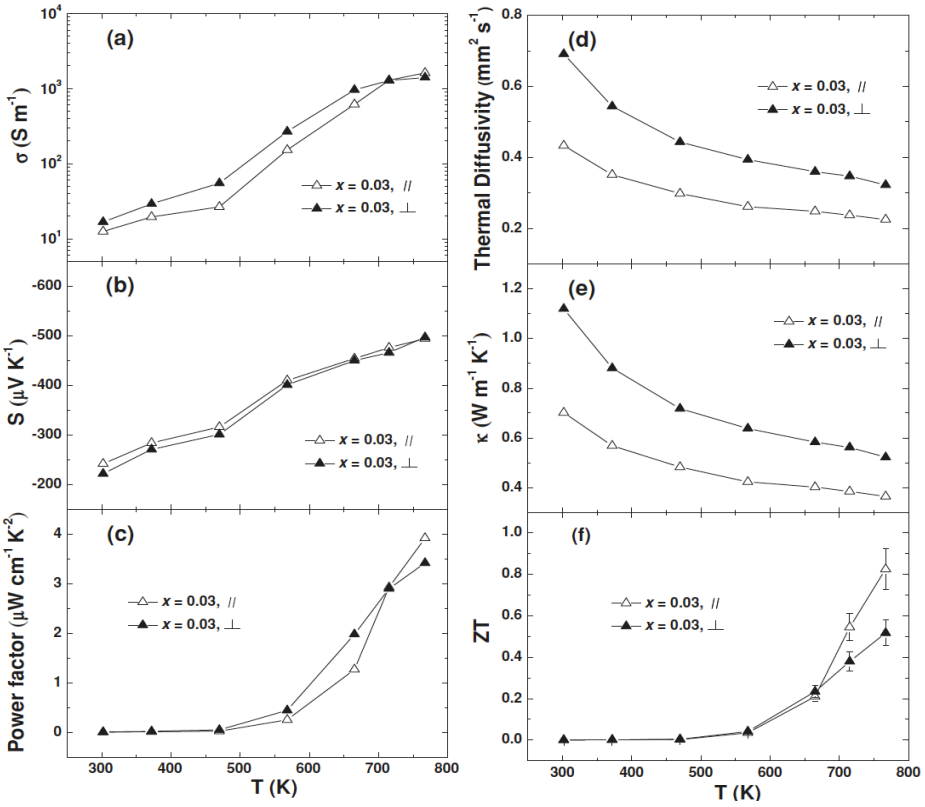

Figure 6.3.6 Temperature dependence of a) electrical conductivity, b) Seebeck coefficient, c) power factor, d) thermal diffusivity, e) total thermal conductivity, and f) ZT for $SnSe_{0.97}$ $I_{0.03}$ measured along the hot pressing direction (open symbols) and perpendicular to the hot pressing direction (filled symbols).

Normally, Seebeck coefficient decreased with increasing carrier concentration. However, from the Pisarenko relation for $SnSe_{1-x}I_x$ in Figure 6.3.5 b, the negative Seebeck coefficient increased with increasing electron carrier concentration when $x < 0.03$ due to the relatively high density of minority carriers when having too low electron carrier concentration. The high density of minority carriers decreased the Seebeck coefficient at low electron carrier concentration. Considering the low electronic thermal conductivity ($\kappa_e = L\sigma T$, where L is the Lorenz number), the lattice thermal conductivity ($\kappa_L = \kappa_{total} - \kappa_e$) is close to the total thermal conductivity shown in Figure 6.3.4 e. Similar to other

reported SnSe [23,26,27], high *ZT* value of ~ 0.8 at about 773 K as shown in Figure 6.3.4 f is mostly benefited from this very low intrinsic thermal conductivity. We also showed the thermoelectric properties of $SnSe_{0.97}I_{0.03}$ measured both parallel and perpendicular to the hot pressing direction in Figure 6.3.6. The electrical conductivity and the thermal conductivity measured from perpendicular to the hot pressing direction are higher than those from parallel to the hot pressing direction, but the Seebeck coefficient is almost the same from the two directions. However, the *ZT* is higher along the hot pressing direction. SnS also crystallizes in a layered structure with orthorhombic Pbmn space group (PDF #39-0354) at room temperature [29]. It undergoes structural phase transition from orthorhombic to tetragonal at about 858 K [29]. We also studied the alloying effect of SnS into SnSe to see whether further reduction on thermal conductivity is possible. Figure 6.3.7 shows the XRD patterns of alloyed bulk samples $SnSe_{0.97-y}S_yI_{0.03}$ (y = 0, 0.1, and 0.3) parallel (a) and perpendicular (b) to hot pressing direction. Again, we saw strong anisotropy in the samples, which is in consistent with the SEM images presented in Figure 6.3.2 b. Since SnSe and SnS can form a continuous series of solid solutions, all the peaks of $SnSe_{0.97-y}S_yI_{0.03}$ were indexed to single phase with a minor right shift when SnS is increased. All the calculated lattice parameters (a, b, and c) decreased with increasing concentration of SnS in consistent with Vegard's law.

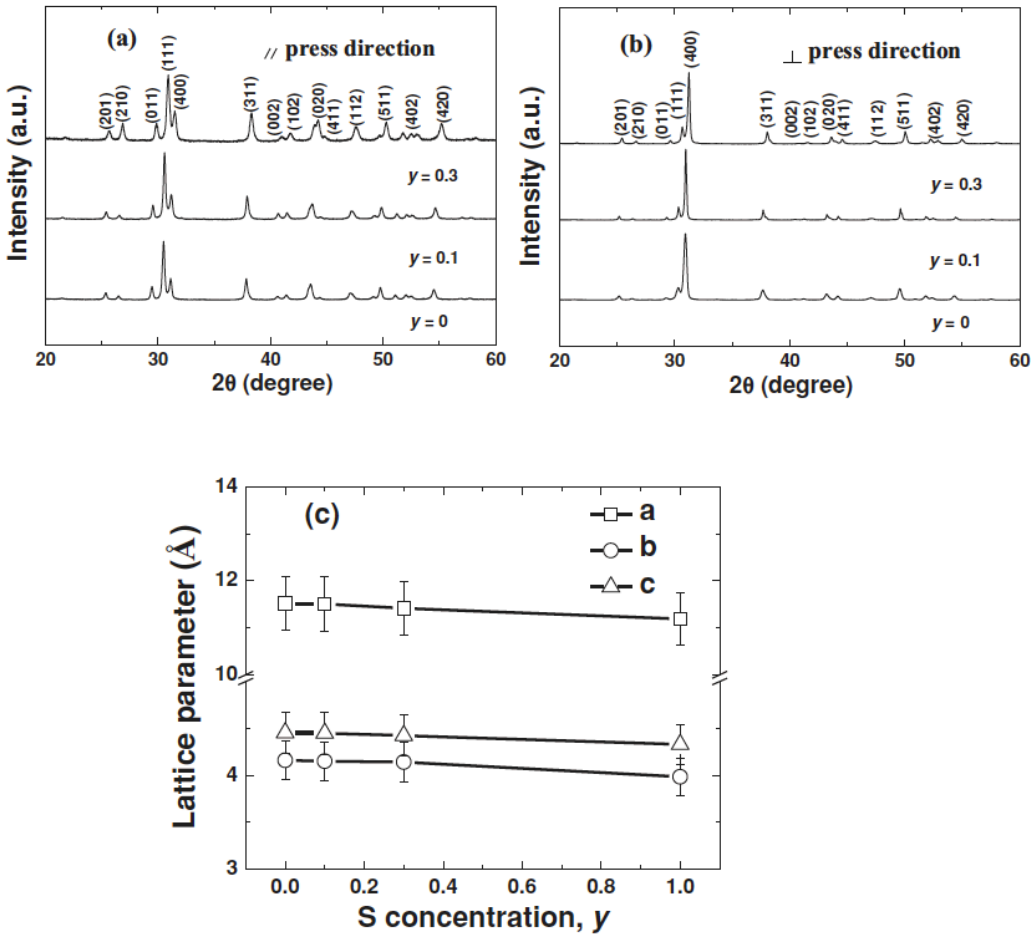

Figure 6.3.7 XRD patterns of bulk samples $SnSe_{0.97-y}S_yI_{0.03}$ (y = 0, 0.1, and 0.3) a) along the hot-pressing direction and b) perpendicular to the hot pressing direction. The calculated lattice parameters were based on $SnSe_{0.97-y}S_yI_{0.03}$ (y = 0, 0.1, and 0.3). We use data from ref [29] for undoped SnSe.

Figure 6.3.8 presents the temperature dependence of electrical conductivity (a), Seebeck coefficient (b), power factor (c), thermal diffusivity (d), total thermal conductivity (e), and ZT (f) of alloyed $SnSe_{0.97-y}S_yI_{0.03}$ (y = 0.1 and 0.3) compared with $SnSe_{0.97}I_{0.03}$ measured from along the hot pressing direction. Both the electrical conductivity and the thermal conductivity decreased with increasing content of SnS. Se evaporation was depressed and the electron carrier concentration decreased by introducing S (see Table 6.3.1). Optical absorption spectra in Figure 6.3.9 shows that the band gap of undoped SnSe is ~ 0.94 eV, which is decreased to ~ 0.91 eV for $SnSe_{0.97}I_{0.03}$ by I doping and

increased to ~0.97 eV for $SnSe_{0.67}S_{0.3}I_{0.03}$ and ~ 0.93 eV for $SnSe_{0.87}S_{0.1}I_{0.03}$ by alloying with SnS.

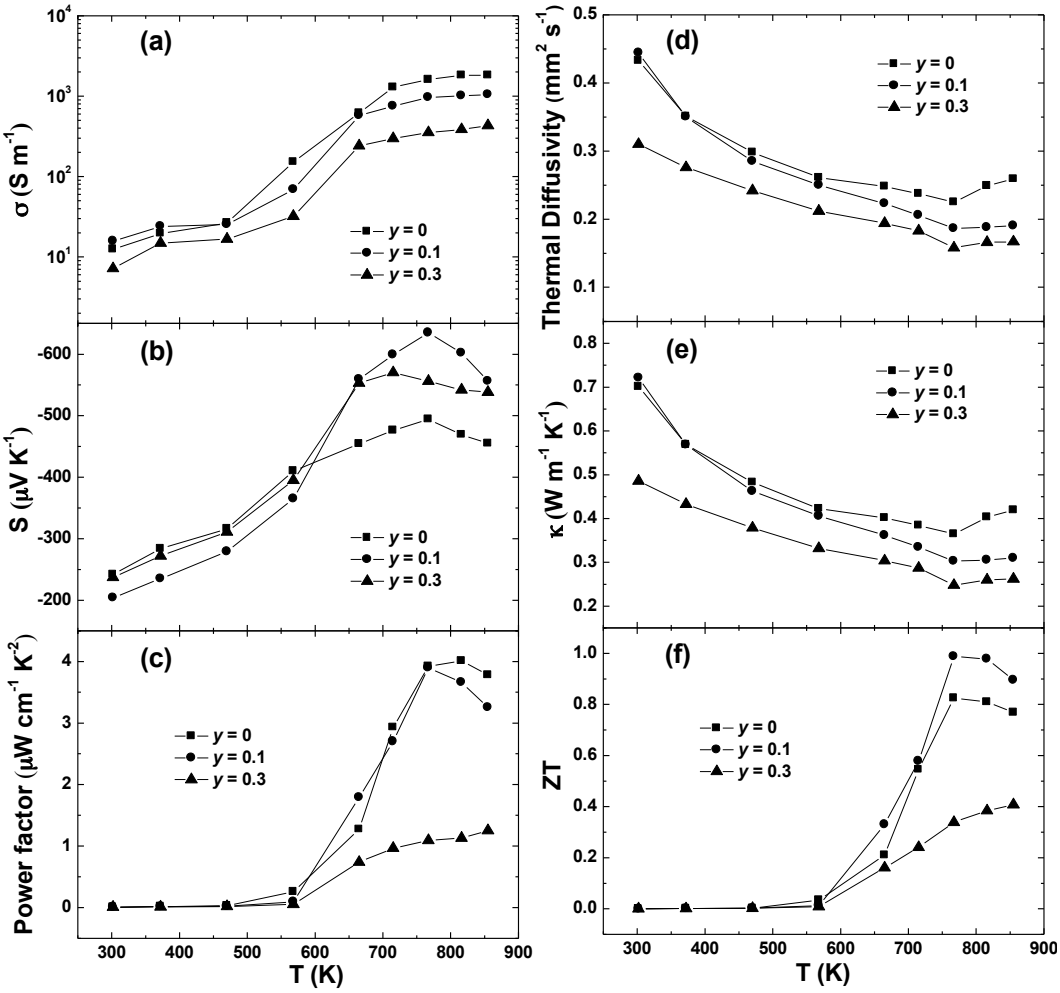

Figure 6.3.8 Temperature dependence of (a) electrical conductivity, (b) Seebeck coefficient, (c) power factor, (d) thermal diffusivity, (e) total thermal conductivity, and (f) *ZT* for $SnSe_{0.97-y}S_yI_{0.03}$ (y = 0, 0.1, and 0.3) measured along the hot-pressing direction.

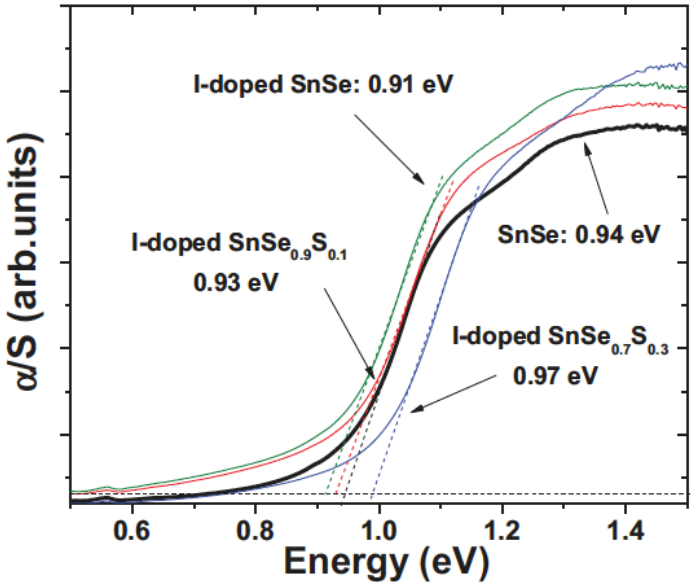

Figure 6.3.9 Optical absorption spectra and band gaps for undoped SnSe (black line), $SnSe_{0.97}I_{0.03}$ (green line), $SnSe_{0.87}S_{0.1}I_{0.03}$ (red line), and $SnSe_{0.67}S_{0.3}I_{0.03}$ (blue line).

According to the Debye approximation, the theoretical lowest lattice thermal conductivity of a disordered crystal can be calculated using the following formula [33].

$$k_{\min} = \left(\frac{\pi}{6}\right)^{1/3} \kappa_B n^{2/3} \sum_i v_i \left(\frac{T}{\theta_i}\right)^2 \int_0^{\theta_i/T} \frac{x^3 e^x}{\left(e^x - 1\right)^2} dx \qquad (6.3.1)$$

Where κ_B is the Boltzmann constant, n is number of atom per volume; v_i and Θ_i are the phonon velocity and Debye temperature for three sound modes (two transverse and one longitudinal), respectively. In our case, the calculated lowest lattice thermal conductivity is ~0.26 W m^{-1} K^{-1} at about 770 K for the low temperature orthorhombic (Pnma) phase SnSe, which is still lower than the experimental results for undoped (~0.4 W m^{-1} K^{-1}) and I-doped SnSe, ($SnSe_{0.97}I_{0.03}$ ~0.37 W m^{-1} K^{-1}) at 770 K shown in Figure 6.3.4 e. In spite of the very low thermal conductivity in SnSe, we also tried alloying with SnS in 3 atm. % iodine-doped SnSe to further decrease the thermal conductivity. Due to the very

low electrical conductivity, the lattice thermal conductivity is also close to the total thermal conductivity. It also decreased close to the theoretical limit with more alloy scattering (≈ 0.3 W m^{-1} K^{-1} for $SnSe_{0.87}S_{0.1}I_{0.03}$, and ≈ 0.25 W m^{-1} K^{-1} for $SnSe_{0.67}S_{0.3}I_{0.03}$ at 770 K) (if more SnS alloyed, we should consider the theoretical limit of the $SnSe_{1-y}S_y$ alloys). This thermal conductivity is also close to the lattice thermal conductivity of the single crystals measured from b axis and c axis from 673 K-773 K [23]. The increased Seebeck coefficient by alloying, together with the lowered thermal conductivity kept the power factor at ~ 4 μW cm^{-1} K^{-2} and increased the highest *ZT* to ~ 1.0 at about 773 K for $SnSe_{0.87}S_{0.1}I_{0.03}$. This finding shows the first n-type Sn chalcogenide alloy also with decent peak *ZT*. However, we must notice the low average *ZT* of tin chalcogenides, even worse than that of lead chalcogenides.

6.4. Conclusion

I-doped n-type SnSe polycrystal was successfully prepared by melting and hot pressing. The electrons from iodine doping first decreased the carrier concentration and then increased the electron carrier concentration to ~ $2x10^{17}$ cm^{-3} in $SnSe_{0.96}I_{0.04}$. *ZT* of ~ 0.8 at about 773 K was obtained due to the intrinsic ultralow thermal conductivity in $SnSe_{0.97}I_{0.03}$. A highest *ZT* of ~ 1.0 at about 773 K was achieved by alloying 10 atm. % SnS with 3 atm. % I-doping due to even lower thermal conductivity. Although having high peak *ZT*s in p-type single crystalline SnSe, the *ZT* of its polycrystalline form is not quite promising. In order to use this environmentally friendly and economic material, the average *ZT* needs to be increased.

References

[1] D. M. Rowe, *CRC Handbook of Thermoelectrics: Macro to nano*; CRC Press, Taylor & Francis, Boca Raton, (2006).

[2] M. S. Dresselhaus, G. Chen, M. Y. Tang, R. G. Yang, H. Lee, D. Z. Wang, Z. F. Ren, J. P. Fleurial and P. Gogna, *Adv. Mater.*, **19**, 1043, (2007).

[3] B. Poudel, Q. Hao, Y. Ma, Y. C. Lan, A. Minnich, B. Yu, X. Yan, D. Z. Wang, A. Muto, D. Vashaee, X. Chen, J. Liu, D. S. Dresselhaus, G. Chen and Z. F. Ren, *Science*, **320**, 634, (2008).

[4] J. P. Heremans, V. Jovovic, E. S.Toberer, A. Samarat, K. Kurosaki, A. Charoenphakdee, S. Yamanaka and G. J. Snyder, *Science*, **321**, 554, (2008).

[5] Q. Y. Zhang, H. Wang, W. S. Liu, H. Z. Wang, B. Yu, Q. Zhang, Z. T. Tian, G. Ni, S. Lee, K. Esfarjani, G. Chen and Z. F. Ren, *Energy Environ. Sci.*, **5**, 5246, (2012).

[6] Y. Z. Pei, X. Y. Shi, A. LaLonde, H. Wang, L. D. Chen and G. J. Snyder, *Nature*, **473**, 66, *(*2011).

[7] Q. Zhang, F. Cao, W. S. Liu, K. Lukas, B. Yu, S. Chen, C. Opeil, G. Chen and Z. F. Ren, *J. Am. Chem, Soc*, 134**,** 10031, (2012).

[8] K. Biswas, J. Q. He, I. D. Blum, C. I. Wu, T. P. Hogan, D. N. Seldman, V. P. Dravid and M. G. Kanatzidis, *Nature*, **489**, 414, (2012).

[9] Y. Lee, S. H. Lo, J. Androulakis, C. I. Wu, L. D. Zhao, D. Y. Chung, T. P. Hogan, V. P. Dravid, M. G. Kanatizidis, *J. Am. Chem, Soc*, 135, 5152, (2013).

[10] R. J. Korkosz, T. C. Chasapis, S. H. Lo, J. W. Doak, Y. J. Kim, C. I. Wu, E. Hatzikraniotis, T. P. Hogan, D. N. Seidman, C. Wolverton, V. P. Dravid and M. G. Kanatzidis, *J. Am. Chem. Soc.*, **136**, 3225, (2014).

[11] H. J. Wu, L. D. Zhao, F. S. Zheng, D. Wu, Y. L. Pei, X. Tong, M. G. Kanatizidis and J. Q. He,*Nat. Commun*., **5**, 4515, (2014).

[12] Q. Zhang, B. L. Liao, Y. C. Lan, K. Lukas, W. S. Liu, K. Esfarjani, C. Opeil, D. Broido, G. Chen and Z. F. Ren, *Proc. Natl. Acad. Sci. USA.*, **110**, 13261, (2013).

[13] G. J. Tan, L. D. Zhao, F. Y. Shi, J. W. Doak, S. H. Lo, H. Sun, C. Wolverton, V. P. Dravid, C. Uher and M. G. Kanatzidis, *J. Am. Chem. Soc.*, **136**, 7006, (2014).

[14] M. Zhou, Z. M.Gibbs, H. Wang, Y. Han, C. N. Xin, L. F. Li and G. J. Snyder, *Phys. Chem. Chem. Phys.*, DOI: 10.1039/c4cp02091j, (2014).

[15] L. D. Zhao, S. H. Lo, Y. S. Zhang, H. Sun, G. J. Tan, C. Uher, C. Wolverton, V. P. Dravid and M. G. Kanatzidis, *Nature*, **508**, 373, (2014).

[16] J. P. Heremans, *Nature*, **508**, 327, (2014).

[17] H. Zhang and D. V. Talapin, *Angew. Chem. Int. Ed.*, **53**, 9126, (2014).

[18] S. Sassi, C. Candolfi, J. B. Vaney, V. Ohorodniichuk, P. Masschelein, A. Dauscher and B. Lenori, *Appl. Phys. Lett.*, **104**, 212105, (2014).

[19] C. L. Chen, H. Wang, Y. Y. Chen, T. Day and G. J. Snyder, *J. Mater. Chem. A*, **2**, 11171, (2014).

[20] E. K. Chere, Q. Zhang, K. Dahal, F. Cao, G. Chen and Z. F. Ren, *Adv. Energy Mater.* Submitted.

[21] A. Banik and K. *J. Biswas, Mater. Chem. A*, **2**, 9620, (2014).
[22] Q. Tan, L. D. Zhao, J. F. Li, C. F. Wu, T. R. Wei, Z. B. Xing and M. G. Kanatzidis, *J Mater. Chem. A*, **2**, 17302, (2014).
[23] W. Albers, C. Haas, H. Ober, G. R. Schodder and J. D. Wasscher, *J. Phys. Chem. Solids*, **23**, 215, (1962).
[24] J. D. Wasscher, W. Albers and C. Haas, *Solid-State Electron.*, **6**, 261, (1963).
[25] J. G. Yu, A. S. Yue and O. M. Stafsudd, *J. Cryst. Growth*, **54**, 248, (1981).
[26] M. Parenteau and C. Carlone, *Phys. Rev. B*, **41**, 5227, (1990).
[27] B. B. Nariya, A. K. Dasadia, M. K. Bhayani, A. J. Patel and A. R. Jani, *Chalcogenide Lett.*, **6**, 549, (2009).
[28] G. J. Snyder and E. S. Toberer, *Nature Mater.*, **7**, 105, (2008).
[29] W. Albers, C. Haas, H. J. Vink and J. D. Wasscher, *J Appl. Phys.*, **32**, 2220, (1961).
[30] M. M. Nassary *J Alloy Comp.*, **398**, 21, (2005).
[31] C. Bera, S. Jacob, I. Opahle, N. S. H. Gunda, R. Chmielowski, G. Dennler and G. K. H. Madsen, *Phys. Chem. Chem. Phys.*, **16**, 19894, (2014).
[32] T. Chattopadhyay, J. Pannetier and H. G. Vonschnering, *J. Phys. Chem. Solids*, **47**, 879, (1986).
[33] D. G. Cahill, S. K.Watson and R. O. Pohl, *Phys. Rev. B*, **46**, 6131, (1992).
[34] Y. Z. Pei, A. LaLonde, S. Iwanaga and G. J. Snyder, *Energy Environ. Sci.*, **4**, 2085, (2011).
[35] H. Wang, Y. Z. Pei, A. D. LaLonde and G. J. Snyder, *Adv. Mater.*, **23**, 1366, (2011).
[36] A. D. LaLonde, Y. Z. Pei and G. J. Snyder, *Energy Environ. Sci.*, **4**, 2090, (2011).
[37] Q. Zhang, F. Cao, K. Lucas, W. S. Liu, K. Esfarjani, C. Opeil, D. Broido, D. Parker, D. J. Singh, G. Chen and Z. F. Ren, *J. Am. Chem. Soc.*, **134**, 17731, (2012).
[38] L. D. Zhao, J. Q. He, C. I. Wu, T. P. Hogan, X. Y. Zhou, C. Uher, V. P. Dravid and M. G. Kanatzidis, *J. Am. Chem. Soc.*, **134**, 7902, (2012).
[39] H. Wang, E. Schechtel, Y. Z. Pei and J. Snyder, *Adv. Energy Mater.*, **3**, 488, (2013).
[40] Y. Lee, S. H. Lo, C. Q. Chen, H. Sun, D. Y. Chung, T. C. Chasapis, C. Uher, V. P. Dravid and M. G. Kanatzidis, *Nat. Commun.*, ***5***, 3640, (2014).

CHAPTER 7: THERMOELECTRIC PROPERTIES OF P-TYPE SnSe

7.1. Introduction

As we addressed in the preceding chapters, various efforts have been implemented to reach a subtle balance of thermal and electronic transport properties to achieve high *ZT* values [1-6]. These include but not limited to, the phonon-glass electron-crystal approach [7,8], nanostructuring techniques [5], solid solution [9,10], and all-scale hierarchical structuring [11] to reduce the thermal conductivity and resonant doping and band convergence approaches [12-20] to enhance the electronic properties. These techniques have proven to be successful in achieving high *ZT* values in different thermoelectric materials. Another good way to achieve high *ZT* value is to find materials with intrinsic low thermal conductivities, such as Zintl phases, Mo-based clusters and sulphur-based compounds [21-24]. SnSe also shown to have intrinsic ultra low thermal conductivity due to the complex structure with strong anharmonic and anisotropic bonding, contributing to a high *ZT* value of ~2.6 at 923 K along b-axis in single crystalline form [25]. SnSe compounds have been studied more in solar cell technology and phase change memory devices [26-27] than thermoelectric applications because of the large band gap ~ 0.9 eV [28]. SnSe consists of earth-abundant and nontoxic elements, hence it would be better than those containing rare elements [29]. At ambient conditions SnSe crystallizes in a layered orthorhombic structure with space group *Pnma* #62, but the structure undergoes phase transition into a higher symmetric orthorhombic phase with space group *Cmcm* #63 at ~800 K. This high-temperature high-symmetric phase has good thermoelectric properties. However, the structure is thermally unstable under these conditions due to

sublimation, which severely restricts the potential applications [29]. The thermal and electronic transport properties of this binary compound have significant differences along the three crystallographic directions unlike other symmetric IV–VI compounds such as SnTe and lead chalcogenides that crystallize in rock salt structure and have isotropic thermoelectric properties [30,31]. Despite the extraordinary *ZT* values in single crystalline SnSe, the practical device application is difficult because of the poor mechanical properties [32].

Therefore, exploring the thermoelectric properties of polycrystalline SnSe is preferred. Up to now, one study has assessed the thermoelectric performance of undoped polycrystalline SnSe and found a *ZT* value of ~ 0.5 at 823 K [32]. Another study showed that Ag doping increased the carrier concentration and a maximum room temperature Hall carrier concentration of ~ 9×10^{18} cm^{-3} was obtained in $Ag_{0.07}Sn_{0.93}Se$ showing a peak *ZT* value of ~0.6 at 750 K in $Ag_{0.01}Sn_{0.99}Se$ [31]. Very recently, Na is investigated as a potential dopant in SnSe-SnTe alloy system [33]. We also successfully prepared and studied the thermoelectric properties of n-type Sn chalcogenide polycrystalline materials and achieved a peak *ZT* value of ~1.0 at 773 K [34] as explained in the preceding chapter in detail.

Since polycrystalline SnSe has very low electrical conductivity (< 10^3 S m^{-1}), we tried different dopants Na and K (IA element), Mg, Ca, and Ba (IIA element), B, Al, Ga, and In (IIIA element), Sb and Bi (VA element), and also Ag to enhance the carrier concentration and improve the *ZT* values. However, none of these dopants significantly increase the electrical conductivity due to probably lower solubility of these dopants in

SnSe lattice except Ag and Na. Very recently, ultrahigh power factor and thermoelectric performance was obtained in single crystalline SnSe by Na doping showing that Na is a more effective dopant of SnSe [35]. In this chapter, we present our studies on the thermoelectric properties of Na-doped polycrystalline p-type SnSe below the phase transition temperature (~800 K). A peak *ZT* of ~0.8 is obtained at 773 K along the hot pressing direction and the average *ZT* of Na-doped SnSe was improved.

7.2. Experimental Methods

Ingots of $Na_xSn_{1-x}Se$ with $x = 0.01$, 0.015, 0.02, and 0.03 were prepared in a double sealed carbon coated quartz tube from high purity elements (Na chunks, 99.99%; Sn shots, 99.99%; Se granules, 99.99%). The tubes were evacuated to ~3×10^{-4} Pa and sealed, then slowly heated to 900-950 ^{o}C at a rate of 100 ^{o}C h^{-1} and then held at that temperature for 6 hours, then slowly cooled at the same rate to 600 ^{o}C and kept there for 50 hours, and finally cooled to room temperature. The ingots obtained from this procedure were cleaned and only ball milled for 1 minute to achieve some anisotropy in the grains. The ball-milled powder was then loaded into the 1/2 inch central cylindrical hole of graphite dies, hot pressed at 600 ^{o}C for 7 minutes by alternating current (ac-HP) under 50 MPa, air cooled, polished, cleaned, and cut from two different directions (parallel and perpendicular to the hot pressing direction) to a desired shape for thermal and electrical transport property measurements. X-ray diffraction spectra analysis was conducted on a PANalytical multipurpose diffractometer with an X'celerator detector (PANalytical X'Pert Pro). The microstructures were investigated by a scanning electron microscope (SEM, JEOL 6340F). Seebeck coefficient (*S*) and electrical conductivity (*s*) were

measured using a static direct current method and a four-point direct current switching method, respectively, on a commercial (ZEM-3, ULVAC) system. The room temperature Hall carrier concentration (n_H) was measured using a Quantum Design Physical Properties Measurement System. The thermal diffusivity (α) was measured by a laser flash system (LFA 457, Netzsch), the specific heat (C_p) was measured on a differential scanning calorimetry thermal analyzer (DSC 404 C, Netzsch), and the volumetric density (D) was measured by the Archimedes method. The thermal conductivity was calculated by $\kappa = D\alpha C_p$. Our measurements are accurate within 12 % for ZT and 10 % for power factor, due to a 3 % error in electrical conductivity, a 5 % error in Seebeck coefficient, and a 7 % error in thermal conductivity. Error bars are not used in the Figures to increase the readability of the curves.

7.3. Thermoelectric Properties of Na-doped SnSe

Considering the anisotropy of SnSe, we conducted room temperature XRD measurements from two different directions for samples $Na_xSn_{1-x}Se$ with x = 0, 0.01, 0.015, 0.02, and 0.03, as shown in Figure 7.3.1. Analysis of the XRD results indicated Na-doped SnSe crystallizes in pure orthorhombic low symmetric phase with space group *Pnma* #62 similar to undoped SnSe [25]. There are obvious differences in the patterns collected from the two different planes, especially in the intensity of the (400) and (111) reflection peaks, suggesting that grains have preferentially grown along these planes, which agrees with the previous reports for both single crystalline and polycrystalline SnSe [25,32]. The peak positions for Na-doping level of 1 atm. % and 1.5 atm. % shift a little bit to higher angles relative to the undoped sample due to the substitution of a larger atom Sn (0.112

nm) by a smaller atom Na (0.102 nm), for Na-doping levels of 2 atm. % and 3 atm. % the peak positions did not change anymore because they have surpassed the doping limit. The variation of lattice parameters with Na concentration for the two different directions is plotted in Figure 7.3.1 (c) and (d). The SEM images from the freshly fractured surface of undoped and 1.5 atm. % Na-doped samples are shown in (Figure 7.3.2 (a) and (b)) and (Figure 7.3.2 (c) and (d)) respectively. The obvious layered structure leads to the difference in the electrical and thermal transport properties along the two different directions. To further increase the anisotropy, we forged the samples by repressing them. However, thermoelectric properties are not enhanced (not shown here). Since the best thermoelectric property is in one of the in-plane directions according to the single crystal result [25], by hot pressing, we can only get the mixture properties of the two in-plane directions. The grain sizes of undoped SnSe samples are smaller than the 1.5 atm. % Na-doped samples showing an increase in grain size with Na doping. The addition of any additional element in an existing compound could change the chemistry of that compound, which may lead to grain size difference. In Na-doped SnSe, Na has a different atomic radius from Sn to cause a change of stress/strain field in the material. This would affect the grain growth by affecting the surface/grain boundary energy and might produce bigger grains in Na-doped SnSe.

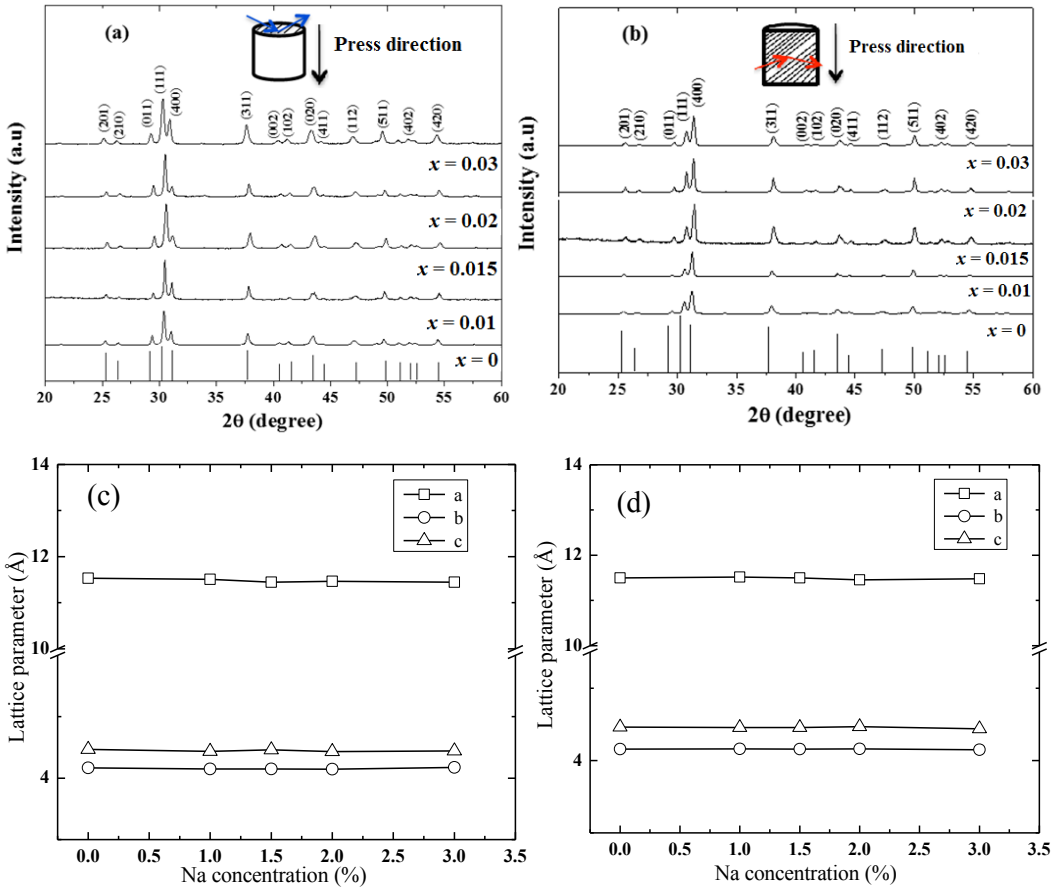

Figure 7.3.1 XRD patterns of the as-pressed bulk samples $Na_xSn_{1-x}Se$ (x = 0, 0.01, 0.015, 0.02, 0.03) for (a) perpendicular (blue arrow) to the hot pressing direction (b) parallel (red arrow) to the hot pressing direction, calculated lattice parameters from the XRD patterns for (c) perpendicular and (d) parallel to the hot pressing direction. The vertical lines at the bottom of (a) and (b) are from the standard card.

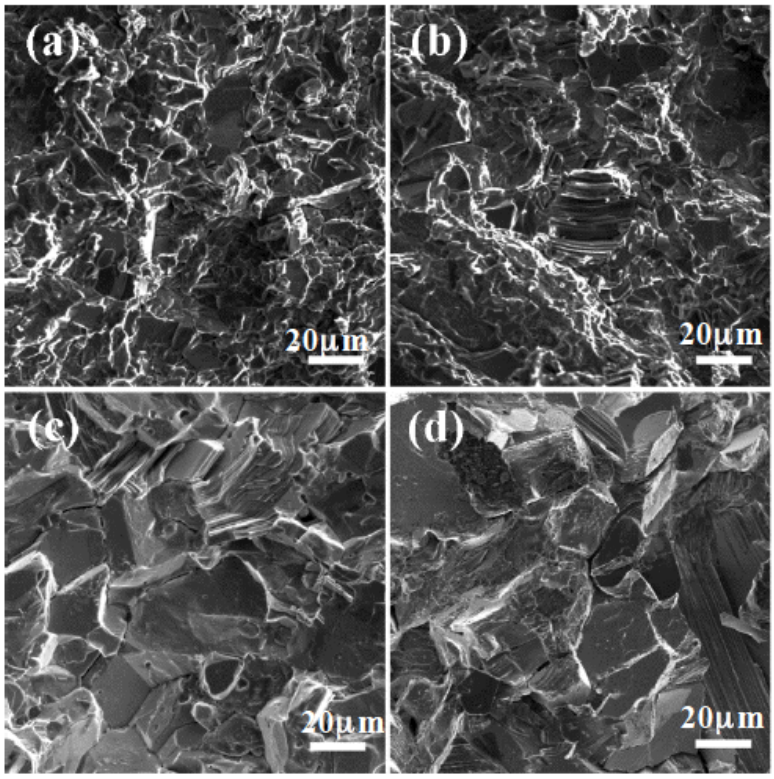

Figure 7.3.2 SEM images of the freshly fractured surface of undoped SnSe (a) bulk samples perpendicular to the hot pressing direction, (b) parallel to the hot pressing direction, and Na-doped $Na_{0.015}Sn_{0.985}Se$ (c) perpendicular to the hot pressing direction, (d) parallel to the hot pressing direction.

Undoped polycrystalline SnSe has a phase transition at about ~800 K [31-33]. For any possible applications, we should avoid using these materials above this phase transition temperature. Hence, all the thermoelectric properties in this study are only measured up to 773 K. Figure 7.3.3 presents the temperature dependence of the specific heat of undoped and 3 atm. % Na-doped SnSe samples. The specific heat of the doped sample is relatively higher than the undoped sample, which is attributed to the substitution of Sn by a lighter atomic mass element Na. We noticed that the Cp had an abnormal increase at 773 K, which is very likely related to the phase transition at ~780 K.

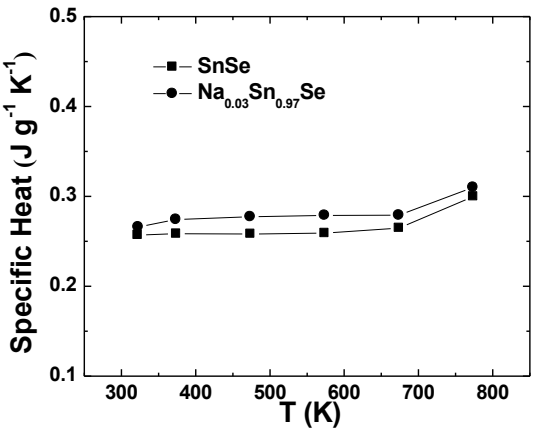

Figure 7.3.3 Temperature dependence of specific heat for undoped SnSe and Na-doped $Na_{0.03}Sn_{0.97}Se$.

Figure 7.3.4 shows the thermoelectric properties ((a) Seebeck coefficient, (b) electrical conductivity, (c) power factor, (d) thermal diffusivity, (e) thermal conductivity and (f) the *ZT*) of Na-doped SnSe (x = 0.01, 0. 015, 0.02, and 0.03) measured along the hot pressing direction compared with the reported data of single crystal SnSe along the b axis (filled star) [25], together with the undoped (dotted line) and the optimized Ag-doped polycrystalline SnSe (solid line) [31]. The Seebeck coefficient of all the samples is positive, indicating that the samples are p-type, consistent with the Hall measurements. The Seebeck coefficient increased from less than 200 $\mu V\ K^{-1}$ to a maximum ~350 $\mu V\ K^{-1}$ at about ~673 K and then decreased due to the bipolar effect of minority carriers activation at elevated temperature. The Seebeck coefficient values of all Na-doped samples shown in Figure 7.3.4 (a) are lower than that of single crystal SnSe [25], undoped, and Ag-doped polycrystalline SnSe [31]. However, the bipolar temperature is higher than that of the single crystal SnSe [25], undoped, and Ag-doped [31] polycrystalline SnSe because of the increase of the carrier concentration by Na doping.

The electrical conductivity of all Na-doped samples is higher than that of the undoped SnSe as shown in Figure 7.3.4 (b). The electrical conductivity first increased with increasing temperature, then decreased from 400 K to 673 K and increased again from 673 K to 773 K, showing typical semiconductor characteristic.

A similar property was also previously reported in undoped polycrystalline SnSe [32]. The increase of electrical conductivity from 673 K to 773 K could be attributed to the thermal activation of minority carriers (electrons) due to the temperature dependent reduction of the band gap. At all temperature ranges the electrical conductivity first increased with Na doping level from 1 atm. % to 1.5 atm. % and then decreased for 2 atm. % and 3 atm. %, yielding the maximum electrical conductivity at 1.5 atm. % Na doping level. This electrical conductivity is higher than the electrical conductivity of polycrystalline Ag-doped SnSe, but still much lower than that of other typical thermoelectric materials with equivalent carrier concentration because of the very low Hall mobility in this material. The decrease in the electrical conductivity at higher doping levels is attributed to the decrease in Hall mobility due to ionized impurity scattering and increased carrier-carrier scattering. Below ~673 K, even though the electrical conductivity decreased at higher doping levels it is still much higher than the electrical conductivity of undoped SnSe and the electrical conductivity of single crystalline SnSe. The maximum power factor is only ~ 4.5 μW cm^{-1} K^{-2} at 773 K for 1.5 atm. % Na doping (see Figure 7.3.4 (c)), and this power factor is less than that of the optimized Ag-doped SnSe due to the lower Seebeck coefficient. However, the thermal conductivity of Na-doped SnSe is lower than that of Ag-doped SnSe and undoped SnSe in the whole

temperature range as shown in Figure 7.3.4 (e) (Figure 7.3.4 (d) shows the corresponding thermal diffusivities). It also showed that the total thermal conductivity is almost independent of Na doping, showing that the lattice part of thermal conductivity is significantly dominant and the electronic part is negligible. This is understandable, since the electrical conductivity is too low. A maximum *ZT* of ~0.8 is obtained at about 773 K in 1.5 atm. % Na-doped SnSe samples. Moreover, the calculated average *ZT* (~0.32) of Na-doped SnSe is relatively higher than the average *ZT*s of undoped SnSe (~0.11), Ag-doped SnSe (~0.27) and a little bit lower than single crystalline SnSe (~0.43) (The highest *ZT* of the single crystalline SnSe is ~1.6 at 773 K) in the temperature range of 300 K to 773 K. Since average *ZT* is very important for real device application [36,37], polycrystalline $Na_{0.015}Sn_{0.985}Se$ seems to be a better candidate compared to the previously studied p-type undoped [31,32], Ag-doped polycrystalline SnSe [31] and single crystalline SnSe that has also poorer mechanical properties.

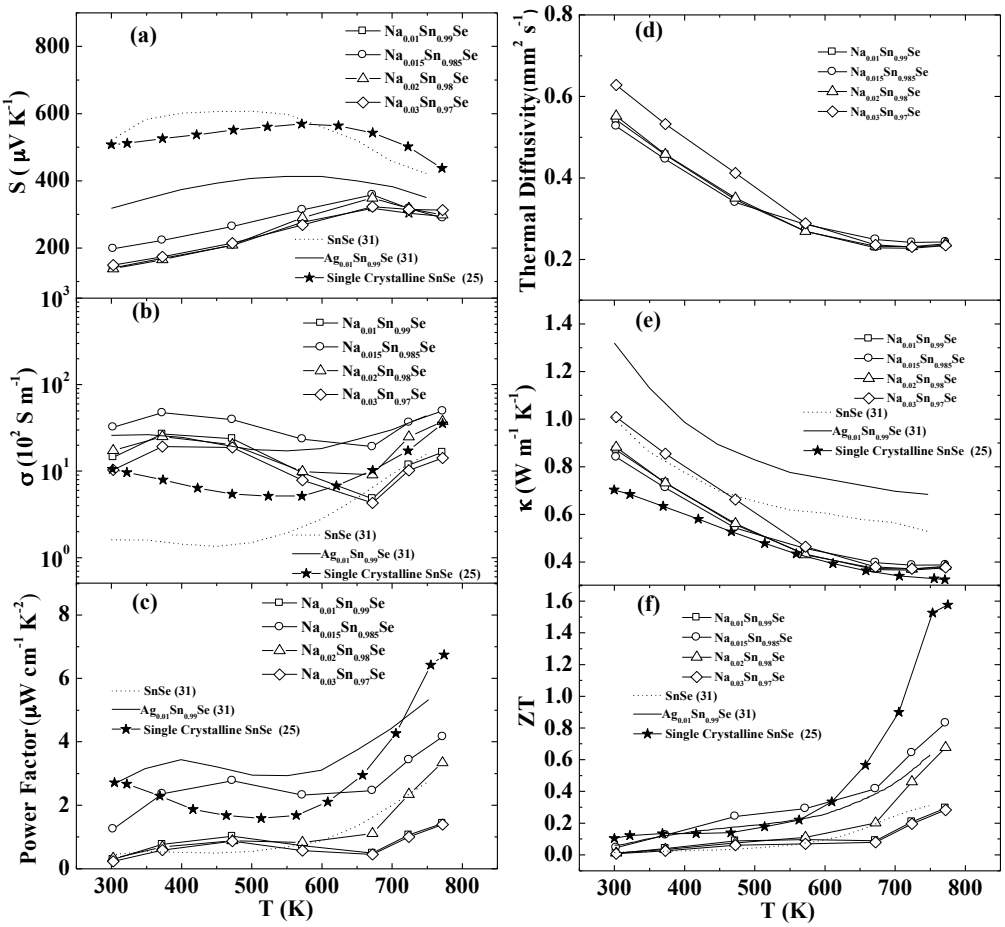

Figure 7.3.4 Temperature dependence of (a) Seebeck coefficient, (b) electrical conductivity, (c) power factor, (d) thermal diffusivity, (e) thermal conductivity, and (f) *ZT* for $Na_xSn_{1-x}Se$ (x = 0, 0.01, 0.015, 0.02, and 0.03) measured along the hot pressing direction compared with that of the reported single crystal SnSe along b axis (filled star) [25], together with the undoped (dotted line) and the optimized Ag-doped polycrystalline SnSe (solid line) [31].

In order to understand the change of transport properties with doping, we fitted our experimental Seebeck coefficient data at 300 K with a single parabolic band model calculation results as shown in Figure 7.3.5(a).

The fitting shows the transport properties of Na-doped SnSe are explained by single parabolic band model with acoustic phonon scattering approximation and density of states effective mass of $m^* = 0.75m_e$, similar to Ag-doped SnSe. The lower Seebeck

coefficient values of Na-doped samples compared to Ag-doped samples are attributed to the higher Hall concentration by Na-doping. The relationship between the Hall carrier concentration and the doping concentration of Na (our work, filled circles) and Ag [31] (open circles) is shown in Figure 7.3.5 (b). The Hall carrier concentration of undoped SnSe is ~2.3×10^{17} cm^{-3}, consistent with the reported data. The carrier concentrations of all Na-doped samples, even the one with the lowest doping concentration (x = 0.01) is higher than the highest carrier concentration obtained by Ag doping (x = 0.07) (9×10^{18} cm^{-3}) [31]. Na has been generally demonstrated as efficient dopant in p-type lead-based chalcogenides and it also effectively increased the Hall concentration of SnSe even at low doping levels. It is found that, the carrier concentration increased with increasing Na doping concentration. However, the electrical conductivity is maximized at a carrier concentration of ~ 2.1×10^{19} cm^{-3} for 1.5 atm. % Na doping. We also summarized the room temperature Hall carrier concentrations and density of selected $Na_xSn_{1-x}Se$ samples in Table 7.3.1. The relative density of all samples is higher than 94 %. There is always Se deficiency due to the evaporation of Se during the preparation; however, it is stable after annealing for 50 hours. When we prepared samples with the nominal composition SnSe, we detected the small vacancy of the Se. Se vacancy can lead to n-type behavior, that's why the undoped SnSe in this study has a lower Hall carrier concentration than that of the single crystal SnSe [25]. However, it is still p-type [34]. When Na is effectively doped into SnSe, more holes contributed, which insured higher p-type conductivity in Na-doped SnSe.

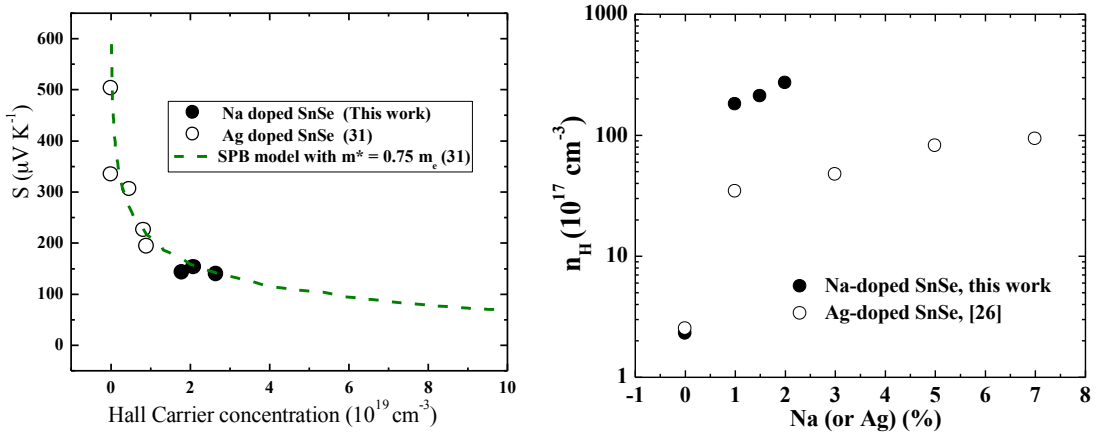

(a) (b)

Figure 7.3.5 Relationship between (a) Seebeck coefficient and Hall carrier concentration for Na-doped (this work filled circles) and Ag-doped [31] (open circles) (b) Hall carrier concentration and Na concentration (this work, filled circles) and Ag concentration [31] (open circle).

Table 7.3.1 Room temperature Hall carrier concentrations, and density of selected $Na_xSn_{1-x}Se$ samples

Nominal Composition	Density (g cm^{-3})	n_H (10^{19} cm^{-3})
SnSe	6.05	0.023
$Na_{0.01}Sn_{0.99}Se$	5.83	1.81
$Na_{0.015}Sn_{0.985}Se$	5.81	2.10
$Na_{0.02}Sn_{0.98}Se$	5.84	2.67

Anisotropic transport properties have been observed in all previous studies of both single crystalline and polycrystalline SnSe [25,31,32]. Na-doped SnSe samples show similar anisotropic structure and transport properties. Figure 7.3.6 shows the thermoelectric properties of $Na_{0.015}Sn_{0.985}Se$ measured in two different directions: parallel (open circles) and perpendicular (filled circles) to the hot pressing direction. There is not much difference between the Seebeck coefficients measured from the two directions.

However, both the electrical conductivity and the thermal conductivity show obvious anisotropy. Because of the higher electrical conductivity when measured perpendicular to the hot pressing direction, the power factor is also higher. However, due to the much lower thermal conductivity along the hot pressing direction, the *ZT* value is a little bit higher along the hot pressing direction. This is consistent with the reported undoped, Ag-doped and I-doped SnSe [31,32,34].

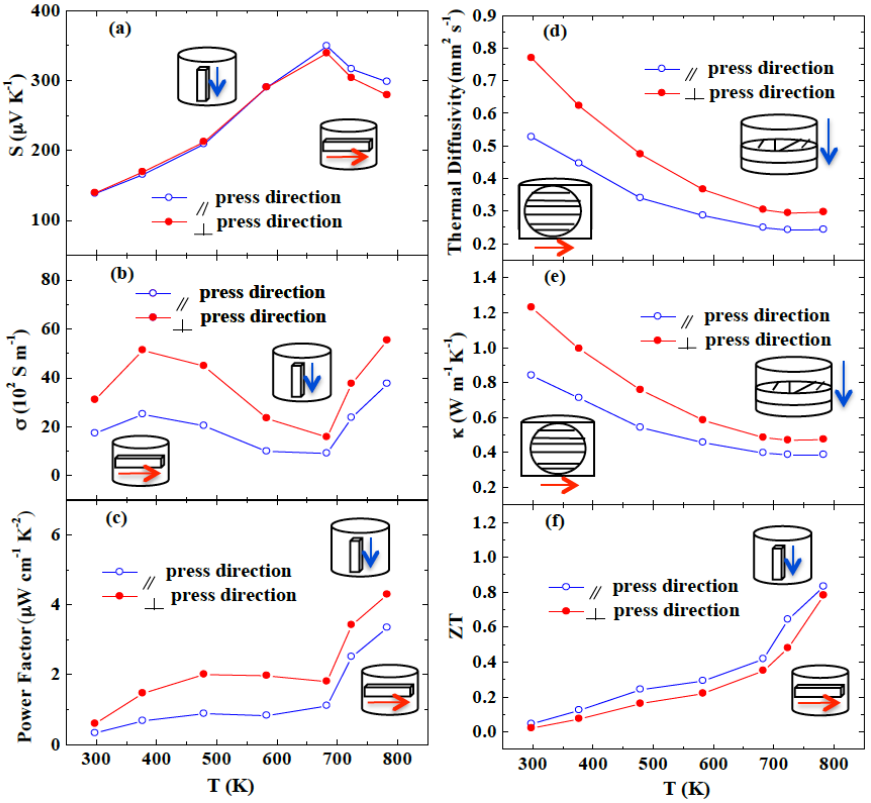

Figure 7.3.6 Temperature dependence of (a) Seebeck coefficient, (b) electrical conductivity, (c) power factor, (d) thermal diffusivity, (e) thermal conductivity, and (f) *ZT* for $Na_{0.015}Sn_{0.985}Se$ measured along the hot pressing direction (blue arrow) and perpendicular to the hot pressing direction (red arrow).

7.4. Conclusion

In this study we showed Na doping could effectively increase the carrier concentration to ~2.7×10^{19} cm^{-3} in polycrystalline SnSe, which results in increased electrical conductivity and power factor. A peak *ZT* of ~0.8 is obtained at 773 K along the hot pressing direction due to the low intrinsic thermal conductivity and enhanced power factor at an optimum Na doping level of 1.5 atm. %.

References

[1] Z. G. Chen, G. Han, L. Yang, L. Cheng and J. Zou, *Progress in Natural Science: Materials International,* **22**, 535-549, (2120).

[2] H. J. Goldsmid, Thermoelectric Refrigeration, *Temple Press Books, Ltd.,* London, (1964).

[3] D. M. Rowe Thermoelectric and Its Energy Harvesting, edited by, *CRC Press*, (2012).

[4] D. M. Rowe Thermoelectric Handbook, Macro to Nano, edited by, *CRC Press, Taylor & Francis Group, Boca Raton FL*, (2006).

[5] J. P. Hermans, M. S. Dreslhaus, L. E. Bell and D. T. Morelli, *Nature Nanotechnol*., **8**, 471-473, (2013).

[6] L. D. Zhao, V. P. Dravid and M. G. Kanatzidis, *Energ Environ. Sci.,* **7**, 251-268, (2014).

[7] B. C. Sales, D. Mandrus and R. K. Williams, *Science,* **272**, 1325-1328, (1996).

[8] H. Kleinke, *Chem. Mater*., **22**, 604-611, (2010).

[9] Q. Zhang, T. Sun, F. Cao, M. Li, M. H. Hong, J. K. Yuan, Q. Y. Yan, H. H. Hng, N. Q. Wu and X. G. Liu, *Nanoscale,* **2**, 1256-1259, (2010).

[10] W. S. Liu, X. Yan, G. Chen and Z. F. Ren, *Nano Energy,* **1**, 42-56, (2012).

[11] K. Biswas, J. Q. He, I. D. Blum, C. I. Wu, T. P. Hogan, D. N. Seldman, V. P. Dravid and M. G. Kanatzidis, *Nature*, **489**, 414-418, (2012).

[12] M. S. Dresselhaus, G. Chen, M. Y. Tang, R. G. Yang, H. Lee, D. Z. Wang, Z. F. Ren, J. P. Fleurial and P. Gogna, *in Materials and Technologies for Direct Thermal-to-Electric Energy Conversion, MRS Symp. Proc. (Eds: J. Yang, T. P. Hogan, R. Funahashi, G. S. Nolas)*, *Materials Research Society Press, Pittsburgh, PA*, pp. 3-12, (2005).

[13] M. S. Dresselhaus and J. P. Heremans, *in Thermoelectrics Handbook: Macro to Nano (Ed: D. M. Rowe), Taylor and Francis, CRC, Boca Raton,* FL, Ch. 39, pp. 1-24, (2006).

[14] Y. Pei, X. Shi, A. LaLonde, H. Wang, L. Chen and G. J. Snyder, *Nature,* **473**, 66-69, (2011).

[15] S. N. Girard, J. He, X. Zhou, D. Shoemaker, C. M. Jaworski, C. Uher, V. P. Dravid, J. P. Heremans and M. G. Kanatzidis, *J. Am. Chem. Soc.,* **133**, 16588-16597, (2011).

[16] Y. Pei, A. D. LaLonde, N. A. Heinz, X. Shi, S. Iwanaga, H. Wang, and L. Chen and G. J. Snyder, *Adv. Mater.,* **23**, 5674-5678, (2011).

[17] J. P. Heremans, V. Jovovic, E. S. Toberer, A. Saramat, K. Kurosaki, A. Charoenphakdee, S. Yamanaka and G. J. Snyder, *Science,* **321**, 554-557, (2008).

[18] Q. Zhang, H. Wang, W. Liu, H. Wang, B. Yu, Q. Zhang, Z. Tian, G. Ni, S. Lee, K. Esfarjani, G. Chen and Z. Ren, *Energy Environ. Sci*., **5**, 5246-5251, (2012).

[19] J. P. Heremans, B. Wiendlocha and A. M. Chamoire, *Energy Environ. Sci.,* **5**, 5510-5530, (2012).
[20] C. M. Jaworski, B. Wiendlocha, V. Jovovic and J. P. Heremans, *Energy Environ. Sci.,* **4**, 4155-4162, (2011).
[21] S. K. Bux, A. Zevalkink, O. Janka, D. Uhl, S. Kauzlarich, G. J. Snyder and J. P. Fleurial, *J. Mater. Chem.* A, **2**, 215-220, (2014).
[22] P. Gougeon, P. Gall, R. Al Rahal Al Orabi, B. Fontaine, R. Gautier, M. Potel, T. Zhou, B. Lenoir, M. Colin, C. Candolfi and A. Dauscher, *Chem. Mater.,* **24**, 2899-2908, (2012).
[23] A. Zevalkink, Y. Takagiwa, K. Kitahara, K. Kimura and G. J. Snyder, *Dalton Trans.,* **43**, 4720-4725, (2014).
[24] X. Lu, D. T. Morelli, Y. Xia, F. Zhou, V. Ozolins, H. Chi, X. Zhou and C. Uher, *Adv. Energy Mater.,* **3**, 342-348, (2013).
[25] L. D. Zhao, S. H. Lo, Y. Zhang, H. Sun, G. Tan, C. Uher, C. Wolverton, V. P. Dravid and M. G. Kanatzidis, *Nature*, **508**, 373–377, (2014).
[26] C. Guillen, J. Montero and J. Herrero, *Phys. Status Solidi A*, **208**, 679-683, (2011).
[27] K. M. Chung, D. Wamwangi, M. Woda, M. Wuttig, and W. Bensch, *J. Appl. Phys*., **103**, 083523-083523-7, (2008).
[28] S. Chen, K. Cai and W. Zhao, *Physica B*, **407**, 4154-4159, (2012).
[29] I. Loa, R. J. Husband, R.A. Downie, S. R. Popuri and J-W. G. Bos, *J. Phys.: Condens. Matter,* **27**, 072202, (2015).
[30] Q. Zhang, B. Liao, Y. Lan, K. Lukas, W. Liu, K. Esfarjani, C. Opeil, D. Broido, G. Chen and Z. Ren,. *Proc. Natl. Acad. Sci., USA,* August 13, *vol.* **110** *no.* 33,13263-13266, (2013).
[31] C. L. Chen, H. Wang, Y. Y. Chen T. Daya and G. J. Snyder, *J. Mater. Chem.* A, **2**, 11171-11176, (2014).
[32] S. Sassi, C. Candolfi, J. B. Vaney, V. Ohorodniichuk, P. Masschelein, A. Dauscher and B. Lenoir, *Appl. Phys. Lett.,* **104**, 212105, (2014).
[33] W. R. Tian, W. F. Chao, Z. Xiaozhi, T. Qing, S. Li, P. Yu and L. F. Jing *Phys. Chem. Chem. Phys.*, **17**, 30102-30109, (2015).
[34] Q. Zhang, E. K. Chere, J. Sun, F. Cao, K. Dahal, S. Chen, G. Chen and Z. Ren, *Adv. Energy Mater.,*1500360, (*2015*).
[35] L. D. Zhao, G. Tan, S. Hao, J. He, Y. Pei, H. Chi, H. Wang, S. Gong, H. Xu, V. P. Dravid, U. Ctirad, G. J. Snyder, C. Wolverton and M. G. Kanatzidis, *Science* DOI: 10.1126/science.aad3749.
[36] E. K. Chere, Q. Zhang, K. McEnaney, M. L. Yao, F. Cao, J. Y. Sun, S. Chen, C. Opeil, G. Chen and Z. Ren, *Nano Energy*, **13**, 355-367, (2015).
[37] Q. Zhang, E. K. Chere, K. McEnaney, M. L. Yao, F. Cao, Y. Ni, S. Chen, C. Opeil, G. Chen and Z. Ren, *Adv. Energy Mater*., 1401977, (2015).

CHAPTER 8: SUMMARY

In conclusion, we have successfully prepared and studied the thermoelectric performance of lead and tin chalcogenides. In our study of lead chalcogenides we came up with a different approach of improving the performance of these materials by systematically improving their thermoelectric performance near room temperature.

In our investigation of the thermoelectric properties of n-type PbSe, we discovered transition metals (Ti, V, Cr, Nb, and Mo) as effective dopants to enhance the lower temperature (below 600 K) thermoelectric properties. Specifically, Cr doping in PbSe enhanced the room temperature *ZT* to ~0.4 and the peak *ZT* to ~1.0 between 573 K and 673 K. Hence, the average *ZT* of n-type PbSe is increased over a wide temperature range (300 K to 873 K). A thermal to electrical conversion efficiency of up to ~12 % is achieved in 0.5 atm. % Cr doped PbSe atcold-side temperature of 300 K and hot-side temperature of 773 K. At the lower temperature range, when the hot-side temperature is between 350 K and 523 K, the device efficiency of Cr-doped PbSe is still pretty high and only slightly lower than that of the state-of-the-art n-type $Bi_2Te_{2.7}Se_{0.3}$ system. This makes Cr-doped PbSe a promising thermoelectric material for cooling and power generation applications.

In a similar investigation of the thermoelectric performance of PbTe-PbSe quaternary alloy, we found Cr is still the most effective dopant to tailor the thermoelectric properties near room temperature. In this systematic study of Cr doping in $PbTe_{1-y}Se_y$, a *ZT* of ~0.6 at room temperature was achieved in Te-rich $Cr_{0.015}Pb_{0.985}Te_{0.75}Se_{0.25}$ resulting from combination of a higher power factor and a lower thermal conductivity. This *ZT* value is

a record value achieved so far in the family of lead-chalcogenide systems at room-temperature. A peak *ZT* of ~1 was also obtained in Se-rich $Cr_{0.01}Pb_{0.99}Te_{0.25}Se_{0.75}$ at about 573 to 673 K, with a room-temperature *ZT* of ~0.5. The thermal to electrical conversion efficiencies of Te-rich $Cr_{0.015}Pb_{0.985}Te_{0.75}Se_{0.25}$ and Se-rich $Cr_{0.01}Pb_{0.99}Te_{0.25}Se_{0.75}$ are ~10 % and ~12 %, respectively, with hot-side temperature of 773 K andcold-side temperature of 300 K. This result shows both Te-rich $Cr_{0.015}Pb_{0.985}Te_{0.75}Se_{0.25}$ and Se-rich $Cr_{0.01}Pb_{0.99}Te_{0.25}Se_{0.75}$ alloys could potentially be used for cooling and medium temperature power generation applications.

Interestingly, in both PbSe and PbTe-PbSe alloys, Cr doping tunes the carrier concentration to an optimum value from 10^{18} cm^{-3} to 10^{19} cm^{-3} and we found the room temperature performance of lead chalcogenides got boosted under this range of carrier concentration. Even though, Cr is speculated as a resonant dopant in lead chalcogenides, our results showed no resonant effect in both PbSe and PbTe-PbSe alloys and further investigation is needed to explain what modifications happened in the band structure to yield these interesting thermoelectric properties at room temperature.

On another study of the thermoelectric performance of PbTe-PbS quaternary alloy, we found Indium (In) as effective dopant to tune the carrier concentration by forming deep lying defect states. PbS was incorporated into In-doped PbTe to increase the electrical conductivity by band structure modification and to decrease the thermal conductivity by alloy scattering and spinodal decomposition. We achieved a room-temperature *ZT* as high as ~0.5 in $In_{0.02}Pb_{0.98}Te_{0.8}S_{0.2}$. With high-room temperature *ZT* optimized by deep lying doping, desirable average *ZT* and engineering figure of merit, $(ZT)_{eng}$, are obtained in

$In_{0.02}Pb_{0.98}Te_{0.8}S_{0.2}$, leading to an efficiency of ~12% withcold-side temperature of 323 K and hot-side temperature of 773 K. In-doped $PbTe_{1-y}S_y$ has high $(ZT)_{eng}$ due to the deep lying doping that lead to optimal carrier concentration for good room-temperature *ZT* and high-temperature *ZT*. This method could be applied to other material systems for higher thermoelectric efficiencies.

In our study of anisotropic polycrystalline SnSe materials, we synthesized I-doped n-type SnSe by melting and hot pressing for the first time. Iodine doping changed the conductivity type and increased the electron carrier concentration to ~ $2x10^{17}$ cm^{-3} in $SnSe_{0.96}I_{0.04}$. A *ZT* value of ~ 0.8 was obtained along the hot pressing direction at about 773 K due to the intrinsic ultralow thermal conductivity in $SnSe_{0.97}I_{0.03}$. A highest *ZT* of ~ 1.0 was achieved by alloying 10 atm. % SnS with 3 atm. % I-doping along the hot pressing direction at about 773 K.

In our study of p-type polycrystalline SnSe, we found Na doping could effectively increase the carrier concentration to ~2.7×10^{19} cm^{-3}, which results in a relatively higher electrical conductivity and power factor. A peak *ZT* of ~0.8 is obtained at 773 K along the hot pressing direction due to the low intrinsic thermal conductivity and enhanced power factor at an optimum Na doping level of 1.5 atm. %.

Even though, high peak *ZT* value is obtained in p-type single crystalline SnSe, the *ZT* of its polycrystalline form is not quite promising. In order to use this environmentally friendly and economic material, the average *ZT* needs to be improved.